Investigation of Anisotropic Rotor with Different Shaft Orientation

Vom Fachbereich Maschinenbau
der Technischen Universität Darmstadt
zur Erlangung des Grades eines
Doktor-Ingenieurs (Dr.-Ing.)
genehmigte

Dissertation

von

Jhon Malta, M.T.

aus Bukittinggi, Indonesien

Referent:	Prof. Dr.-Ing. Richard Markert
Koreferent:	Prof. Dr. Peter Hagedorn
Tag der Einreichung:	26.02.2009
Tag der mündlichen Prüfung:	13.05.2009

Darmstadt 2009
D 17

Declaration

Herewith, I certify that I have written the present work independently apart of the therein explicitly cited sources.

Erklärung

Hiermit erkläre ich, dass ich die vorliegende Arbeit, abgesehen von den in ihr ausdrücklich genannten Hilfen, selbständig verfasst habe.

Darmstadt, May 2009 Jhon Malta

Abstract

The present work deals with a new discrete model of an anisotropic rotor. The rotor is supported by rigid or anisotropic flexible bearings. Because of different orientations of the cross-section along the shaft, the rotor is modelled by discrete elements. An anisotropic rotor system can be analyzed both in a fixed and in a rotating reference frames. In fixed reference frame, the shaft stiffness varies with time. In rotating reference frame, the differential equations of the system become speed-dependent. If an anisotropic rotor is supported by anisotropic flexible bearings, the system stiffness is always a time-variant parameter whether the rotor is modelled in a fixed or in a rotating reference frame. In the developed model, the shaft stiffness matrix is assembled in the rotating reference frame by considering asymmetric bending by means of the strain energy method. The gyroscopic moments and the internal and external damping are taken into account. The differential equations of motion of the rotor are developed for a rotor at constant angular speed, at constant angular acceleration and accelerated by a constant driving torque.

A stability investigation is conducted of an anisotropic rotor through analysis of eigenvalues for a speed-dependent rotor system and by using FLOQUET theory for a time-variant rotor system. The dynamic responses of the rotor are solved by using the RUNGE-KUTTA method of fourth order. Several anisotropic rotors with single or two disks with different shaft orientations are presented. Additionally, an approach of a twisted anisotropic rotor is developed and analyzed with the minimum and a high number of discrete shaft elements. The eigenvalue analyses and stability charts of these models are presented. The influences of the shaft element anisotropy and the difference in the shaft orientation are analyzed. The difference in the shaft orientation affects the occurrence of the second region of instability and the width of instability. The occurrence of gyroscopic moments in the rotor system is influenced not only by the asymmetry of the rotor but also by the difference in the shaft orientation.

Experimental investigation of an anisotropic rotor with two disks and different shaft orientations is conducted at constant angular speed and constant angular acceleration. These experimental results are benchmarked with the numerical simulations of the developed discretized model.

Kurzfassung

Die vorliegende Arbeit behandelt ein neues diskretes Modell eines anisotropen Rotors. Der Rotor ist starr- oder anisotrop-elastisch gelagert. Aufgrund verschiedener Orientierungen der Wellenquerschnitte wird der Rotor mit Hilfe von diskreten Elementen modelliert. Ein Rotorsystem kann im festen oder im mitrotierenden Koordinatensystem beschrieben werden. Im festen Koordinatensystem ist die resultierende Steifigkeitsmatrix der Welle zeitlich periodisch. Im mitrotierenden Koordinatensystem ist sie von der Drehzahl abhängig. Wenn ein anisotroper Rotor in anisotrop-elastischen Lagern gelagert wird, ist die Systemsteifigkeitmatrix periodisch zeitvariant, unabhängig davon ob der Rotor im festen- oder im mitrotierenden Koordinatensystem betrachtet wird. Im hier entwickelten Modell wird die Steifigkeitsmatrix der Rotorwelle mit Hilfe des Ansatzes der schiefen Biegung durch die Formänderungsenergiemethode aufgestellt. Die gyroscopischen Momente und die innere- und außere Dämpfung werden ebenfalls berücksichtigt. Die Bewegungsgleichungen des Rotors werden für den Betrieb bei konstanter Drehzahl, bei konstanter Drehbeschleunigung und bei konstantem Antriebmoment entwickelt.

Stabilitätsuntersuchungen werden für ein drehzahlabhängiges Rotorsystem mit Hilfe der Eigenwertanalyse und für ein zeitvariantes Rotorsystem mit Hilfe der FLOQUET-Theorie durchgeführt. Die Differentialsgleichungen des Rotors werden numerisch mit Hilfe der RUNGE-KUTTA Methode vierter Ordnung gelöst. Rotorbeispiele mit einer oder zwei Scheiben und verschiedene Wellenorientierungen werden vorgestellt. Zusätzlich wird ein Ansatz eines verdrehten anisotropen Rotors entwickelt und mit der minimalen als auch einer hohen Anzahl an Wellenelementen diskretisiert. Die Eigenwertanalyse und die Stabilitätskarte der Modelle werden präsentiert. Die Einflüsse der Wellenanisotropie und verschiedener Wellenorientierungen werden aufgezeigt. Unterschiede in der Wellenorientierung beeinflussen das Auftreten eines zusätzlichen Instabilitätsgebietes und die Größe des Instabilitätsgebietes. Das Auftreten von gyroscopischen Momente wird nicht nur durch den asymmetrischen Rotor beeinflußt sondern auch durch die Unterschiede in der Wellenorientierung.

Experimentelle Untersuchungen eines anisotropen Rotors mit zwei Scheiben und verschiedener Wellenorientierungen werden bei konstanter Drehzahl als auch bei konstanter Drehbeschleunigung durchgeführt. Um die entwickelten Diskritsmodelle zu überprüfen, werden diese experimentellen Untersuchungen mit direkter numerischer Simulation verglichen.

Acknowledgements

This dissertation is my work of more than three years in the department of structural dynamics, faculty of mechanical engineering, Technische Universität Darmstadt in the field of rotor dynamics.

I gratefully thank to Prof. Dr.-Ing. Richard Markert as my supervisor for his encouragement, useful suggestion and valuable disscusions. I would especially like to thank Prof. Dr. Peter Hagedorn for his willingness to co-supervise my dissertation. I would like to express my deep appreciation for both promoters for supporting and enabling my research financed by the DAAD (Deutscher Akademischer Austausch Dient) scholarship without which this work would not have been possible.

I am sincerely thankful to my colleague Dr.techn. Fadi Dohnal for his efforts in valuable discussions and suggestions. I would also like to thank Frau Maria Rauck and Frau Renate Schreiber for their helpfulness in administration. Meanwhile, I am thankful to all my colleagues: Dipl.-Ing. Martin Kreschel, Dipl.-Ing. Katrin Baumann, Dipl.-Ing. Anke Böttcher, Dipl.-Ing. Gunnar Wieland, Dipl.-Ing. Christoph Mischke, Dipl.-Ing. Steffen Neeb, Dipl.-Ing. Jens Bauer, Dipl.-Ing. Nicklas Norrick and Dipl.-Ing. Felix Dornbusch. Besides that, I deeply gratitude to the DAAD, which has financed me and my family in Germany.

Special thanks are due to my wife Lenggo Geni and my children Khawarizmi Aydin and Khalid Shidqi for their love, appreciation and encouragement in my life.

Darmstadt, May 2009 Jhon Malta

Contents

Nomenclature

Latin

Symbol	Unit	Meaning
A	m^2	cross-section area
$\boldsymbol{A}, \boldsymbol{B}$		state-space matrices
$c_{\square}$	N/m	stiffness coefficient
$\boldsymbol{C}$		general stiffness matrix
$\boldsymbol{C}_{\square}$		proportional matrix due to displacement
$\tilde{\boldsymbol{C}}$		modal stiffness matrix
d_a	Ns/m	external damping coefficient
d_i	Ns/m	internal damping coefficient
D_a		modal external damping coefficient
D_i		modal internal damping coefficient
$\boldsymbol{D}$		general damping matrix
$\boldsymbol{D}_{\square}$		proportional matrix due to velocity
$\tilde{\boldsymbol{D}}$		modal damping matrix
E	N/m^2	Young’s modulus
$\boldsymbol{f}_{\square}$		force vector
$F_{\square}$	N	single force
$\hat{F}_{\square}$		unit force
g	Ns/m	acceleration of gravitation
$h_{\square}$	m/N	flexibility influence coefficient
$\boldsymbol{H}$		flexibility matrix
$I_{\square}$	m^4	moment of inertia of area
$\boldsymbol{I}$		identity matrix
$L_{\square}$		reference point of bearing
$\boldsymbol{L}$		left eigenvectors of a matrix
$m_{\square}$	kg	mass coefficient of disk
$M_{\square}$	Nm	bending moment
$\hat{M}_{\square}$		normalized bending moment

$\boldsymbol{M}$		general mass matrix
$\boldsymbol{M}_{\square}$		inertial mass matrix
$\tilde{\boldsymbol{M}}$		modal mass matrix
$N(x)$	N	normal force as a function of position in x-direction
N		degree of freedom of system
N_d		number of node
N_e		number of element
O		coordinate (0,0,0)
p		investigated point
$\boldsymbol{p}_{\square}$		column matrix of forces
$\boldsymbol{q}$		column matrix of general displacements in rotating reference frame
$\boldsymbol{q}_{\square}$		column matrix of displacements in rotating reference frame
$\boldsymbol{r}$		state-space column matrix
$\tilde{\boldsymbol{r}}$		state-space modal column matrix
$\boldsymbol{R}$		right eigenvectors of a matrix
u	m	deflection in x-direction
v	m	deflection in η-direction
w	m	deflection in ζ-direction
W		centre of shaft
S		centre of disk mass
t	s	time
T	s	period
U	Nm	strain energy
U	Nm	active internal strain energy
$\bar{U}$	Nm	passive internal strain energy
W	Nm	external work
x, y, z		global fixed coordinate system
x', y', z'		local coordinate of disk
$x_{\square}$	m	position of measured point in x-direction
$y_{\square}$	m	position of measured point in y-direction
$z_{\square}$	m	position of measured point in z-direction
$\boldsymbol{0}$		zero matrix

Greek

Symbol	Unit	Meaning
α	rad/s^2	angular acceleration of rotor

$\beta_{\square}$	( )°	angle of principal axis due to rotating reference frame
χ	rad/s	eigenvalue of transpose state-space matrix
δ		specified modal damping ratio
$\epsilon_{\square}$	m	eccentricity
$\phi_{\square}$	( )°	angle of eccentricity
φ	rad	angle (counterclockwise) between rotating and fixed reference frame
φ_y	rad	precession of z-axis
φ_z	rad	precession of y-axis
γ	rad	initial angle of angular position
$\eta_{\square}$	m	position of measured point in η-direction
κ	m	radius of gyration
λ	rad/s	eigenvalue of state-space matrix
Λ		logarithmic decrement
μ_L		anisotropy coefficient of bearing
μ_W		anisotropy coefficient of shaft
$\mathbf{\Phi}$		normalized eigenvector
σ_x	N/m	normal stress in x-axis
Θ_a	kg m^2	axial mass moment of inertia
Θ_p	kg m^2	polar mass moment of inertia
ω	rad/s	natural frequency
ω'	rad/s	normalized forward whirl speed in fixed reference frame
$\bar{\omega}'$	rad/s	normalized backward whirl speed in fixed reference frame
ω^*	rad/s	forward whirl speed in rotating reference frame
$\bar{\omega}^*$	rad/s	backward whirl speed in rotating reference frame
Ω	rad/s	rotational speed of rotor
$\mathbf{\Psi}$		fundamental matrix
x, η, ζ		global rotating coordinate system
x, η^*, ζ^*		coordinate system of principal axis of shaft element
$\zeta_{\square}$	m	position of measured point in ζ-direction

Subscribe Index

Symbol	Meaning
i, j, k, n	integer value of index
k	index number of shaft element
x, y, z	directions in fixed reference frame of system
x', y', z'	directions in fixed reference frame of disk

x, η, ζ	directions in rotating reference frame of system
x, η^*, ζ^*	directions in coordinate system of principal axis

Other Symbols

Symbol	Unit	Meaning
$\ell_{\square}$	m	length of shaft element
$\Im$		imaginary part
$\Re$		real part

Chapter 1

Introduction

1.1 Motivation

An anisotropic rotor can be found in turbogenerators, helicopter rotors, two-bladed propellers and two-pole generators. For such a motor increased vibrations may occur at half of its first bending critical speed. If a rotor has no longer a circular cross-section, its cross-sections are characterized by two different cross-sectional moments of inertia. Therefore, during one revolution of a horizontal rotor shaft the same position of cross-section occurs twice as illustrated in Figure 1.1. This phenomenon is termed the weight critical [11].

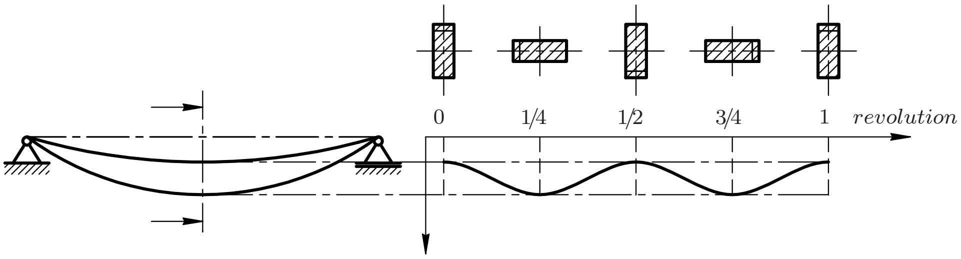

Figure 1.1: Ilustration of rotating anisotropic rotor

For a real rotor system with a constant cross-section along the shaft, the system can be approached by a JEFFCOTT rotor model. For a more complicated rotor system, it can be modelled as a discrete or continuous rotor. For the JEFFCOTT rotor model, the simplest rotor model possessing two degrees of freedom (i.e. in horizontal and vertical axes), a system can be solved straightforwardly both, by analytical analysis and numerical simulation, especially when it is analyzed at constant rotational speed. By a non-stationary case of an anisotropic JEFFCOTT rotor or an anisotropic rotor supported by flexible anisotropic bearings, the differential equations of the system become time-variant, hence the solving is more difficult and can be done numerically only.

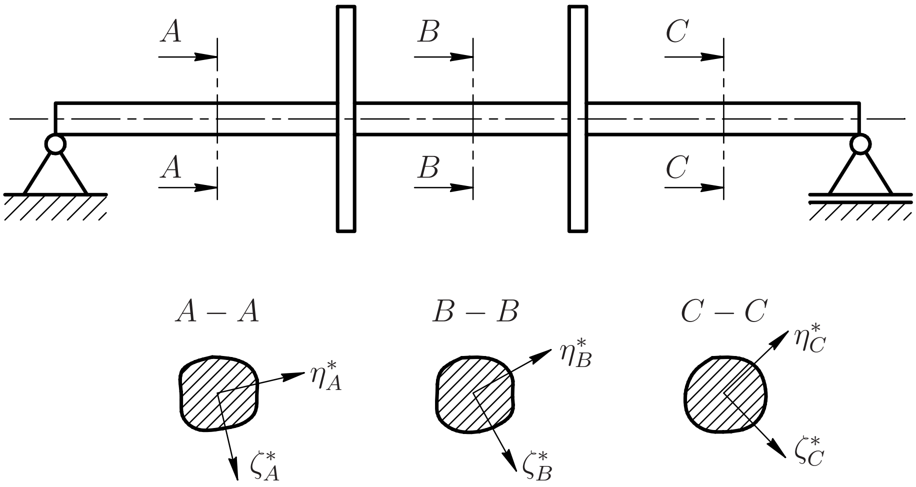

Figure 1.2: Anisotropic rotor with three shaft sections and different shaft orientation in each section

If a real rotor with different cross-sections along the shaft is modelled by discrete elements, it is possible that the elements will have different orientations of principal axes as shown in Figure 1.2. In case of a twisted anisotropic shaft with two disks, the directions of principal axes of cross-sections change along the shaft although the shaft has constant cross-sections. The example rotor in Figure 1.2 is modelled by using the minimal number of three elements i.e. one element for each shaft section. Because of the difference in the orientation in each element, the rotor will have the characterictic of asymmetric bending. Therefore, a JEFFCOTT rotor is no longer a satisfactory model and a new approach of a discrete or continuous rotor should be developed. If the model is discretized by using one-dimensional elements, the approach can be developed by using the finite element or the transfer matrix method. However, the difference in the element orientation must be taken into account. Therefore, a modification in the existing methods is needed. If the model is discretized by using three-dimensional solid elements, the system will have more degrees of freedom compared to the approach with one-dimensional elements. Therefore, the computational cost is very high, because the differential equations of rotor motion are speed or time-dependent depending in the system's frame of reference. In order to obtain a model with the minimal degrees of freedom, an alternative method is developed here by using the strain energy method for asymmetric bending of a beam.

1.2 Related topics

Particularly in the last fifty years, the weight critical of rotors has been widely investigated by many researchers and numerous papers have been published. In general, these investigations can be categoried into two types of rotors. Firstly, the rotor is approached by using the JEFFCOTT rotor model consisting of modal properties or simple physical model of a disk and massless shaft for the analysis. Second, the rotor is approached by using a model of discrete or continuous rotor. Each type can be analyzed based on the assumption that the rotational speed is constant (i.e. stationary operation) or accelerated (i.e. non-stationary operation).

1.2.1 JEFFCOTT rotor and modified JEFFCOTT rotor

The fundamental theoretical investigations of an anisotropic rotor and its corresponding differential equations of motion have been studied by KELLENBERGER [23] and ARIARATNAM [2]. In order to describe its basic characteristic, MICHATZ [38] investigated a simple JEFFCOTT rotor model, in which the effects of external and internal damping on the rotor have been taken into account. In this model, the instability of the rotor can be described accurately. Other studies show that two types of unstable vibrations can occur on anisotropic rotors. They are termed statically and dynamically unstable vibrations, as reported in [42]. YAMAMOTO *et al* [55] investigated an asymmetrical rotor with inequality in stiffness (i.e. different cross-sections along the shaft) including the effects of gyroscopic moments. HULL [15] conducted experiments and showed the forward and backward whirl motion of anisotropic rotors which are supported by flexible anisotropic bearings. A more complicated model with an asymmetric stiffness and an asymmetric disk can be found in [36]. IWATSUBO et al [18] concerned with the vibrations of an asymmetric simple rotor supported by asymmetric bearings. The effects of asymmetry of the rotor and the bearing stiffness have been analyzed. However, some parameters in the model like the eccentricity of the rotor, the acceleration of gravity, the effects of rotary inertia, gyroscopic moments and shear deformation were neglected. The change of angular position of the static and dynamic unbalance influences the increase rate of the total energy and the torque applied to the shaft end. These investigations are reported in [43].

In the design of rotor dynamics, it is essential to investigate the stability of the system. In an investigation, it is important to distinguish the cases whether an anisotropic rotor is supported by rigid or by flexible bearings, because the analyses are different. For the case of an anisotropic rotor in rigid bearings analyzed in a fixed reference frame, the system becomes time-dependent and if analyzed in a rotating reference frame, the system becomes speed-dependent. For the case of an anisotropic rotor in flexible bearings especially in anisotropic flexible bearings, the system becomes time-dependent although they are analyzed either in a fixed or a rotating reference frame (see Table 1.1). In order to investigate the stability of time-variant system, some methods have been developed. Two of these methods are FLOQUET's theory and HILL's method. Both methods have been applied in numerical simulations [3], [47], [48], [52], [54].

In order to minimize the effects of anisotropic stiffness on rotors, several solutions have been published. WETTERGREN and OLSSON [51] dealt with an anisotropic JEFFCOTT rotor supported by anisotropic bearings and supposed that the combination of the damping and asymmetric stiffness of the shaft and the damping and anisotropic stiffness of the bearings can minimize the effect of instability of the rotor. ACKERMAN *et al* [1] proposed a method to identify an anisotropic stiffness of a rotor by investigating the vibrations at twice of the rotational speed of the shaft. For the theoretical and identified models an approach of a non-circular JEFFCOTT rotor was used in order to simplify the differential equations of motion.

Table 1.1: Analysis of anisotropic rotor-bearings system [47]

Type of bearings	Fixed reference frame	Rotating reference frame
rigid	time-dependent	speed-dependent
flexible	time-dependent	time-dependent

Various other studies deal with the change of rotor speed e.g. accelerating the rotor through its bending critical speed. It is well known that the amplitude of the unbalance response of a rotor which runs through a critical speed can be reduced by increasing the value of the acceleration. IWATSUBO *et al* [17] studied the non-stationary vibration of an asymmetric rotor passing through its critical speed. In their models, two approaches have been used. In the first approach the system is driven at constant acceleration, for which an energy source provides an ideal driving force to the vibrating system. The second one is an energy source interacting with the vibrating system, where the system is driven by a non-ideal energy source. MARKERT *et al* [28] investigated a minimal torque that is needed to accelerate an elastic rotor to pass the first bending critical speed. Meanwhile, MARKERT found that as reported in [30] and [31], the maximum rotor deflection is smaller than during stationary resonance speed. The maximum rotor deflection does not appear when the rotor speed corresponds to the critical speed. The peak is shifted to a higher frequency during run-up and shifted to a lower frequency during run-down. After running through resonance the vibrational components at natural frequency dominate but will decay with time. Ganesan [7] analyzed the effect of bearings and shaft asymmetry on the stability of the rotor. Particular attention has been paid to the motion characterictics of the rotor while passing through the primary resonance. The presence of proper combination between bearings and shaft asymmetries on the rotor helps the stability of the unbalance response during start-up or run-down operation.

1.2.2 Discrete or continuous rotor

In order to describe the complete nature of the problem, additional characteristics must be also considered. In this problem, the JEFFCOTT rotor is no longer a satisfactory model. Therefore, several solutions are proposed by using an approach of a discrete or continuous rotor. GASCH *et al* [8] and MARKERT [29] investigated a flexible rotor with a continuous mass distribution passing through its critical speeds under a driving torque. Similar to the authors above, GENTA and DELPRETE [13] approached a rotor system with multiple degrees of freedom by using the finite element method. Other researcher have formulated the differential equations of motion by using EULER's beam theory [27], a modified transfer matrix method [22] or a solid model of finite element method [46]. However, the last three references analyzed the rotor models at constant rotational speed only.

Furthermore, the stability of rotors modelled by discrete elements have been also investigated. ONCESCU *et al* [41] formulated a set of ordinary differential equations with periodic coefficients by using finite element method in conjuction with a time-transfer matrix method based on FLOQUET's theory. In their model, the shaft cross-section is asymmetric, having different principal moments of inertia and varied step-by-step along the longitudinal axis. However, the principal directions of inertia of the cross-section is uniform along the shaft. By taking into account of the shear deformation in the rotor model (i.e. TIMOSHENKO beam), CHEN and PENG [5] have analyzed the stability of the rotor based using the finite element method. The authors [20] and [21] investigated the influences of the damping in the bearings on the instability of a rotating asymmetric shaft supported by isotropic bearings. They used the approach of continuous shaft in their model and solved the problem analytically. In general, the bearing stiffness cannot eliminate an unstable region, but it can only shift it. If the shaft asymmetry is increased the unstable regions for synchronous whirl become wider.

1.3 Organization of the thesis

The present investigations deal with a new discretization model of an anisotropic rotor. The rotor has different orientation along the shaft and is supported by rigid bearings or anisotropic flexible bearings. The models are investigated at both, stationary at constant rotational speed and non-stationary at acceleration through its critical speeds. Because of the difference in the orientation in each element of the shaft, the rotor must be modelled by using an approach of an asymmetric bending of shaft.

The thesis is structured as follows:

Chapter 2 deals with the theoretical model of anisotropic shaft with single disk and different shaft orientations. Here, some mathematical formulations are derived by using the strain energy method for asymmetric bending of a beam in order to obtain the equations of an asymmetric bending rotor stiffness. Two types of rotor models are considerd corresponding to different supports, rigid and anisotropic flexible bearings. Each model uses only one element to discretize each shaft section. Furthermore, the differential equations of rotor motion are solved numerically and eigenvalue analyses and stability charts are presented.

Chapter 3 concerns an extended formulation of Chapter 2, in which the mathematical model of an anisotropic rotor is extended to a general mathematical anisotropic rotor model having multiple degrees of freedom with different shaft orientations. The model can use one or more elements with different orientations to discretize each shaft section. Example rotors with two disks that are supported by rigid or anisotropic flexible bearings are simulated numerically. Additionally, an approach of a twisted anisotropic shaft with two disks is developed and analyzed with the minimal number of discrete shaft elements and a high number of discrete shaft elements. The eigenvalues analyses and stability charts of these models are ilustrated.

Furthermore, because of some difficulties in manufacturing and experimental setup, only one model of the rotor case is verified experimentally and the results are documented in Chapter 4. Here, the apparatus setup, the procedure of measurement and the signal processing is described. The stability investigation of the rotor is conducted at constant angular speed and constant angular acceleration experimentally. The experimental result is compared to the numerical result and presented in a spectral map and a spectrogram.

Finally, a summary of the results and an outlook to future work are given in the Chapter 5.

Chapter 2

Anisotropic shaft with single disk and different shaft orientation

Generally, an anisotropic rotor system can be modelled both in a fixed and in a rotating reference frames. In a fixed reference frame, the dynamic parameter especially the shaft stiffness is time-variant. If the rotor is modelled in a rotating reference frame, where the coordinate system follows the rotation of the shaft, then the differential equations of the system become speed-dependent. Hence, at constant rotational speed, the dynamic parameters of the rotor can be considered constant. If an anisotropic rotor is supported by anisotropic flexible bearings, the system stiffness must be a time-variant parameter whether the rotor is modelled in a fixed or in a rotating reference frame. Thus, the mathematical model is more complicated. In another case, if the rotor has variable orientation along the shaft (i.e. a twisted anisotropic rotor), the directions of the principal axes of cross-sections are not uniform along the shaft. In order to simplify the model, an approach with discrete shaft elements is used for which the shaft will behave like system at asymmetric bending.

2.1 Modelling of anisotropic rotor system

In this section, an anisotropic rotor is modelled consisting of a rigid disk and a massless shaft with two different support conditions. Because of different orientations of principal axes along the shaft, the model is approached by using discrete elements. Each element has different stiffness values in vertical and horizontal directions. The principal axes of each element have different orientations as shown in Figure 2.1a for a rotor supported by rigid bearings and in Figure 2.2a for a rotor supported by anisotropic flexible bearings, hence the principal axis of the cross-section along the shaft generally is unknown or changed. In order to simplify the model, some assumptions on each element are used as outlined in the following:

- coordinate of shaft element is considered in rotating reference frame,

- line axis of element lies in the x-axis,
- line axis of element coincides with the axis of the shear centre,
- cross-section of each element is constant,
- element is assumed to be massless,
- deformation is small and there is no non-linearity in geometry,
- material is linear-elastic and obeys HOOKE's law,
- forces and displacements are acting only at node,
- torsional vibration is not considered, and
- effects of temperature and shear deformation are neglected.

The first system model is an anisotropic rotor supported by rigid bearings. A rigid disk is attached at a node (i.e. the joint of two elements) at the distance ℓ_1 from the left bearing L_1 or ℓ_2 from the right bearing L_2 as shown in Figure 2.1a. By using the minimal number of elements, the rotor is discretized into two elements with the length ℓ_1 and ℓ_2, respectively. Therefore, the mathematical model can be simplified and possesses only four degrees of freedom, where the vibration of the shaft comes from only the motions of the disk. For further investigation, this model will be discussed in Section 2.5. As a point of interest, although the disk is attached symmetrically on the shaft ($\ell_1 = \ell_2$) and all elements have the same cross-sectional moment of inertia, but because of different orientation between the shaft elements, the disk position makes a precession. In this case, the effect of gyroscopic moments is no longer negligible. The derivation of gyroscopic moments will be presented in Section 2.2.

Furthermore, in the second modelling, a system is investigated as an anisotropic rotor supported by anisotropic flexible bearings as shown in Figure 2.2a. In this case, besides the anisotropy in each bearing, it is possible that the deflections between the left and the right bearing are different. Therefore, the effect of gyroscopic moments can be increased or decreased. For further investigation, this model will be discussed in Section 2.6.

The model shown in Figure 2.1b or 2.2b is a cross-section of the rotor in deflected condition with coordinates (y_W, z_W) in fixed frame or (η_W, ζ_W) in rotating reference frame. In this position, the rotating frame rotates with the angle φ which is a function of time. In the analysis, the rotating frame is assumed to rotate at constant angular velocity or constant angular acceleration.

If a constant angular acceleration is denoted as $\ddot{\varphi} = \alpha$, then

$$\dot{\varphi} = \alpha\, t + \Omega \qquad \text{and} \qquad \varphi = \frac{1}{2}\alpha\, t^2 + \Omega\, t + \gamma \quad . \tag{2.1}$$

Based on the Figure 2.1 or 2.2, if the rotor is assumed that has the minimal number of discrete elements (i.e. shaft with two elements only) the symbol of the subscribe k has a value 1 or 2. Furthermore, the coordinate systems of the principal axes of the first and the second shaft element are placed on the η_1^*-ζ_1^*-plane inclined at an angle β_1 and the η_2^*-ζ_2^*-plane at angle β_2. The center of gravity S of the disk is eccentric to the center of the shaft W and its position being defined by the eccentricity ε and the angular position ϕ. The kinematic relationships between the center of gravity and the center of shaft are

$$z_S = z_W + \varepsilon\ \cos(\varphi + \phi) \qquad \text{and} \qquad y_S = y_W + \varepsilon\ \sin(\varphi + \phi) \quad . \tag{2.2}$$

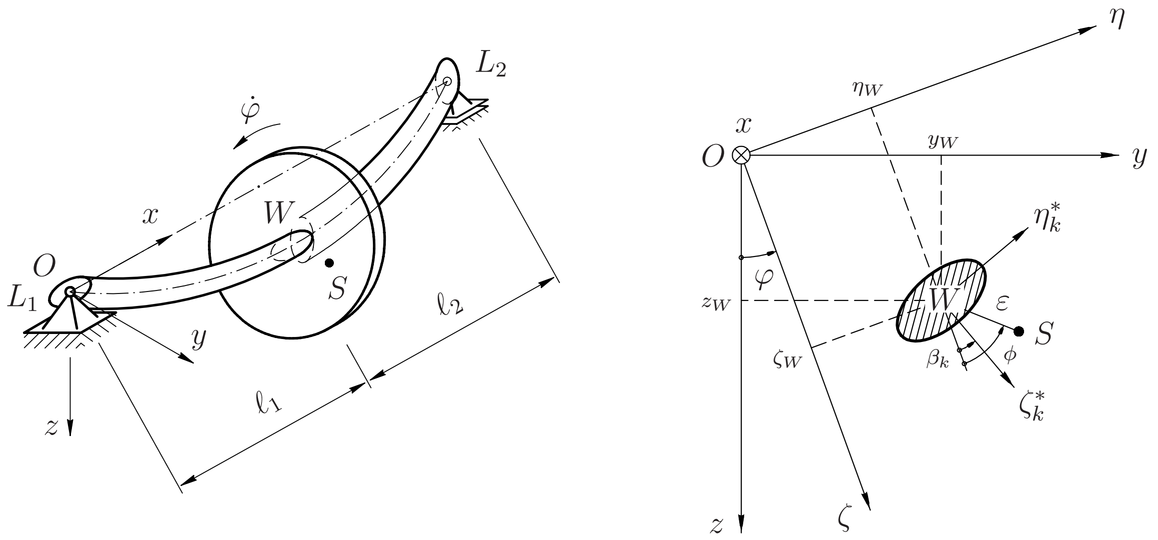

(a) (b)

Figure 2.1: Anisotropic rotor with different shaft orientation supported by rigid bearings

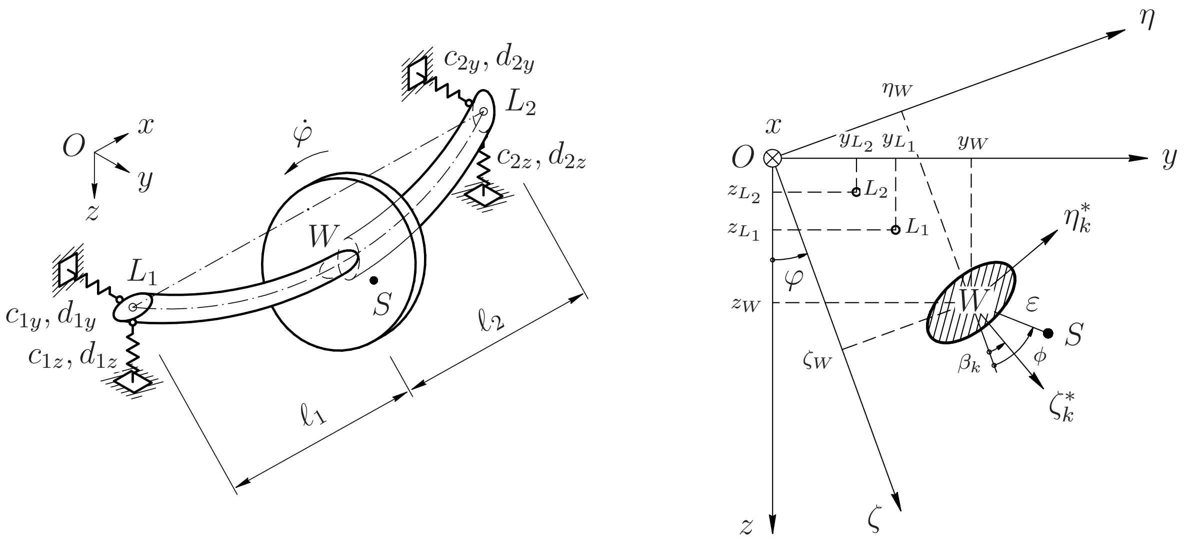

(a) (b)

Figure 2.2: Anisotropic rotor with different shaft orientation supported by anisotropic flexible bearings

Furthermore, the kinematic relationships between coordinates of principal axes and rotating reference frame of the k^{th}-shaft element can be determined by using the following transformation equations

$$\zeta_k = \zeta_k^* \cos\beta_k - \eta_k^* \sin\beta_k \qquad \text{and} \qquad \eta_k = \zeta_k^* \sin\beta_k + \eta_k^* \cos\beta_k \tag{2.3}$$

and between rotating and fixed reference frames can be determined by using transformation equations as follows

$$z = \zeta \cos\varphi - \eta \sin\varphi \qquad \text{and} \qquad y = \zeta \sin\varphi + \eta \cos\varphi \quad . \tag{2.4}$$

If a force acts on the rotor in arbitrary direction then this force is projected as F_ζ in ζ-direction and as F_η in η-direction. Furthermore, because of different shaft orientations, the force F_ζ is projected again on the first element to $F_{\zeta_1^*}$ and $F_{\eta_1^*}$ and on the second element to $F_{\zeta_2^*}$ and $F_{\eta_2^*}$. In the same way, the force F_η is projected on the first element to $F_{\zeta_1^*}$ and $F_{\eta_1^*}$ and is projected on the second element to $F_{\zeta_2^*}$ and $F_{\eta_2^*}$. Furthermore, if the resultant of forces in ζ_1^*-direction or ζ_2^*-direction has a positive value, then bending moment $M_{1\eta^*}$ or $M_{2\eta^*}$ will have a positive value. On the contrary, if resultant of forces in η_1^*-direction or η_2^*-direction has a positive value, then bending moment $M_{1\zeta^*}$ or $M_{2\zeta^*}$ will have negative value. In a moment diagram, the bending moments can be depicted as shown in Figure 2.3.

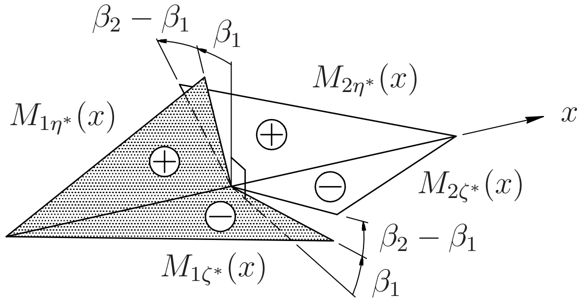

Figure 2.3: Bending moments in anisotropic rotor with different shaft orientation

In order to simplify the mathematical model, the moments of inertia of cross-section in principal axes of shaft elements should be transformed to rotating reference frame by using the following equations

$$I_{k\zeta} = \int \eta_k^2 \, dA = \frac{1}{2}\left(I_{k\eta^*} + I_{k\zeta^*}\right) - \frac{1}{2}\left(I_{k\eta^*} - I_{k\zeta^*}\right)\cos 2\beta_k - I_{k\eta^*\zeta^*}\sin 2\beta_k \tag{2.5}$$

$$I_{k\eta} = \int \zeta_k^2 \, dA = \frac{1}{2}\left(I_{k\eta^*} + I_{k\zeta^*}\right) + \frac{1}{2}\left(I_{k\eta^*} - I_{k\zeta^*}\right)\cos 2\beta_k + I_{k\eta^*\zeta^*}\sin 2\beta_k \tag{2.6}$$

$$I_{k\eta\zeta} = -\int \eta_k \zeta_k \, dA = -\frac{1}{2}\left(I_{k\eta^*} - I_{k\zeta^*}\right)\sin 2\beta_k + I_{k\eta^*\zeta^*}\cos 2\beta_k \quad . \tag{2.7}$$

However, in order to obtain the simplest differential equations of system, here the mathematical model of the system is presented only in rotating reference frame.

2.2 Gyroscopic moments

The differential equations of anisotropic rotor supported by rigid bearings have been formulated by WALTER [49]. In this research, the effects of the gyroscopic moments are taken into account. Based on this reference, the following formulations are developed for an anisotropic rotor supported by anisotropic flexible bearings. As shown in Figure 2.4, the disk on a shaft is described in the coordinate system (x', y', z'), where the plane of disk is parallel to the y'-z'-plane. The x'-axis is perpendicular to that plane. Furthermore, y'-axis can move only in the x-y-plane and z'-axis in the x-z-plane, therefore y'-axis and z'-axis can be not-perpendicular, where their position can make precessions φ_z and φ_y, respectively. This means the coordinate system (x', y', z') is no longer orthonormal. Because the rotor system is supported by anisotropic flexible bearings, the precessions φ_y and φ_z occur not only due to the slope of the shaft at deflection in the left and in the right bearings, but also by slope of the deflected shaft, hence

$$\varphi_y = \varphi_{y_W} + \varphi_{y_L} \qquad \text{and} \qquad \varphi_z = \varphi_{z_W} + \varphi_{z_L} \quad , \tag{2.8}$$

where φ_{y_W} and φ_{z_W} are the slopes of the disk due to the axis of the shaft in undeflected condition in the x-z and x-y-plane, respectively (i.e. the precessions are occured only by shaft deflection). The φ_{y_L} and φ_{z_L} are the precessions that come from the slope of the shaft due to the deflection in the left and the right bearing.

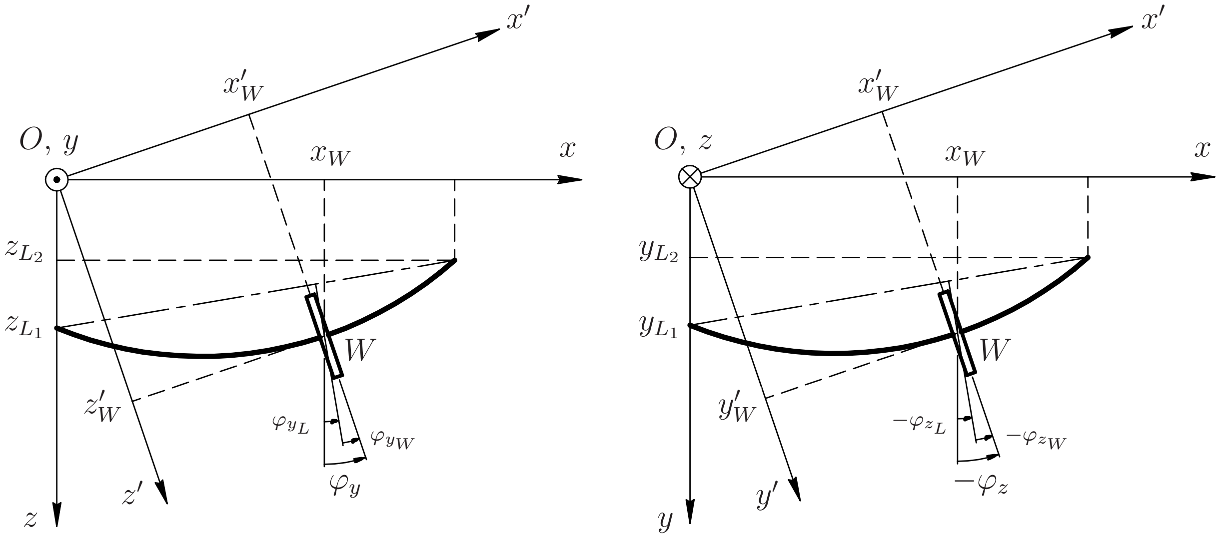

Figure 2.4: Coordinate of disk in anisotropic rotor-bearings system

From the Figure 2.4, the transformation equations of basis vectors are obtained

$$\begin{aligned} \vec{e}_{z'} &= \sin\varphi_y\,\vec{e}_x + \cos\varphi_y\,\vec{e}_z \\ \vec{e}_{y'} &= -\sin\varphi_z\,\vec{e}_x + \cos\varphi_z\,\vec{e}_y \end{aligned} \tag{2.9}$$

$$\vec{e}_{x'} = \frac{\vec{e}_{y'} \times \vec{e}_{z'}}{|\,\vec{e}_{y'} \times \vec{e}_{z'}|} = \frac{\vec{e}_x + \tan\varphi_z\,\vec{e}_y - \tan\varphi_y\,\vec{e}_z}{\sqrt{1+\tan^2\varphi_y+\tan^2\varphi_z}} \quad .$$

The first step is to determine the kinematic relationships of angular velocities in (x', y', z')-coordinate system. If angular speed of the disk is denoted by ω_s in the (x', y', z')-coordinate system, the y'-z'-plane that rotates along the x'-axis is denoted by ω_E and $\dot{\varphi}$ is the rotational speed of the shaft, then

$$\omega_s = \omega_E - \dot{\varphi}\,\vec{e}_{x'} \quad . \tag{2.10}$$

Furthermore, angular speed of basis vector $\vec{e}_{y'}$ is

$$\omega(\vec{e}_{y'}) = \dot{\varphi}_{x'}(\vec{e}_{y'})\,\vec{e}_{x'} + \dot{\varphi}_{y'}(\vec{e}_{y'})\,\vec{e}_{y'} + \dot{\varphi}_{z'}(\vec{e}_{y'})\,\vec{e}_{z'} \quad . \tag{2.11}$$

The expression in parenthesis is not a function argument but an alternative index. For an example, the $\dot{\varphi}_{x'}(\vec{e}_{y'})\,\vec{e}_{x'}$ means the rotational speed of the vector $\vec{e}_{x'}$ due to y'-axis. Because the plane of disk is placed at the y'-z'-plane and the precession φ_z is the angle of the plane of disk with respect to the z-axis, hence

$$\omega(\vec{e}_{y'}) = \dot{\varphi}_z\,\vec{e}_z \quad . \tag{2.12}$$

Therefore, the Equation (2.11) can be rearranged in matrix notation as

$$\begin{bmatrix} \dfrac{1}{\sqrt{1+\tan^2\varphi_y+\tan^2\varphi_z}} & -\sin\varphi_z & \sin\varphi_y \\ \dfrac{\tan\varphi_z}{\sqrt{1+\tan^2\varphi_y+\tan^2\varphi_z}} & \cos\varphi_z & 0 \\ -\dfrac{\tan\varphi_y}{\sqrt{1+\tan^2\varphi_y+\tan^2\varphi_z}} & 0 & \cos\varphi_y \end{bmatrix} \begin{bmatrix} \dot{\varphi}_{x'}(\vec{e}_{y'}) \\ \dot{\varphi}_{y'}(\vec{e}_{y'}) \\ \dot{\varphi}_{z'}(\vec{e}_{y'}) \end{bmatrix} = \begin{bmatrix} 0 \\ 0 \\ \dot{\varphi}_z \end{bmatrix} \tag{2.13}$$

and angular speed of basis vector $\vec{e}_{z'}$ is

$$\omega(\vec{e}_{z'}) = \dot{\varphi}_{x'}(\vec{e}_{z'})\,\vec{e}_{x'} + \dot{\varphi}_{y'}(\vec{e}_{z'})\,\vec{e}_{y'} + \dot{\varphi}_{z'}(\vec{e}_{z'})\,\vec{e}_{z'} \quad . \tag{2.14}$$

Similar to the Equation (2.12), the precession φ_y is the angle of the plane of disk with respect to the y-axis, hence

$$\omega(\vec{e}_{z'}) = \dot{\varphi}_y\,\vec{e}_y \tag{2.15}$$

and in matrix notation the Equation (2.14) can be rearranged as

$$\begin{bmatrix} \dfrac{1}{\sqrt{1+\tan^2\varphi_y+\tan^2\varphi_z}} & -\sin\varphi_z & \sin\varphi_y \\ \dfrac{\tan\varphi_z}{\sqrt{1+\tan^2\varphi_y+\tan^2\varphi_z}} & \cos\varphi_z & 0 \\ -\dfrac{\tan\varphi_y}{\sqrt{1+\tan^2\varphi_y+\tan^2\varphi_z}} & 0 & \cos\varphi_y \end{bmatrix} \begin{bmatrix} \dot{\varphi}_{x'}(\vec{e}_{z'}) \\ \dot{\varphi}_{y'}(\vec{e}_{z'}) \\ \dot{\varphi}_{z'}(\vec{e}_{z'}) \end{bmatrix} = \begin{bmatrix} 0 \\ \dot{\varphi}_y \\ 0 \end{bmatrix} \quad . \tag{2.16}$$

By using the Cramer's rule, angular speeds $\dot{\varphi}_{x'}(\vec{e}_{y'})$, $\dot{\varphi}_{y'}(\vec{e}_{y'})$, $\dot{\varphi}_{z'}(\vec{e}_{y'})$, $\dot{\varphi}_{x'}(\vec{e}_{z'})$, $\dot{\varphi}_{y'}(\vec{e}_{z'})$ and $\dot{\varphi}_{z'}(\vec{e}_{z'})$ of the basis vectors can be determined to

$$\begin{aligned}
\dot{\varphi}_{x'}(\vec{e}_{y'}) &= -\frac{\tan\varphi_y}{\sqrt{1+\tan^2\varphi_y+\tan^2\varphi_z}}\,\dot{\varphi}_z \\
\dot{\varphi}_{y'}(\vec{e}_{y'}) &= \frac{\tan\varphi_y\tan\varphi_z}{\cos\varphi_z(1+\tan^2\varphi_y+\tan^2\varphi_z)}\,\dot{\varphi}_z \\
\dot{\varphi}_{z'}(\vec{e}_{y'}) &= \frac{1}{\cos\varphi_y\cos^2\varphi_z(1+\tan^2\varphi_y+\tan^2\varphi_z)}\,\dot{\varphi}_z \\
\dot{\varphi}_{x'}(\vec{e}_{z'}) &= \frac{\tan\varphi_z}{\sqrt{1+\tan^2\varphi_y+\tan^2\varphi_z}}\,\dot{\varphi}_y \\
\dot{\varphi}_{y'}(\vec{e}_{z'}) &= \frac{1}{\cos^2\varphi_y\cos\varphi_z(1+\tan^2\varphi_y+\tan^2\varphi_z)}\,\dot{\varphi}_y \\
\dot{\varphi}_{z'}(\vec{e}_{z'}) &= \frac{\tan\varphi_y\tan\varphi_z}{\cos\varphi_y(1+\tan^2\varphi_y+\tan^2\varphi_z)}\,\dot{\varphi}_y \quad .
\end{aligned} \tag{2.17}$$

Based on the Figure 2.4, it is clear that the angular speed of the y'-z'-plane is the rotational speed of the vector $\vec{e}_{y'}$ due to z'-axis and the rotational speed of the vector $\vec{e}_{z'}$ due to y'-axis, hence the angular speed in Equation (2.10) can be reformulated as

$$\omega_E = \dot{\varphi}_{y'}(\vec{e}_{z'})\,\vec{e}_{y'} + \dot{\varphi}_{z'}(\vec{e}_{y'})\,\vec{e}_{z'} \tag{2.18}$$

and by inserting Equations (2.17) and (2.18) into Equation (2.10),

$$\begin{aligned}
\omega_s = -\dot{\varphi}\,\vec{e}_{x'} &+ \frac{1}{\cos^2\varphi_y\cos\varphi_z(1+\tan^2\varphi_y+\tan^2\varphi_z)}\,\dot{\varphi}_y\,\vec{e}_{y'} \\
&+ \frac{1}{\cos\varphi_y\cos^2\varphi_z(1+\tan^2\varphi_y+\tan^2\varphi_z)}\,\dot{\varphi}_z\,\vec{e}_{z'} \quad .
\end{aligned} \tag{2.19}$$

Furthermore, the vector of angular momentum can be calculated

$$L = \Theta\,\omega_s \quad . \tag{2.20}$$

If φ_y and φ_z are assumed to be small then

$$L = (-\Theta_p\dot{\varphi})\,\vec{e}_x + (-\Theta_p\dot{\varphi}\varphi_z + \Theta_a\dot{\varphi}_y)\,\vec{e}_y + (\Theta_p\dot{\varphi}\varphi_y + \Theta_a\dot{\varphi}_z)\,\vec{e}_z \quad . \tag{2.21}$$

The time derivative of angular momentum can be rewritten in two ways:

1. in fixed reference frame as

$$\frac{dL}{dt} = (-\Theta_p\ddot{\varphi})\,\vec{e}_x + (-\Theta_p\ddot{\varphi}\varphi_z - \Theta_p\dot{\varphi}\dot{\varphi}_z + \Theta_a\ddot{\varphi}_y)\,\vec{e}_y + (\Theta_p\ddot{\varphi}\varphi_y + \Theta_p\dot{\varphi}\dot{\varphi}_y + \Theta_a\ddot{\varphi}_z)\,\vec{e}_z \tag{2.22}$$

2. in rotating reference frame as

$$\begin{aligned}
\frac{dL}{dt} = (-\Theta_p\ddot{\varphi})\,\vec{e}_x &+ \left[\Theta_p(\ddot{\varphi}\varphi_\eta + \dot{\varphi}^2\varphi_\zeta + \dot{\varphi}\dot{\varphi}_\eta) + \Theta_a(\ddot{\varphi}_\zeta - \dot{\varphi}^2\varphi_\zeta - 2\dot{\varphi}\dot{\varphi}_\eta - \ddot{\varphi}\varphi_\eta)\right]\vec{e}_\zeta \\
&+ \left[\Theta_p(-\ddot{\varphi}\varphi_\zeta + \dot{\varphi}^2\varphi_\eta - \dot{\varphi}\dot{\varphi}_\zeta) + \Theta_a(\ddot{\varphi}_\eta - \dot{\varphi}^2\varphi_\eta + 2\dot{\varphi}\dot{\varphi}_\zeta + \ddot{\varphi}\varphi_\zeta)\right]\vec{e}_\eta \quad .
\end{aligned} \tag{2.23}$$

2.3 Asymmetric bending

It is well known that if a beam is loaded by an external force not in the direction of the principal axes of beam cross-section, then its deflection will not be parallel to the direction of the force. This phenomenon is well known as asymmetric bending ([14], [33]).

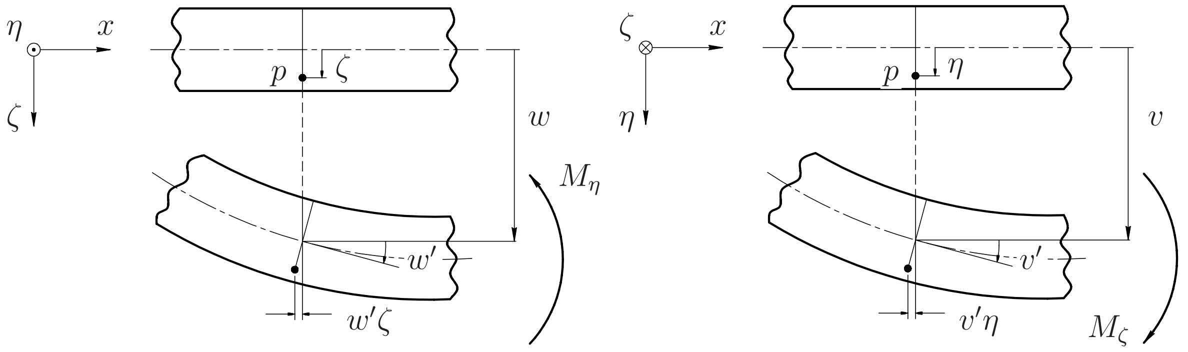

Figure 2.5: Kinematics of deflected beam

Figure 2.5 depicts the kinematics of asymmetric bending of deflected beam. If a beam is loaded by a force, the bending moments will occur in both η and ζ-direction directly. Furthermore, the displacement of point p in x-direction can be defined as

$$u_p(x,\eta,\zeta) = u(x) - w'(x)\,\zeta - v'(x)\,\eta \quad . \tag{2.24}$$

If the differentiation of point p due to differentiation of x is considered, then the elongation of point p in x-direction is obtained.

$$\varepsilon_x(x,\eta,\zeta) = \frac{\partial u_p(x,\eta,\zeta)}{\partial x} = u'(x) - w''(x)\,\zeta - v''(x)\,\eta \quad . \tag{2.25}$$

Furthermore, by assuming the HOOKE's law

$$\sigma_x = E\varepsilon_x(x,\eta,\zeta) \quad , \tag{2.26}$$

where E is YOUNG's modulus of the beam material, the normal stress of the beam can be determined to

$$\sigma_x = Eu'(x) - Ew''(x)\,\zeta - Ev''(x)\,\eta \quad . \tag{2.27}$$

Based on the Equation (2.27), if the area of beam cross-section is defined as A then the normal force can be obtained

$$N(x) = \int_{(A)} \sigma_x \, dA = EA\,u'(x) \quad . \tag{2.28}$$

With the assumption that no normal force acts on the beam, the normal stresses which act on the beam come only from bending moments M_η and M_ζ, where

$$M_\eta(x) = \int_{(A)} \zeta\, \sigma_x \, dA = -EI_\eta w''(x) + EI_{\eta\zeta} v''(x) \tag{2.29}$$

and

$$M_\zeta(x) = -\int_{(A)} \eta\, \sigma_x \, dA = -EI_{\eta\zeta} w''(x) + EI_\zeta v''(x) \quad . \tag{2.30}$$

Furthermore, by elimination of the Equation (2.29) and (2.30), the second differentiation of deflection in ζ and η-directions are obtained

$$w''(x) = -\frac{I_\zeta}{E\left(I_\eta I_\zeta - I_{\eta\zeta}^2\right)} M_\eta(x) + \frac{I_{\eta\zeta}}{E\left(I_\eta I_\zeta - I_{\eta\zeta}^2\right)} M_\zeta(x) \tag{2.31}$$

$$v''(x) = -\frac{I_{\eta\zeta}}{E\left(I_\eta I_\zeta - I_{\eta\zeta}^2\right)} M_\eta(x) + \frac{I_\eta}{E\left(I_\eta I_\zeta - I_{\eta\zeta}^2\right)} M_\zeta(x) \quad . \tag{2.32}$$

2.4 Strain energy in asymmetric bending

It is well known that if an elastic body or beam is loaded by a force then that body will be deformed. With the assumption that no energy is converted to heat, the external work will be absorbed by the body in form of internal strain energy, where

$$W = U \quad . \tag{2.33}$$

If one is interested in the normal stress in x-direction which comes only from bending moments, the equation of strain energy in the beam can be formulated in a double-integral as

$$U = \frac{1}{2} \int_{(\ell)} \int_{(A)} \sigma_x \, \varepsilon_x(x, \eta, \zeta) \; dA \, dx \quad . \tag{2.34}$$

Since the Equation (2.34) is extended by using substitution from Equations (2.25) and (2.27) without factor $u'(x)$ into the Equation (2.34), the internal strain energy becomes

$$U = \frac{1}{2} \int_{(\ell)} \left[EI_\eta \, w''(x) \, w''(x) + EI_\zeta \, v''(x) \, v''(x) - 2EI_{\eta\zeta} \, w''(x) \, v''(x) \right] \, dx \quad . \tag{2.35}$$

Furthermore, if the Equation (2.35) is abbreviated by the Equations (2.29) and (2.30) then the internal strain energy as a function of bending moments is obtained

$$U = \frac{1}{2} \int_{(\ell)} -M_\eta \, w''(x) + M_\zeta \, v''(x) \; dx \quad . \tag{2.36}$$

Finally, if the Equations (2.31) and (2.32) are substituted into the Equation (2.36) then the internal strain energy as a function of bending moments in asymmetric bending is obtained

$$U = \frac{1}{2} \int_{(\ell)} \frac{I_\zeta}{E\left(I_\eta I_\zeta - I_{\eta\zeta}^2\right)} M_\eta^2(x) \; dx \; + \; \frac{1}{2} \int_{(\ell)} \frac{I_\eta}{E\left(I_\eta I_\zeta - I_{\eta\zeta}^2\right)} M_\zeta^2(x) \; dx$$

$$- \int_{(\ell)} \frac{I_{\eta\zeta}}{E\left(I_\eta I_\zeta - I_{\eta\zeta}^2\right)} M_\eta(x)\, M_\zeta(x)\ dx \quad . \tag{2.37}$$

The Equation (2.37) consists of three integral components, where the first and the second integral can be used to obtain the internal strain energy for the same plane of works (e.g. the works of the forces in ζ or in η-direction with the displacements in ζ or in η-direction, respectively). The first or the second integral components is called as active internal strain energy. The third integral component can be used to obtain the internal strain energy for the different plane of works (e.g. the works of the forces in ζ-direction with the displacements in η-direction or reciprocally). The third integral component is called pasive internal strain energy.

If the Equation (2.37) is extended, where M_η consists of $M_{i\eta}$ and $M_{j\eta}$ and M_ζ consists of $M_{i\zeta}$ and $M_{j\zeta}$, they can be rewritten as

$$M_\eta^2 = \left(M_{i\eta} + M_{j\eta}\right)^2 = M_{i\eta}^2 + M_{j\eta}^2 + 2M_{i\eta}M_{j\eta} \tag{2.38}$$

$$M_\zeta^2 = \left(M_{i\zeta} + M_{j\zeta}\right)^2 = M_{i\zeta}^2 + M_{j\zeta}^2 + 2M_{i\zeta}M_{j\zeta} \tag{2.39}$$

or for k^{th}-element of bending moment in η-direction can be written as

$$M_{k\eta}^2 = \left(M_{ik\eta} + M_{jk\eta}\right)^2 = M_{ik\eta}^2 + M_{jk\eta}^2 + 2M_{ik\eta}M_{jk\eta} \tag{2.40}$$

and in ζ-direction as

$$M_{k\zeta}^2 = \left(M_{ik\zeta} + M_{jk\zeta}\right)^2 = M_{ik\zeta}^2 + M_{jk\zeta}^2 + 2M_{ik\zeta}M_{jk\zeta} \quad . \tag{2.41}$$

With Equations (2.40) and (2.41), the Equation (2.37) can be written as

$$U = U_{ii\zeta} + U_{jj\zeta} + U_{ij\zeta} + U_{ii\eta} + U_{jj\eta} + U_{ij\eta} + \bar{U}_{ii\eta\zeta} + \bar{U}_{jj\eta\zeta} + \bar{U}_{ij\eta\zeta} \quad , \tag{2.42}$$

where $\bar{U}$ denotes the passive internal strain energy.

Based on the MAXWELL-BETTI reciprocal work theorem which has been used in the similar case in [24], the internal strain energy of the system can be written by using the relationship of flexibility equation, hence

$$\begin{aligned} U = {} & \frac{1}{2}\, h_{ii\zeta} f_{i\zeta}^2 + \frac{1}{2}\, h_{jj\zeta} f_{j\zeta}^2 + h_{ij\zeta} f_{i\zeta} f_{j\zeta} + \frac{1}{2}\, h_{ii\eta} f_{i\eta}^2 + \frac{1}{2}\, h_{jj\eta} f_{j\eta}^2 + h_{ij\eta} f_{i\eta} f_{j\eta} \\ & + \frac{1}{2}\, h_{ii\eta\zeta} \bar{f}_{i\eta} f_{i\zeta} + \frac{1}{2}\, h_{jj\eta\zeta} \bar{f}_{j\eta} f_{j\zeta} + h_{ij\eta\zeta} \bar{f}_{j\eta} f_{i\zeta} \quad , \end{aligned} \tag{2.43}$$

where h and f are defined as flexibility influence coefficient and normalized acting force, respectively. The explicit expressions of the flexibility influence coefficients can be found in the Appendix A.1.

2.5 Dynamic parameters of anisotropic rotor supported by rigid bearings

In an anisotropic rotor model, the mass of the shaft is assumed to be small compared to the disk mass. This system is not only influenced by gyroscopic moments but also both by internal viscous damping forces of the shaft and by external proportional damping forces due to velocity of the disk.

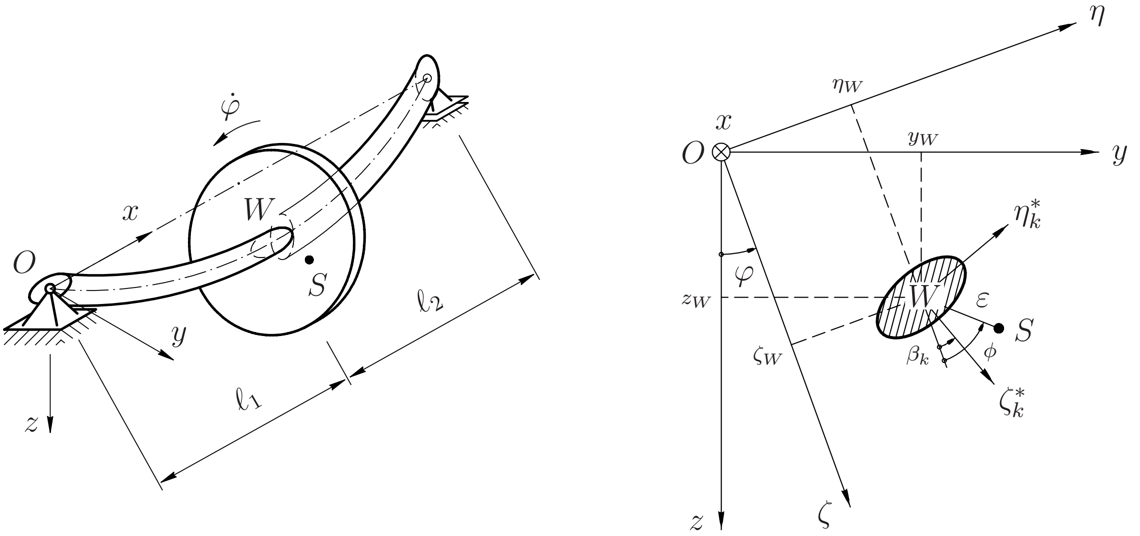

(a) (b)

Figure 2.6: Anisotropic rotor with different shaft orientations supported by rigid bearings

The authors in [11], [28] and [34] have formulated the differential equations of rotor supported by rigid bearings, where the equations of system motion can be considered by using the system reference at the centre of gravitation of the system S or at the centre of rotating shaft W. However, the point W is easier to determine experimentally, hence a model with the reference of centre of rotating shaft W is preferred in the mathematical model.

For the case in Figure 2.6, the rotor model has a node which has four degrees of freedom, those are two translational y, z or η, ζ and two rotational φ_y, φ_z or $\varphi_\zeta, \varphi_\eta$ degrees of freedom. The shaft is modelled by discrete elements. Because of different shaft orientations and by using the minimal number of elements, the shaft is devided into two elements. The positive sign rule is used in numbering of the node of the shaft, the forces and the displacements. The first step is to number the displacement and force in translational direction i.e. in ζ-axis and then in η-axis. The next step is to number the rotational displacements and moments in ζ-axis and then η-axis as shown in Figure 2.7.

In the model, the gravitational force is taken into account. The gravitational force in rotating reference frame is

$$F_g = mg\cos\varphi\,\vec{e}_\zeta - mg\sin\varphi\,\vec{e}_\eta \tag{2.44}$$

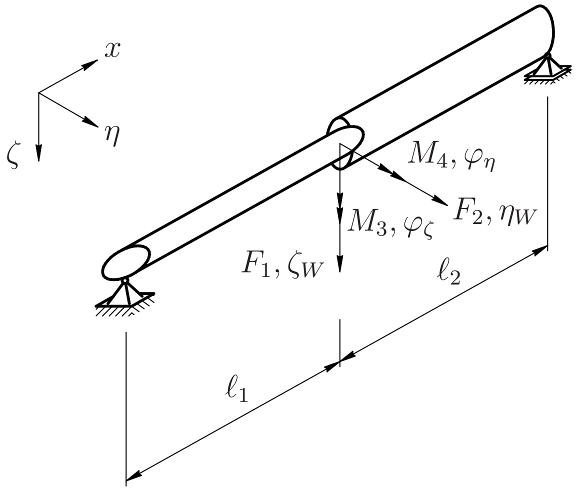

Figure 2.7: Rotor model 4-DoF with the minimal number of discrete elements

or in matrix notation the Equation (2.44) is rewritten in a column matrix as

$$\boldsymbol{p}_g = \begin{bmatrix} mg\cos\varphi \\ -mg\sin\varphi \\ 0 \\ 0 \end{bmatrix} \quad . \tag{2.45}$$

2.5.1 Flexibility matrix

By deviding the bending moments $M_{ik\eta}$, $M_{jk\zeta}$ and $M_{ik\zeta}$, $M_{jk\eta}$ in k^{th}-element by forces $F_{i\zeta}$, $F_{j\eta}$ and by moments $M_{i\zeta}$, $M_{j\eta}$, respectively, the normalized bending moments are obtained

$$\begin{aligned} \hat{M}_{ik\eta}(x) &= \frac{M_{ik\eta}(x)}{F_{i\zeta}} \qquad & \hat{M}_{jk\zeta}(x) &= \frac{M_{jk\zeta}(x)}{F_{j\eta}} \\ \hat{M}_{jk\eta}(x) &= \frac{M_{jk\eta}(x)}{M_{j\eta}} \qquad & \hat{M}_{ik\zeta}(x) &= \frac{M_{ik\zeta}(x)}{M_{i\zeta}} \quad . \end{aligned} \tag{2.46}$$

For the model which consists of four degrees of freedom with the minimal number of discrete elements, the equations of bending moments under the forces F_1 and F_2 as the functions of the shaft position x can be formulated based on Figure 2.8, thus

$$\begin{aligned} \hat{M}_{11\eta}(x) &= \frac{\ell_2}{\ell}x \qquad & \hat{M}_{21\zeta}(x) &= -\frac{\ell_2}{\ell}x \\ \hat{M}_{12\eta}(x) &= -\frac{\ell_1}{\ell}x + \frac{\ell_1\ell_2}{\ell} \qquad & \hat{M}_{22\zeta}(x) &= \frac{\ell_1}{\ell}x - \frac{\ell_1\ell_2}{\ell} \end{aligned} \tag{2.47}$$

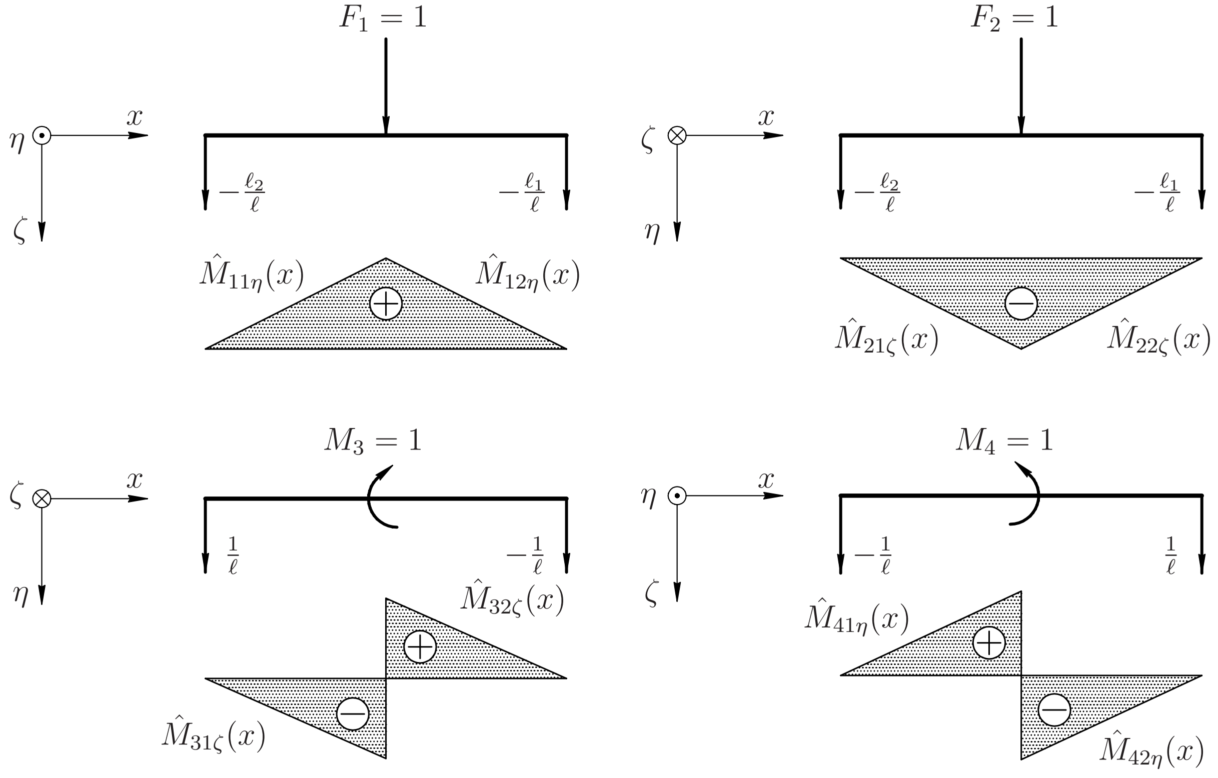

Figure 2.8: Bending moments in anisotropic rotor

and the equations of bending moments under the moments M_3 and M_4 are obtained as the functions of the position x as

$$\begin{aligned} \hat{M}_{31\zeta}(x) &= -\frac{x}{\ell} & \qquad \hat{M}_{41\eta}(x) &= \frac{x}{\ell} \\ \hat{M}_{32\zeta}(x) &= -\frac{x}{\ell} + \frac{\ell_2}{\ell} & \qquad \hat{M}_{42\eta}(x) &= \frac{x}{\ell} - \frac{\ell_2}{\ell} \quad . \end{aligned} \tag{2.48}$$

The flexibility influence coefficients of the shaft are obtained as follows

$$h_{ij} = \sum_{k=1}^{2} \int_{(\ell_k)} \frac{I_{k\zeta}}{E\left(I_{k\eta} I_{k\zeta} - I_{k\eta\zeta}^2\right)} \hat{M}_{ik\eta}(x)\, \hat{M}_{jk\eta}(x)\ dx \quad ; \text{for } i = 1,4 \text{ and } j = 1,4 \tag{2.49}$$

$$h_{ij} = \sum_{k=1}^{2} \int_{(\ell_k)} \frac{I_{k\eta}}{E\left(I_{k\eta} I_{k\zeta} - I_{k\eta\zeta}^2\right)} \hat{M}_{ik\zeta}(x)\, \hat{M}_{jk\zeta}(x)\ dx \quad ; \text{for } i = 2,3 \text{ and } j = 2,3 \tag{2.50}$$

$$h_{ij} = \sum_{k=1}^{2} \int_{(\ell_k)} \frac{-I_{k\eta\zeta}}{E\left(I_{k\eta} I_{k\zeta} - I_{k\eta\zeta}^2\right)} \hat{M}_{ik\eta}(x)\, \hat{M}_{jk\zeta}(x)\ dx \quad ; \text{for } i = 1,4 \text{ and } j = 2,3. \tag{2.51}$$

After assembling of the flexibility influence coefficients as mentioned in the Equations (2.49)-(2.51), they can be arranged in a matrix with the size 4×4, thus

$$\boldsymbol{H} = \begin{bmatrix} h_{11} & h_{12} & h_{13} & h_{14} \\ h_{12} & h_{22} & h_{23} & h_{24} \\ h_{13} & h_{23} & h_{33} & h_{34} \\ h_{14} & h_{24} & h_{34} & h_{44} \end{bmatrix} \quad . \tag{2.52}$$

Furthermore, the stiffness matrix can be obtained as inverse of the flexibility matrix, hence

$$\boldsymbol{C}_W = \boldsymbol{H}^{-1} = \begin{bmatrix} c_{11} & c_{12} & c_{13} & c_{14} \\ c_{12} & c_{22} & c_{23} & c_{24} \\ c_{13} & c_{23} & c_{33} & c_{34} \\ c_{14} & c_{24} & c_{34} & c_{44} \end{bmatrix} \quad . \tag{2.53}$$

Shaft bending forces in rotating reference frame can be determined based on the stiffness matrix in the Equation (2.53). Because the shaft bending forces are reaction forces, these forces are written in negative sign , hence

$$\begin{bmatrix} F_{c1} \\ F_{c2} \\ M_{c3} \\ M_{c4} \end{bmatrix} = - \begin{bmatrix} c_{11} & c_{12} & c_{13} & c_{14} \\ c_{12} & c_{22} & c_{23} & c_{24} \\ c_{13} & c_{23} & c_{33} & c_{34} \\ c_{14} & c_{24} & c_{34} & c_{44} \end{bmatrix} \begin{bmatrix} \zeta_W \\ \eta_W \\ \varphi_\zeta \\ \varphi_\eta \end{bmatrix} \tag{2.54}$$

or rewritten in simple form

$$\boldsymbol{f}_c = -\boldsymbol{C}_W \, \boldsymbol{q}_W \quad . \tag{2.55}$$

2.5.2 Damping matrix

In considering of a damping coefficient of a structure, this damping is separated between internal and external damping. In [35] and [44], the internal damping is approached by a proportional damping due to mass matrix and stiffness matrix as RAYLEIGH damping, where

$$\boldsymbol{D}_i = \alpha_m \boldsymbol{M} + \alpha_c \boldsymbol{C}_W \quad , \tag{2.56}$$

with α_m and α_c are coefficients of proportional internal damping due to mass matrix and stiffness matrix, respectively.

If the coefficient of internal damping can be considered by using an assumption that the rotor system is in standby condition, where the rotor speed is still equal to zero, therefore the rotor system is still as a static system. In this case, the differential equation of the rotor refers to a general damped system in fixed reference frame

$$\boldsymbol{M} \ddot{\boldsymbol{q}} + \boldsymbol{D}_i \dot{\boldsymbol{q}} + \boldsymbol{C} \boldsymbol{q} = \boldsymbol{0} \quad . \tag{2.57}$$

By using an assumption of the CAUGHEY damping [35], the damping can be considered by using the orthogonality behavior of the eigenvectors of the system to obtain the uncoupled damping matrix.

Therefore, the transformation of coordinate is introduced

$$\boldsymbol{q} = \boldsymbol{\Phi} \, \boldsymbol{r} \quad , \tag{2.58}$$

where $\boldsymbol{\Phi}$ is the modal matrix or normalized eigenvectors and $\boldsymbol{r}$ is the modal matrix of displacements, thus uncoupled matrices of mass matrix, damping matrix and stiffness matrix are obtained as follows

$$\tilde{\boldsymbol{M}} = \boldsymbol{\Phi}^T \boldsymbol{M}\, \boldsymbol{\Phi}, \qquad \tilde{\boldsymbol{C}} = \boldsymbol{\Phi}^T \boldsymbol{C}\, \boldsymbol{\Phi} \qquad \text{and} \qquad \tilde{\boldsymbol{D}}_i = \boldsymbol{\Phi}^T \boldsymbol{D}_i\, \boldsymbol{\Phi} \quad . \tag{2.59}$$

Since the specified modal damping ratio D_i is known, the damping matrix has the relationship

$$\tilde{\boldsymbol{D}}_i = \begin{bmatrix} 2D_1\omega_1\tilde{M}_1 & 0 & 0 & 0 \\ 0 & 2D_2\omega_2\tilde{M}_2 & 0 & 0 \\ 0 & 0 & 2D_3\omega_3\tilde{M}_3 & 0 \\ 0 & 0 & 0 & 2D_4\omega_4\tilde{M}_4 \end{bmatrix} \tag{2.60}$$

In order to obtain the coupled damping matrix again, the Equation (2.60) should be premultiplied by inverse transpose of the modal matrix and postmultiplied by inverse of the modal matrix, hence

$$\boldsymbol{D}_i = \boldsymbol{\Phi}^{-T} \tilde{\boldsymbol{D}}_i\, \boldsymbol{\Phi}^{-1} \quad . \tag{2.61}$$

Furthermore, because the internal damping forces of the shaft in rotating reference frame are reaction damping forces of the system, they are denoted by a negative sign.

$$\begin{bmatrix} F_{i1} \\ F_{i2} \\ M_{i3} \\ M_{i4} \end{bmatrix} = - \begin{bmatrix} d_{11} & d_{12} & d_{13} & d_{14} \\ d_{12} & d_{22} & d_{23} & d_{24} \\ d_{13} & d_{23} & d_{33} & d_{34} \\ d_{14} & d_{24} & d_{34} & d_{44} \end{bmatrix} \begin{bmatrix} \dot{\zeta}_W \\ \dot{\eta}_W \\ \dot{\varphi}_\zeta \\ \dot{\varphi}_\eta \end{bmatrix} \tag{2.62}$$

or rewritten in simple form

$$\boldsymbol{f}_i = -\boldsymbol{D}_i\, \dot{\boldsymbol{q}}_W \quad . \tag{2.63}$$

For external damping, an approach of proportional damping due to absolute velocity of disk can be used. In fixed reference frame, the external damping force can be written as

$$F_a = -d_a \left(\dot{z}_S\, \vec{e}_z + \dot{y}_S\, \vec{e}_y \right) \tag{2.64}$$

or in rotating reference frame due to centre of shaft W, the equation can be formulated as

$$F_a = -d_a \left[\left(\dot{\zeta}_W - \dot{\varphi}\eta_W - \varepsilon\dot{\varphi}\sin\phi \right) \vec{e}_\zeta + \left(\dot{\eta}_W + \dot{\varphi}\zeta_W + \varepsilon\dot{\varphi}\cos\phi \right) \vec{e}_\eta \right] \quad , \tag{2.65}$$

where d_a is coefficient of proportional external damping.

In matrix notation the Equation (2.65) can be rearranged as

$$\begin{bmatrix} F_{a1} \\ F_{a2} \\ M_{a3} \\ M_{a4} \end{bmatrix} = - \begin{bmatrix} d_a & & & \\ & d_a & & \\ & & 0 & \\ & & & 0 \end{bmatrix} \begin{bmatrix} \dot{\zeta}_W \\ \dot{\eta}_W \\ \dot{\varphi}_\zeta \\ \dot{\varphi}_\eta \end{bmatrix} - \begin{bmatrix} 0 & -d_a\dot{\varphi} & 0 & 0 \\ d_a\dot{\varphi} & 0 & 0 & 0 \\ 0 & 0 & 0 & 0 \\ 0 & 0 & 0 & 0 \end{bmatrix} \begin{bmatrix} \zeta_W \\ \eta_W \\ \varphi_\zeta \\ \varphi_\eta \end{bmatrix} + \begin{bmatrix} d_a\varepsilon\dot{\varphi}\sin\phi \\ -d_a\varepsilon\dot{\varphi}\cos\phi \\ 0 \\ 0 \end{bmatrix} \tag{2.66}$$

or rewritten in simple form

$$\boldsymbol{f}_a = -\boldsymbol{D}_a\, \dot{\boldsymbol{q}}_W - \boldsymbol{C}_a\, \boldsymbol{q}_W + \boldsymbol{p}_a \quad . \tag{2.67}$$

2.5.3 Differential equations of translatory inertia

Differential equations of translatory inertia of a rotor which are considered in the fixed reference frame at the centre of gravitation of the system are

$$m\left(\ddot{z}_S\,\vec{e}_z + \ddot{y}_S\,\vec{e}_y\right) = \sum_n F_n \tag{2.68}$$

If the Equation (2.68) is separated into ζ and η-directions, thus

$$m\left(\ddot{\zeta}_s - \ddot{\varphi}\,\eta_s - 2\dot{\varphi}\,\dot{\eta}_s - \dot{\varphi}^2\,\zeta_s\right)\vec{e}_\zeta = \left(F_{a1} + F_{i1} + F_{c1} + F_g\right)\vec{e}_\zeta \tag{2.69}$$

$$m\left(\ddot{\eta}_s + \ddot{\varphi}\,\zeta_s + 2\dot{\varphi}\,\dot{\zeta}_s - \dot{\varphi}^2\,\eta_s\right)\vec{e}_\eta = \left(F_{a2} + F_{i2} + F_{c2} + F_g\right)\vec{e}_\eta \tag{2.70}$$

or in matrix notation the Equations (2.69) and (2.70) can be written as

$$\begin{bmatrix} m & & & \\ & m & & \\ & & 0 & \\ & & & 0 \end{bmatrix}\begin{bmatrix} \ddot{\zeta}_W \\ \ddot{\eta}_W \\ \ddot{\varphi}_\zeta \\ \ddot{\varphi}_\eta \end{bmatrix} + \begin{bmatrix} 0 & -2m\dot{\varphi} & 0 & 0 \\ 2m\dot{\varphi} & 0 & 0 & 0 \\ 0 & 0 & 0 & 0 \\ 0 & 0 & 0 & 0 \end{bmatrix}\begin{bmatrix} \dot{\zeta}_W \\ \dot{\eta}_W \\ \dot{\varphi}_\zeta \\ \dot{\varphi}_\eta \end{bmatrix}$$

$$+ \begin{bmatrix} -m\dot{\varphi}^2 & -m\ddot{\varphi} & 0 & 0 \\ m\ddot{\varphi} & -m\dot{\varphi}^2 & 0 & 0 \\ 0 & 0 & 0 & 0 \\ 0 & 0 & 0 & 0 \end{bmatrix}\begin{bmatrix} \zeta_W \\ \eta_W \\ \varphi_\zeta \\ \varphi_\eta \end{bmatrix} - \begin{bmatrix} m\varepsilon\ddot{\varphi}\sin\phi + m\varepsilon\dot{\varphi}^2\cos\phi \\ -m\varepsilon\ddot{\varphi}\cos\phi + m\varepsilon\dot{\varphi}^2\sin\phi \\ 0 \\ 0 \end{bmatrix} = \begin{bmatrix} \sum F\,\vec{e}_\zeta \\ \sum F\,\vec{e}_\eta \\ 0 \\ 0 \end{bmatrix} \tag{2.71}$$

or rewritten in simple form

$$\boldsymbol{M}_T\,\ddot{\boldsymbol{q}}_W + \boldsymbol{D}_T\,\dot{\boldsymbol{q}}_W + \boldsymbol{C}_T\,\boldsymbol{q}_W - \boldsymbol{p}_T = \boldsymbol{f}_T \quad . \tag{2.72}$$

2.5.4 Differential equations of rotary inertia

In rotating reference frame, the gyroscopic moments as presented in the Equation (2.23) should be used to obtain the complete differential equations of rotor motion in φ_ζ and φ_η-directions. Therefore, the differential equations of rotary inertia can be considered as follows

$$\dot{L}\,\vec{e}_\zeta = \left(M_{i3} + M_{c3}\right)\vec{e}_\zeta \tag{2.73}$$

$$\dot{L}\,\vec{e}_\eta = \left(M_{i4} + M_{c4}\right)\vec{e}_\eta \quad , \tag{2.74}$$

where the components M_{i3}, M_{i4}, M_{c3} and M_{c4} come from the Equations (2.54) and (2.62). In matrix notation the Equations (2.73) and (2.74) can be written as

$$
\begin{aligned}
&\begin{bmatrix} 0 & 0 & 0 & 0 \\ 0 & 0 & 0 & 0 \\ 0 & 0 & \Theta_a & 0 \\ 0 & 0 & 0 & \Theta_a \end{bmatrix}
\begin{bmatrix} \ddot{\zeta}_W \\ \ddot{\eta}_W \\ \ddot{\varphi}_\zeta \\ \ddot{\varphi}_\eta \end{bmatrix}
+
\begin{bmatrix} 0 & 0 & 0 & 0 \\ 0 & 0 & 0 & 0 \\ 0 & 0 & 0 & (\Theta_p - 2\Theta_a)\,\dot{\varphi} \\ 0 & 0 & -(\Theta_p - 2\Theta_a)\,\dot{\varphi} & 0 \end{bmatrix}
\begin{bmatrix} \dot{\zeta}_W \\ \dot{\eta}_W \\ \dot{\varphi}_\zeta \\ \dot{\varphi}_\eta \end{bmatrix} \\
&\qquad + \begin{bmatrix} 0 & 0 & 0 & 0 \\ 0 & 0 & 0 & 0 \\ 0 & 0 & (\Theta_p - \Theta_a)\,\dot{\varphi}^2 & (\Theta_p - \Theta_a)\,\ddot{\varphi} \\ 0 & 0 & -(\Theta_p - \Theta_a)\,\ddot{\varphi} & (\Theta_p - \Theta_a)\,\dot{\varphi}^2 \end{bmatrix}
\begin{bmatrix} \zeta_W \\ \eta_W \\ \varphi_\zeta \\ \varphi_\eta \end{bmatrix}
=
\begin{bmatrix} 0 \\ 0 \\ \sum M\,\vec{e}_\zeta \\ \sum M\,\vec{e}_\eta \end{bmatrix}
\end{aligned}
\tag{2.75}
$$

or rewritten in simple form

$$\boldsymbol{M}_G\,\ddot{\boldsymbol{q}}_W + \boldsymbol{D}_G\,\dot{\boldsymbol{q}}_W + \boldsymbol{C}_G\,\boldsymbol{q}_W = \boldsymbol{f}_G \quad . \tag{2.76}$$

2.5.5 Differential equations of rotor motion

Generally, the system has five differential equations of motion. The first four equations come from the following equation in matrices

$$
\begin{aligned}
&(\boldsymbol{M}_T + \boldsymbol{M}_G)\,\ddot{\boldsymbol{q}} + (\boldsymbol{D}_T + \boldsymbol{D}_G + \boldsymbol{D}_a + \boldsymbol{D}_i)\,\dot{\boldsymbol{q}} + (\boldsymbol{C}_T + \boldsymbol{C}_G + \boldsymbol{C}_a + \boldsymbol{C}_W)\,\boldsymbol{q} \\
&\qquad\qquad = \boldsymbol{p}_T + \boldsymbol{p}_a + \boldsymbol{p}_g
\end{aligned}
\tag{2.77}
$$

with the system matrices and force vectors from Equations (2.45), (2.55), (2.63), (2.67), (2.72) and (2.76).

Rewritten in simple form gives

$$\boldsymbol{M}\,\ddot{\boldsymbol{q}} + \boldsymbol{D}\,\dot{\boldsymbol{q}} + \boldsymbol{C}\,\boldsymbol{q} = \boldsymbol{p} \quad , \tag{2.78}$$

where each component matrix has the size 4×4. The matrix $\boldsymbol{M}$ is a diagonal matrix and has constant values. It is well known that the matrix $\boldsymbol{D}$ and the matrix $\boldsymbol{C}$ are speed-dependent and have skew-symmetric components.

Torsion due to reaction forces in bearings

Since the reaction forces in the bearings have been considered in the Equations (2.54) and (2.62), a torsion T_ε in the centre of gravitation S of the disk can be generated by the acting forces in the centre of the shaft W, hence

$$T_\varepsilon = -\varepsilon\,(\,\cos\phi\,\vec{e}_\zeta + \sin\phi\,\vec{e}_\eta\,) \times [(F_{i1} + F_{c1})\,\vec{e}_\zeta + (F_{i2} + F_{c2})\,\vec{e}_\eta] \quad . \tag{2.79}$$

Furthermore, because the reaction forces of bending shaft act not in the direction of shaft bending, a torque T_s will be brought forward from the shaft to the disk, thus

$$T_s = -\,(\eta_W\,\vec{e}_\eta + \zeta_W\,\vec{e}_\zeta) \times [(F_{i1} + F_{c1})\,\vec{e}_\zeta + (F_{i2} + F_{c2})\,\vec{e}_\eta] \quad . \tag{2.80}$$

If the driving torque of the shaft is defined as T_a then this torque, the T_ε and T_s are applied in the dynamic equation in the rotational x-direction as

$$-\Theta_p \ddot{\varphi}\, \vec{e}_x = -T_\varepsilon - T_s - T_a \quad , \tag{2.81}$$

hence, the fifth equation of motion of the rotor can be obtained. The complete set of the equations can be found in Appendix A.2.

2.6 Dynamic parameters of anisotropic rotor supported by anisotropic flexible bearings

In an anisotropic rotor supported by anisotropic flexible bearings, the system has eight degrees of freedom as shown in Figure 2.10. Four degrees of freedom come from a node, where a disk is attached and the others come from the motions of bearings.

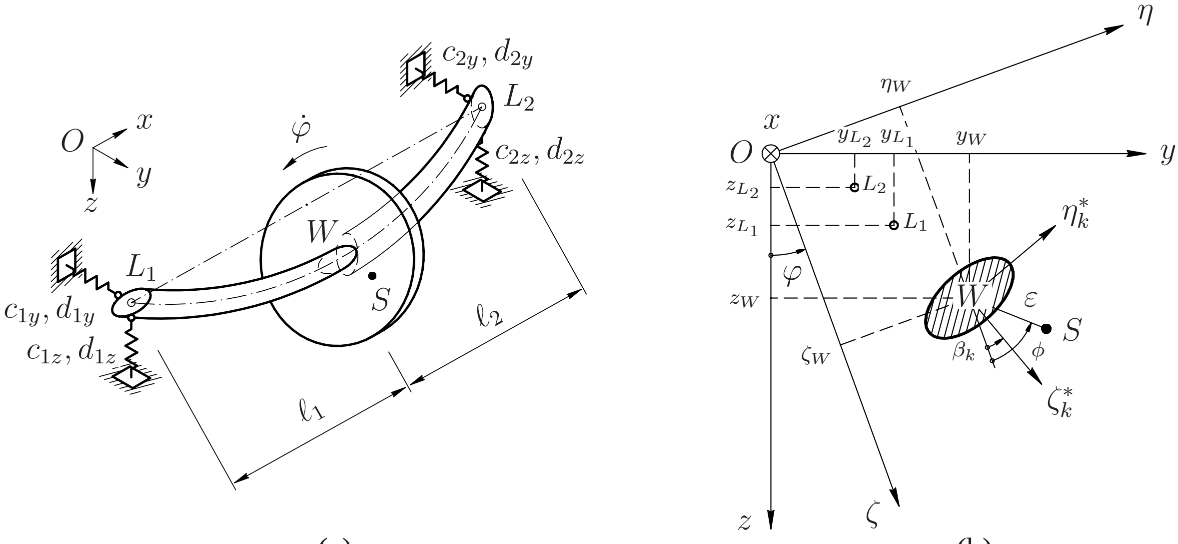

(a) (b)

Figure 2.9: Anisotropic rotor supported by anisotropic flexible bearings

Based on the Figure 2.10, the kinematic relationship in rotating reference frame can be determined. Therefore, the translational and rotational displacements of the bearings are obtained as follows

$$\zeta_L = \frac{\ell_2}{\ell}\,\zeta_{L_1} + \frac{\ell_1}{\ell}\,\zeta_{L_2} \qquad \text{and} \qquad \eta_L = \frac{\ell_2}{\ell}\,\eta_{L_1} + \frac{\ell_1}{\ell}\,\eta_{L_2} \tag{2.82}$$

and

$$\varphi_{\zeta L} \approx -\frac{1}{\ell}\left(\eta_{L_1} - \eta_{L_2}\right) \qquad \text{and} \qquad \varphi_{\eta L} \approx \frac{1}{\ell}\left(\zeta_{L_1} - \zeta_{L_2}\right) \quad . \tag{2.83}$$

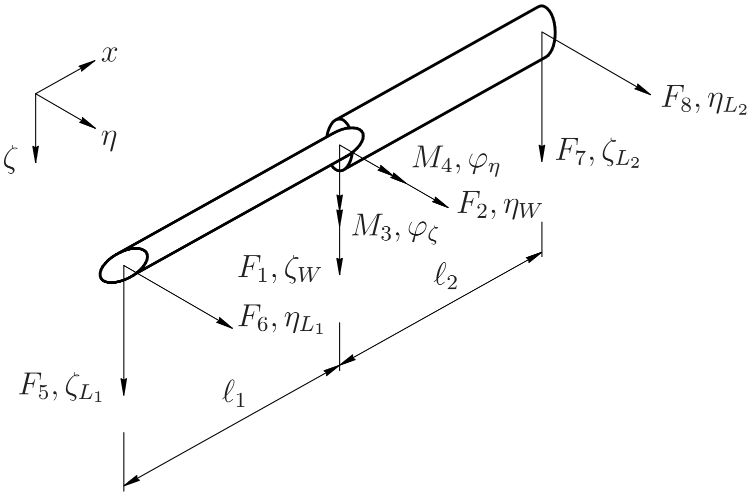

Figure 2.10: Rotor model 8-DoF with the minimal number of discrete elements

Furthermore, translational and rotational velocity of the bearings are obtained by derivation of the Equations (2.82) and (2.83) due to time respectively, hence

$$\dot{\zeta}_L = \frac{\ell_2}{\ell}\,\dot{\zeta}_{L_1} + \frac{\ell_1}{\ell}\,\dot{\zeta}_{L_2} \qquad \text{and} \qquad \dot{\eta}_L = \frac{\ell_2}{\ell}\,\dot{\eta}_{L_1} + \frac{\ell_1}{\ell}\,\dot{\eta}_{L_2} \tag{2.84}$$

and

$$\dot{\varphi}_{\zeta L} \approx -\frac{1}{\ell}\left(\dot{\eta}_{L_1} - \dot{\eta}_{L_2}\right) \qquad \text{and} \qquad \dot{\varphi}_{\eta L} \approx \frac{1}{\ell}\left(\dot{\zeta}_{L_1} - \dot{\zeta}_{L_2}\right) \quad . \tag{2.85}$$

2.6.1 Flexibility and damping matrices

Derivation of equations of the rotor supported by anisotropic flexible bearings is more complicated than the rotor supported by rigid bearings. The differential equations must be considered not only in the shaft system but also in the bearing system.

Equations in shaft system

Considering of the shaft stiffness in anisotropic flexible bearings is analoque to the shaft stiffness of the rotor supported by rigid bearings in Equation (2.53). The internal forces in the shaft are equal to the mutiplication of shaft stiffness and relative displacement of the disk, hence

$$\begin{bmatrix} F_{c1} \\ F_{c2} \\ M_{c3} \\ M_{c4} \end{bmatrix} = - \begin{bmatrix} c_{11} & c_{12} & c_{13} & c_{14} \\ c_{12} & c_{22} & c_{23} & c_{24} \\ c_{13} & c_{23} & c_{33} & c_{34} \\ c_{14} & c_{24} & c_{34} & c_{44} \end{bmatrix} \begin{bmatrix} \zeta_W - \zeta_L \\ \eta_W - \eta_L \\ \varphi_\zeta - \varphi_{\zeta L} \\ \varphi_\eta - \varphi_{\eta L} \end{bmatrix} \quad . \tag{2.86}$$

Using the Equations (2.82) and (2.83) give

$$\begin{bmatrix} F_{c1} \\ F_{c2} \\ M_{c3} \\ M_{c4} \end{bmatrix} = - \begin{bmatrix} c_{11} & c_{12} & c_{13} & c_{14} \\ c_{12} & c_{22} & c_{23} & c_{24} \\ c_{13} & c_{23} & c_{33} & c_{34} \\ c_{14} & c_{24} & c_{34} & c_{44} \end{bmatrix} \begin{bmatrix} \zeta_W \\ \eta_W \\ \varphi_\zeta \\ \varphi_\eta \end{bmatrix} + \begin{bmatrix} c_{15} & c_{16} & c_{17} & c_{18} \\ c_{25} & c_{26} & c_{27} & c_{28} \\ c_{35} & c_{36} & c_{37} & c_{38} \\ c_{45} & c_{46} & c_{47} & c_{48} \end{bmatrix} \begin{bmatrix} \zeta_{L_1} \\ \eta_{L_1} \\ \zeta_{L_2} \\ \eta_{L_2} \end{bmatrix} \tag{2.87}$$

or rewritten in simple form

$$\boldsymbol{f}_c = -\boldsymbol{C}_W \, \boldsymbol{q}_W + \boldsymbol{C}_{W_L} \, \boldsymbol{q}_L \quad , \tag{2.88}$$

where $\boldsymbol{C}_W$ is the shaft stiffness matrix of anisotropic rotor with different shaft orientations equivalent to Equation (2.53) and

$$\boldsymbol{C}_{W_L} = \begin{bmatrix} \left(\frac{\ell_2}{\ell} c_{11} + \frac{1}{\ell} c_{14}\right) & \left(\frac{\ell_2}{\ell} c_{12} - \frac{1}{\ell} c_{13}\right) & \left(\frac{\ell_1}{\ell} c_{11} - \frac{1}{\ell} c_{14}\right) & \left(\frac{\ell_1}{\ell} c_{12} + \frac{1}{\ell} c_{13}\right) \\ \left(\frac{\ell_2}{\ell} c_{12} + \frac{1}{\ell} c_{24}\right) & \left(\frac{\ell_2}{\ell} c_{22} - \frac{1}{\ell} c_{23}\right) & \left(\frac{\ell_1}{\ell} c_{12} - \frac{1}{\ell} c_{24}\right) & \left(\frac{\ell_1}{\ell} c_{22} + \frac{1}{\ell} c_{23}\right) \\ \left(\frac{\ell_2}{\ell} c_{13} + \frac{1}{\ell} c_{34}\right) & \left(\frac{\ell_2}{\ell} c_{23} - \frac{1}{\ell} c_{33}\right) & \left(\frac{\ell_1}{\ell} c_{13} - \frac{1}{\ell} c_{34}\right) & \left(\frac{\ell_1}{\ell} c_{23} + \frac{1}{\ell} c_{33}\right) \\ \left(\frac{\ell_2}{\ell} c_{14} + \frac{1}{\ell} c_{44}\right) & \left(\frac{\ell_2}{\ell} c_{24} - \frac{1}{\ell} c_{34}\right) & \left(\frac{\ell_1}{\ell} c_{14} - \frac{1}{\ell} c_{44}\right) & \left(\frac{\ell_1}{\ell} c_{24} + \frac{1}{\ell} c_{34}\right) \end{bmatrix} \quad . \tag{2.89}$$

Analoque to the above shaft stiffness, the internal damping forces can be determined

$$\begin{bmatrix} F_{i1} \\ F_{i2} \\ M_{i3} \\ M_{i4} \end{bmatrix} = - \begin{bmatrix} d_{11} & d_{12} & d_{13} & d_{14} \\ d_{12} & d_{22} & d_{23} & d_{24} \\ d_{13} & d_{23} & d_{33} & d_{34} \\ d_{14} & d_{24} & d_{34} & d_{44} \end{bmatrix} \begin{bmatrix} \dot{\zeta}_W - \dot{\zeta}_L \\ \dot{\eta}_W - \dot{\eta}_L \\ \dot{\varphi}_\zeta - \dot{\varphi}_{\zeta L} \\ \dot{\varphi}_\eta - \dot{\varphi}_{\eta L} \end{bmatrix} \quad . \tag{2.90}$$

Using the Equations (2.84) and (2.85) give

$$\begin{bmatrix} F_{i1} \\ F_{i2} \\ M_{i3} \\ M_{i4} \end{bmatrix} = - \begin{bmatrix} d_{11} & d_{12} & d_{13} & d_{14} \\ d_{12} & d_{22} & d_{23} & d_{24} \\ d_{13} & d_{23} & d_{33} & d_{34} \\ d_{14} & d_{24} & d_{34} & d_{44} \end{bmatrix} \begin{bmatrix} \dot{\zeta}_W \\ \dot{\eta}_W \\ \dot{\varphi}_\zeta \\ \dot{\varphi}_\eta \end{bmatrix} + \begin{bmatrix} d_{15} & d_{16} & d_{17} & d_{18} \\ d_{25} & d_{26} & d_{27} & d_{28} \\ d_{35} & d_{36} & d_{37} & d_{38} \\ d_{45} & d_{46} & d_{47} & d_{48} \end{bmatrix} \begin{bmatrix} \dot{\zeta}_{L_1} \\ \dot{\eta}_{L_1} \\ \dot{\zeta}_{L_2} \\ \dot{\eta}_{L_2} \end{bmatrix} \tag{2.91}$$

or rewritten in simple form

$$\boldsymbol{f}_i = -\boldsymbol{D}_i \, \dot{\boldsymbol{q}}_W + \boldsymbol{D}_{i_L} \, \dot{\boldsymbol{q}}_L \quad , \tag{2.92}$$

where $\boldsymbol{D}_i$ is the internal damping matrix of the shaft or equivalent to Equation (2.63) and

$$\boldsymbol{D}_{i_L} = \begin{bmatrix} \left(\frac{\ell_2}{\ell} d_{11} + \frac{1}{\ell} d_{14}\right) & \left(\frac{\ell_2}{\ell} d_{12} - \frac{1}{\ell} d_{13}\right) & \left(\frac{\ell_1}{\ell} d_{11} - \frac{1}{\ell} d_{14}\right) & \left(\frac{\ell_1}{\ell} d_{12} + \frac{1}{\ell} d_{13}\right) \\ \left(\frac{\ell_2}{\ell} d_{12} + \frac{1}{\ell} d_{24}\right) & \left(\frac{\ell_2}{\ell} d_{22} - \frac{1}{\ell} d_{23}\right) & \left(\frac{\ell_1}{\ell} d_{12} - \frac{1}{\ell} d_{24}\right) & \left(\frac{\ell_1}{\ell} d_{22} + \frac{1}{\ell} d_{23}\right) \\ \left(\frac{\ell_2}{\ell} d_{13} + \frac{1}{\ell} d_{34}\right) & \left(\frac{\ell_2}{\ell} d_{23} - \frac{1}{\ell} d_{33}\right) & \left(\frac{\ell_1}{\ell} d_{13} - \frac{1}{\ell} d_{34}\right) & \left(\frac{\ell_1}{\ell} d_{23} + \frac{1}{\ell} d_{33}\right) \\ \left(\frac{\ell_2}{\ell} d_{14} + \frac{1}{\ell} d_{44}\right) & \left(\frac{\ell_2}{\ell} d_{24} - \frac{1}{\ell} d_{34}\right) & \left(\frac{\ell_1}{\ell} d_{14} - \frac{1}{\ell} d_{44}\right) & \left(\frac{\ell_1}{\ell} d_{24} + \frac{1}{\ell} d_{34}\right) \end{bmatrix} \quad . \tag{2.93}$$

Because the external damping forces are formulated by proportional damping corresponding to the absolute velocity of the disk, there is no difference of formulation of the Equation (2.67) for anisotropic rotor supported by anisotropic flexible bearings.

Furthermore, the reaction forces in the bearings can be determined. The reaction force for supporting the left side of the rotor in ζ-direction is

$$F_5 = -\left[\frac{\ell_2}{\ell}\left(F_{c1} + F_{i1}\right) + \frac{1}{\ell}\left(M_{c4} + M_{i4}\right)\right] \tag{2.94}$$

and in η-direction

$$F_6 = -\left[\frac{\ell_2}{\ell}\left(F_{c2} + F_{i2}\right) - \frac{1}{\ell}\left(M_{c3} + M_{i3}\right)\right] \quad . \tag{2.95}$$

The reaction force for supporting the right side of the rotor in ζ-direction is

$$F_7 = -\left[\frac{\ell_1}{\ell}\left(F_{c1} + F_{i1}\right) - \frac{1}{\ell}\left(M_{c4} + M_{i4}\right)\right] \tag{2.96}$$

and in η-direction

$$F_8 = -\left[\frac{\ell_1}{\ell}\left(F_{c2} + F_{i2}\right) + \frac{1}{\ell}\left(M_{c3} + M_{i3}\right)\right] \quad . \tag{2.97}$$

If a force vector is introduced

$$\boldsymbol{f}_{L_W} = \Big(F_5, F_6, F_7, F_8\Big)^T \tag{2.98}$$

or in simple form of matrix notation

$$\boldsymbol{f}_{L_W} = \boldsymbol{D}_{i_L}^T\, \dot{\boldsymbol{q}}_W - \boldsymbol{D}_{L_L}\, \dot{\boldsymbol{q}}_L + \boldsymbol{C}_{W_L}^T\, \boldsymbol{q}_W - \boldsymbol{C}_{L_L}\, \boldsymbol{q}_L \quad , \tag{2.99}$$

where

$$\boldsymbol{D}_{L_L} = \begin{bmatrix} \left(\frac{\ell_2}{\ell}d_{15} + \frac{1}{\ell}d_{45}\right) & \left(\frac{\ell_2}{\ell}d_{16} + \frac{1}{\ell}d_{46}\right) & \left(\frac{\ell_2}{\ell}d_{17} + \frac{1}{\ell}d_{47}\right) & \left(\frac{\ell_2}{\ell}d_{18} + \frac{1}{\ell}d_{48}\right) \\ \left(\frac{\ell_2}{\ell}d_{25} - \frac{1}{\ell}d_{35}\right) & \left(\frac{\ell_2}{\ell}d_{26} - \frac{1}{\ell}d_{36}\right) & \left(\frac{\ell_2}{\ell}d_{27} - \frac{1}{\ell}d_{37}\right) & \left(\frac{\ell_2}{\ell}d_{28} - \frac{1}{\ell}d_{38}\right) \\ \left(\frac{\ell_1}{\ell}d_{15} - \frac{1}{\ell}d_{45}\right) & \left(\frac{\ell_1}{\ell}d_{16} - \frac{1}{\ell}d_{46}\right) & \left(\frac{\ell_1}{\ell}d_{17} - \frac{1}{\ell}d_{47}\right) & \left(\frac{\ell_1}{\ell}d_{18} - \frac{1}{\ell}d_{48}\right) \\ \left(\frac{\ell_1}{\ell}d_{25} + \frac{1}{\ell}d_{35}\right) & \left(\frac{\ell_1}{\ell}d_{26} + \frac{1}{\ell}d_{36}\right) & \left(\frac{\ell_1}{\ell}d_{27} + \frac{1}{\ell}d_{37}\right) & \left(\frac{\ell_1}{\ell}d_{28} + \frac{1}{\ell}d_{38}\right) \end{bmatrix} \tag{2.100}$$

and

$$\boldsymbol{C}_{L_L} = \begin{bmatrix} \left(\frac{\ell_2}{\ell}c_{15} + \frac{1}{\ell}c_{45}\right) & \left(\frac{\ell_2}{\ell}c_{16} + \frac{1}{\ell}c_{46}\right) & \left(\frac{\ell_2}{\ell}c_{17} + \frac{1}{\ell}c_{47}\right) & \left(\frac{\ell_2}{\ell}c_{18} + \frac{1}{\ell}c_{48}\right) \\ \left(\frac{\ell_2}{\ell}c_{25} - \frac{1}{\ell}c_{35}\right) & \left(\frac{\ell_2}{\ell}c_{26} - \frac{1}{\ell}c_{36}\right) & \left(\frac{\ell_2}{\ell}c_{27} - \frac{1}{\ell}c_{37}\right) & \left(\frac{\ell_2}{\ell}c_{28} - \frac{1}{\ell}c_{38}\right) \\ \left(\frac{\ell_1}{\ell}c_{15} - \frac{1}{\ell}c_{45}\right) & \left(\frac{\ell_1}{\ell}c_{16} - \frac{1}{\ell}c_{46}\right) & \left(\frac{\ell_1}{\ell}c_{17} - \frac{1}{\ell}c_{47}\right) & \left(\frac{\ell_1}{\ell}c_{18} - \frac{1}{\ell}c_{48}\right) \\ \left(\frac{\ell_1}{\ell}c_{25} + \frac{1}{\ell}c_{35}\right) & \left(\frac{\ell_1}{\ell}c_{26} + \frac{1}{\ell}c_{36}\right) & \left(\frac{\ell_1}{\ell}c_{27} + \frac{1}{\ell}c_{37}\right) & \left(\frac{\ell_1}{\ell}c_{28} + \frac{1}{\ell}c_{38}\right) \end{bmatrix} \quad . \tag{2.101}$$

Equations in bearing system

The force on the left bearing is

$$F_{L_1} = -\left[\left(d_{1z}\,\dot{z}_{L_1} + c_{1z}\,z_{L_1}\right)\vec{e}_z + \left(d_{1y}\,\dot{y}_{L_1} + c_{1y}\,y_{L_1}\right)\vec{e}_y\right] \tag{2.102}$$

and for the right bearing

$$F_{L_2} = -\left[\left(d_{2z}\,\dot{z}_{L_2} + c_{2z}\,z_{L_2}\right)\vec{e}_z + \left(d_{2y}\,\dot{y}_{L_2} + c_{2y}\,y_{L_2}\right)\vec{e}_y\right] \quad , \tag{2.103}$$

where all forces are performed in fixed reference frame, whereas the shaft stiffness is performed in rotating reference frame. Therefore, the equations in the bearings should be transformed into rotating reference frame of by using the Equation (2.4), hence the equations of the reaction damping forces in the bearings are obtained

$$\begin{bmatrix} F_{d_{1\zeta}} \\ F_{d_{1\eta}} \\ F_{d_{2\zeta}} \\ F_{d_{2\eta}} \end{bmatrix} = -\begin{bmatrix} d_{p_1}+d^{(c)}_{k_1} & -d^{(s)}_{k_1} & 0 & 0 \\ -d^{(s)}_{k_1} & d_{p_1}-d^{(c)}_{k_1} & 0 & 0 \\ 0 & 0 & d_{p_2}+d^{(c)}_{k_2} & -d^{(s)}_{k_2} \\ 0 & 0 & -d^{(s)}_{k_2} & d_{p_2}-d^{(c)}_{k_2} \end{bmatrix} \begin{bmatrix} \dot\zeta_{L_1} \\ \dot\eta_{L_1} \\ \dot\zeta_{L_2} \\ \dot\eta_{L_2} \end{bmatrix}$$
$$-\begin{bmatrix} -d^{(s)}_{k_1}\dot\varphi & -d_{p_1}\dot\varphi-d^{(c)}_{k_1}\dot\varphi & 0 & 0 \\ d_{p_1}\dot\varphi-d^{(c)}_{k_1}\dot\varphi & d^{(s)}_{k_1}\dot\varphi & 0 & 0 \\ 0 & 0 & -d^{(s)}_{k_2}\dot\varphi & -d_{p_2}\dot\varphi-d^{(c)}_{k_2}\dot\varphi \\ 0 & 0 & d_{p_2}\dot\varphi-d^{(c)}_{k_2}\dot\varphi & d^{(s)}_{k_2}\dot\varphi \end{bmatrix} \begin{bmatrix} \zeta_{L_1} \\ \eta_{L_1} \\ \zeta_{L_2} \\ \eta_{L_2} \end{bmatrix} \tag{2.104}$$

where

$$\begin{aligned} d_{p_1} &= \tfrac{1}{2}\left(d_{1z}+d_{1y}\right) & d_{p_2} &= \tfrac{1}{2}\left(d_{2z}+d_{2y}\right) \\ d^{(c)}_{k_1} &= \tfrac{1}{2}\left(d_{1z}-d_{1y}\right)\cos 2\varphi & d^{(c)}_{k_2} &= \tfrac{1}{2}\left(d_{2z}-d_{2y}\right)\cos 2\varphi \\ d^{(s)}_{k_1} &= \tfrac{1}{2}\left(d_{1z}-d_{1y}\right)\sin 2\varphi & d^{(s)}_{k_2} &= \tfrac{1}{2}\left(d_{2z}-d_{2y}\right)\sin 2\varphi \quad . \end{aligned} \tag{2.105}$$

In a simple form, the Equation (2.104) can be written as

$$\boldsymbol{f}_{d_L} = -\boldsymbol{D}_{d_L}\,\dot{\boldsymbol{q}}_L - \boldsymbol{C}_{d_L}\,\boldsymbol{q}_L \quad . \tag{2.106}$$

Furthermore, the equations of the reaction deflection forces in the bearings are

$$\begin{bmatrix} F_{c_{1\zeta}} \\ F_{c_{1\eta}} \\ F_{c_{2\zeta}} \\ F_{c_{2\eta}} \end{bmatrix} = -\begin{bmatrix} c_{p_1}+c^{(c)}_{k_1} & -c^{(s)}_{k_1} & 0 & 0 \\ -c^{(s)}_{k_1} & c_{p_1}-c^{(c)}_{k_1} & 0 & 0 \\ 0 & 0 & c_{p_2}+c^{(c)}_{k_2} & -c^{(s)}_{k_2} \\ 0 & 0 & -c^{(s)}_{k_2} & c_{p_2}-c^{(c)}_{k_2} \end{bmatrix} \begin{bmatrix} \zeta_{L_1} \\ \eta_{L_1} \\ \zeta_{L_2} \\ \eta_{L_2} \end{bmatrix} \quad , \tag{2.107}$$

where

$$\begin{aligned} c_{p_1} &= \tfrac{1}{2}\left(c_{1z}+c_{1y}\right) & c_{p_2} &= \tfrac{1}{2}\left(c_{2z}+c_{2y}\right) \\ c^{(c)}_{k_1} &= \tfrac{1}{2}\left(c_{1z}-c_{1y}\right)\cos 2\varphi & c^{(c)}_{k_2} &= \tfrac{1}{2}\left(c_{2z}-c_{2y}\right)\cos 2\varphi \\ c^{(s)}_{k_1} &= \tfrac{1}{2}\left(c_{1z}-c_{1y}\right)\sin 2\varphi & c^{(s)}_{k_2} &= \tfrac{1}{2}\left(c_{2z}-c_{2y}\right)\sin 2\varphi \quad . \end{aligned} \tag{2.108}$$

In a simple form, the Equation (2.107) can be written as

$$\boldsymbol{f}_{c_L} = -\boldsymbol{C}_L\,\boldsymbol{q}_L \tag{2.109}$$

Now, the equations in the bearing system can be determined to

$$\boldsymbol{M}_L\,\ddot{\boldsymbol{q}}_L = \boldsymbol{f}_{L_W} + \boldsymbol{f}_{d_L} + \boldsymbol{f}_{c_L} \tag{2.110}$$

2.6.2 Differential equations of rotor motion

Similar to Section 2.5.5, in general the anisotropic rotor supported by anisotropic flexible bearings has nine differential equations. With the assumption that the bearing mass coefficient in matrix $\boldsymbol{M}_L$ is zero, hence the first eight equations of motion of the rotor can be written as

$$\left[\begin{array}{c|c} \boldsymbol{M}_T + \boldsymbol{M}_G & \boldsymbol{0} \\ \hline \boldsymbol{0} & \boldsymbol{M}_L \end{array}\right] \begin{bmatrix} \ddot{\boldsymbol{q}}_W \\ \ddot{\boldsymbol{q}}_L \end{bmatrix} + \left[\begin{array}{c|c} \boldsymbol{D}_T + \boldsymbol{D}_G + \boldsymbol{D}_a + \boldsymbol{D}_i & -\boldsymbol{D}_{i_L} \\ \hline -\boldsymbol{D}_{i_L}^T & \boldsymbol{D}_{L_L} + \boldsymbol{D}_{d_L} \end{array}\right] \begin{bmatrix} \dot{\boldsymbol{q}}_W \\ \dot{\boldsymbol{q}}_L \end{bmatrix}$$

$$+ \left[\begin{array}{c|c} \boldsymbol{C}_T + \boldsymbol{C}_G + \boldsymbol{C}_a + \boldsymbol{C}_W & -\boldsymbol{C}_{W_L} \\ \hline -\boldsymbol{C}_{W_L}^T & \boldsymbol{C}_{L_L} + \boldsymbol{C}_{d_L} + \boldsymbol{C}_L \end{array}\right] \begin{bmatrix} \boldsymbol{q}_W \\ \boldsymbol{q}_L \end{bmatrix} = \begin{bmatrix} \boldsymbol{p}_T + \boldsymbol{p}_a + \boldsymbol{p}_g \\ \boldsymbol{0} \end{bmatrix} . \tag{2.111}$$

In general form the Equation (2.111) can be written as

$$\boldsymbol{M}\,\ddot{\boldsymbol{q}} + \boldsymbol{D}\,\dot{\boldsymbol{q}} + \boldsymbol{C}\,\boldsymbol{q} = \boldsymbol{p} \tag{2.112}$$

Torsion due to reaction forces in bearings

Similar to the case of the rotor supported by rigid bearings as mentioned in Section 2.5, the torsion T_ε in the centre of gravitation S of the disk can be generated by the acting forces in the centre of the shaft W as

$$T_\varepsilon = -\varepsilon\,(\,\cos\phi\,\vec{e}_\zeta + \sin\phi\,\vec{e}_\eta\,) \times [(F_{i1} + F_{c1})\,\vec{e}_\zeta + (F_{i2} + F_{c2})\,\vec{e}_\eta] \quad . \tag{2.113}$$

Furthermore, because the reaction forces of bending shaft act not in the direction of shaft bending, a torque T_s will be brought forward from the shaft to the disk, thus

$$T_s = -\,[(\eta_W - \eta_L)\,\vec{e}_\eta + (\zeta_W - \zeta_L)\,\vec{e}_\zeta] \times [(F_{i1} + F_{c1})\,\vec{e}_\zeta + (F_{i2} + F_{c2})\,\vec{e}_\eta] \quad . \tag{2.114}$$

If T_ε, T_s and the driving torque T_a are applied in the dynamic equation in the rotational x-direction, thus

$$-\Theta_p \ddot{\varphi}\,\vec{e}_x = -T_\varepsilon - T_s - T_a \quad . \tag{2.115}$$

Now, the ninth equation of motion of the rotor is obtained. The complete set of the equations can be found in Appendix-B2.

2.7 Anisotropic shaft with single disk and many shaft elements

Modelling of a single disk anisotropic shaft discretized by many discrete shaft elements is explained in more detail in Section 3, where a general of multiple disks anisotropic rotor with many shaft elements will be discussed. If a rotor shaft is descretized into N_e-elements and a node is defined as a joint between two elements then the rotor model will have $N_d = N_e - 1$ nodes. A disk can be attached only in a node. Therefore, the system has a matrix $4N_d \times 4N_d$. Whereas the rotor with only one disk has many dummy disks assumed to be massless, hence the mass matrix has only four components which are not zero in diagonal of the matrix . Therefore, the mass matrix is singular. In the shaft stiffness matrix, there is no particular condition, where the matrix size is extended up to $4N_d \times 4N_d$. Arranging the general equations of motion of the rotor based on rotating reference frame, the matrix ***C*** consists of components of a shaft stiffness matrix, components of proportional mass and proportional damping coefficients due to displacement. The matrix ***D*** consists of internal and external damping matrices, gyroscopic matrix and components of proportional mass due to velocity. Because the internal damping is considered by using an approach of proporsional damping due to mass matrix and stiffness matrix as written in the Equation (2.56), the size of damping matrix is also $4N_d \times 4N_d$.

In order to solve the differential equations numerically, there is a problem if the mass matrix is singular. Because of that, the static condensation method (see Section 2.8) can be used, where the zero part in the diagonal of mass matrix can be eliminated. Now, the reduced matrix has the size 4×4 only. The matrices ***D*** and ***C*** are reduced accordingly.

2.8 Reduction of degrees of freedom (static condensation)

Several methods have been developed to reduce the number of degrees of freedom of a system, those are static condensation, dynamic condensation, modal condensation and a modified static and modal condensation [10]. For some zero components in diagonal mass matrix, as mentioned in the previous section, the method of static condensation is very covenient to be used.

With the assumption that the part of $\boldsymbol{D}_{i_L}^T$ and $(\boldsymbol{D}_{L_L} + \boldsymbol{D}_{d_L})$ are negligible, the Equation (2.111) becomes

$$\left[\begin{array}{c|c} \boldsymbol{M}_T + \boldsymbol{M}_G & 0 \\ \hline 0 & 0 \end{array}\right]\begin{bmatrix} \ddot{\boldsymbol{q}}_W \\ \ddot{\boldsymbol{q}}_L \end{bmatrix} + \left[\begin{array}{c|c} \boldsymbol{D}_T + \boldsymbol{D}_G + \boldsymbol{D}_a + \boldsymbol{D}_i & -\boldsymbol{D}_{i_L} \\ \hline 0 & 0 \end{array}\right]\begin{bmatrix} \dot{\boldsymbol{q}}_W \\ \dot{\boldsymbol{q}}_L \end{bmatrix}$$
$$+ \left[\begin{array}{c|c} \boldsymbol{C}_T + \boldsymbol{C}_G + \boldsymbol{C}_a + \boldsymbol{C}_W & -\boldsymbol{C}_{W_L} \\ \hline -\boldsymbol{C}_{W_L}^T & \boldsymbol{C}_{L_L} + \boldsymbol{C}_{d_L} + \boldsymbol{C}_L \end{array}\right]\begin{bmatrix} \boldsymbol{q}_W \\ \boldsymbol{q}_L \end{bmatrix} = \begin{bmatrix} \boldsymbol{p}_T + \boldsymbol{p}_a + \boldsymbol{p}_g \\ 0 \end{bmatrix} . \quad (2.116)$$

Equation (2.116) can be written in short form as

$$\begin{bmatrix} \boldsymbol{M}_{11} & 0 \\ 0 & 0 \end{bmatrix}\begin{bmatrix} \ddot{\boldsymbol{q}}_W \\ \ddot{\boldsymbol{q}}_L \end{bmatrix} + \begin{bmatrix} \boldsymbol{D}_{11} & \boldsymbol{D}_{12} \\ 0 & 0 \end{bmatrix}\begin{bmatrix} \dot{\boldsymbol{q}}_W \\ \dot{\boldsymbol{q}}_L \end{bmatrix} + \begin{bmatrix} \boldsymbol{C}_{11} & \boldsymbol{C}_{12} \\ \boldsymbol{C}_{21} & \boldsymbol{C}_{22} \end{bmatrix}\begin{bmatrix} \boldsymbol{q}_W \\ \boldsymbol{q}_L \end{bmatrix} = \begin{bmatrix} \boldsymbol{p}_1 \\ 0 \end{bmatrix} . \quad (2.117)$$

The second line of those matrices yields

$$\boldsymbol{q}_L = -\boldsymbol{C}_{22}^{-1}\,\boldsymbol{C}_{21}\,\boldsymbol{q}_W \quad . \quad (2.118)$$

Removing the Equation (2.117) gives

$$\boldsymbol{M}_{11}\,\ddot{\boldsymbol{q}}_W + \bar{\boldsymbol{D}}_{11}\,\dot{\boldsymbol{q}}_W + \bar{\boldsymbol{C}}_{11},\dot{\boldsymbol{q}}_W = \boldsymbol{p}_1 \quad , \tag{2.119}$$

where

$$\bar{\boldsymbol{D}}_{11} = \boldsymbol{D}_{11} - \boldsymbol{D}_{12}\boldsymbol{C}_{22}^{-1}\boldsymbol{C}_{21} \qquad \text{and} \qquad \bar{\boldsymbol{C}}_{11} = \boldsymbol{C}_{11} - \boldsymbol{C}_{12}\boldsymbol{C}_{22}^{-1}\boldsymbol{C}_{21} \tag{2.120}$$

Note that, if the sub matrix $\boldsymbol{C}_{22}$ is time-variant, the sub matrix $\bar{\boldsymbol{C}}_{11}$ becomes time-variant too. This must be a point of attention in numerical calculation. It will be discussed in Section (2.9.2).

2.9 Stability analysis of rotor system

Stability analysis of a rotor is an essential point in dynamic analysis of the rotor. Here, the stability of the solution of the homogenous linear equations of rotor motion will be conducted. In the previous section, it has been mentioned that in the stationary case of an anisotropic rotor supported by rigid bearings, the system matrices can be speed-dependent or time-dependent depending on the reference frame of the system. In case of an anisotropic rotor supported by anisotropic flexible bearings, a time-variant system is obtained independently of whether the rotor model is analyzed in fixed or rotating reference frame. If the system matrices are speed-dependent, the stability investigation can be performed by analyzing the eigenvalues at specific angular speeds directly. As discussed in [25], the eigenvalues can be conjugate complex or real and characterize the natural vibration. The imaginary part corresponds to the natural frequency and the real part gives the stability of the natural vibration. The vibration decays with time if the real part is negative and grows if the real part is positive.

In case of a time-variant system, some methods have been developed to solve this problem of which the FLOQUET theory and HILL's method are two that are widely used. However, in references [3], [47], [48], [52] the researchers encountered problems with computational time especially when using FLOQUET theory. In this section, the FLOQUET theory will be discussed theoretically. Because of the very fast development in computer technology, especially in the processor speed and memory capacity, the problem of computational time is reduced straightforwardly. In order to determine the stability, a direct investigation is proposed by means of a spectral map of the dynamic responses.

2.9.1 Stability analysis of speed-dependent system

As formulated in [9], the stability of the rotor system is considered based on the homogenous linear equations of motion of the rotor

$$\boldsymbol{M}\,\ddot{\boldsymbol{q}} + \boldsymbol{D}\,\dot{\boldsymbol{q}} + \boldsymbol{C}\,\boldsymbol{q} = \boldsymbol{0} \quad . \tag{2.121}$$

Therefore, the eigenvalue problem by using the characterictic determinant can be solved

$$\det\left(\lambda^2\boldsymbol{M}+\lambda\boldsymbol{D}+\boldsymbol{C}\right)=0 \tag{2.122}$$

The Equations (2.122) can be rearranged in state-space in order to reduce the differential equations to first-order

$$\begin{bmatrix}\boldsymbol{D} & \boldsymbol{C}\\ \boldsymbol{C} & \boldsymbol{0}\end{bmatrix}\begin{bmatrix}\dot{\boldsymbol{q}}\\ \boldsymbol{q}\end{bmatrix}-\begin{bmatrix}-\boldsymbol{M} & \boldsymbol{0}\\ \boldsymbol{0} & \boldsymbol{C}\end{bmatrix}\begin{bmatrix}\ddot{\boldsymbol{q}}\\ \dot{\boldsymbol{q}}\end{bmatrix}=\begin{bmatrix}\boldsymbol{0}\\ \boldsymbol{0}\end{bmatrix} \tag{2.123}$$

For simplification in writting, the Equation (2.123) can be written as

$$\boldsymbol{A}\,\boldsymbol{r}-\boldsymbol{B}\,\dot{\boldsymbol{r}}=\boldsymbol{0} \tag{2.124}$$

or

$$\left(\boldsymbol{A}-\lambda\boldsymbol{B}\right)\boldsymbol{r}=\boldsymbol{0} \quad . \tag{2.125}$$

By solving Equation (2.125), the eigenvalues and eigenvectors of the system can be calculated. Usually, the eigenvectors are denoted by matrix $\boldsymbol{R}$ of right eigenvectors, where

$$\boldsymbol{R}=\left(\boldsymbol{r}_1,\boldsymbol{r}_2,\ldots,\boldsymbol{r}_{2N}\right) \quad . \tag{2.126}$$

Furthermore, because of non-symmetrical matrices $\boldsymbol{A}$ and $\boldsymbol{B}$, transposing Equation (2.123) gives

$$\left(\boldsymbol{A}^T-\chi\boldsymbol{B}^T\right)\boldsymbol{l}=\boldsymbol{0} \quad . \tag{2.127}$$

The eigenvalues and eigenvectors can be considered, where the eigenvectors are denoted by matrix $\boldsymbol{L}$ of left eigenvectors

$$\boldsymbol{L}=\left(\boldsymbol{l}_1,\boldsymbol{l}_2,\ldots,\boldsymbol{l}_{2N}\right) \quad . \tag{2.128}$$

The eigenvalues of Equation (2.125) and (2.127) must be identical, where $\lambda_i=\chi_i$. However, both matrices of eigenvectors are not equal.

Let the modal vectors be specified as

$$\boldsymbol{r}=\boldsymbol{R}\,\tilde{\boldsymbol{r}} \quad . \tag{2.129}$$

By inserting Equation (2.129) into (2.125), then a premultiplication by transpose of the left eigenvectors, the uncoupled modal transformation of differential equations in (2.123) is obtained

$$\boldsymbol{L}^T\boldsymbol{A}\boldsymbol{R}\,\tilde{\boldsymbol{r}}-\boldsymbol{L}^T\boldsymbol{B}\boldsymbol{R}\,\dot{\tilde{\boldsymbol{r}}}=\boldsymbol{0} \quad , \tag{2.130}$$

where

$$\boldsymbol{L}^T\boldsymbol{A}\boldsymbol{R}=\text{diag}\left(\boldsymbol{a}_i\right) \qquad \text{where} \qquad i=1,...,2N \tag{2.131}$$

and

$$\boldsymbol{L}^T\boldsymbol{B}\boldsymbol{R}=\text{diag}\left(\boldsymbol{b}_i\right) \qquad \text{where} \qquad i=1,...,2N \tag{2.132}$$

In stability analysis, the solution of eigenvalues according to Equation (2.125) is already sufficient. Usually, the eigenvalues are complex frequencies consisting of a real part (i.e. defined as decay rate, where it decreases amplitude in time) and an imaginary part (i.e. natural frequencies). An instability condition is involved if at least one of the real parts of the eigenvalues is positive value. The imaginary parts of eigenvalues are speed-dependent and can be plotted in dependence of the rotor speed. The plots of the imaginary parts of eigenvalues against the rotational speed of the rotor is called generally as CAMPBELL diagram [12].

2.9.2 Stability analysis of time-variant system

As derived in Equation (2.112), the equations of motion of the rotor system supported by anisotropic flexible bearings are time-variant matrices. While the mass matrix is constant, the damping and stiffness matrices are periodic in time,

$$\boldsymbol{D}(t) = \boldsymbol{D}(t+T) \qquad \text{and} \qquad \boldsymbol{C}(t) = \boldsymbol{C}(t+T) \tag{2.133}$$

where T is the period.

Stability investigation according to FLOQUET theory

Following [10], the FLOQUET theory is explained in some detail. The analysis is based on the homogenous linear equations of motion of the rotor in Equation (2.112) and can be written as

$$\boldsymbol{M}\,\ddot{\boldsymbol{q}} + \boldsymbol{D}\,\dot{\boldsymbol{q}} + \boldsymbol{C}\,\boldsymbol{q} = \boldsymbol{0} \quad . \tag{2.134}$$

By using the state-vector $\boldsymbol{r} = (\dot{\boldsymbol{q}}\ \ \boldsymbol{q})^T$, the Equation (2.134) can be regarded as the components of 2N-dimensional given by

$$\begin{bmatrix} \boldsymbol{D} & \boldsymbol{C} \\ \boldsymbol{I} & \boldsymbol{0} \end{bmatrix} \begin{bmatrix} \dot{\boldsymbol{q}} \\ \boldsymbol{q} \end{bmatrix} - \begin{bmatrix} -\boldsymbol{M} & \boldsymbol{0} \\ \boldsymbol{0} & \boldsymbol{I} \end{bmatrix} \begin{bmatrix} \ddot{\boldsymbol{q}} \\ \dot{\boldsymbol{q}} \end{bmatrix} = \begin{bmatrix} \boldsymbol{0} \\ \boldsymbol{0} \end{bmatrix} \tag{2.135}$$

or

$$\begin{bmatrix} \ddot{\boldsymbol{q}} \\ \dot{\boldsymbol{q}} \end{bmatrix} = \begin{bmatrix} -\boldsymbol{M}^{-1}\boldsymbol{D} & -\boldsymbol{M}^{-1}\boldsymbol{C} \\ \boldsymbol{I} & \boldsymbol{0} \end{bmatrix} \begin{bmatrix} \dot{\boldsymbol{q}} \\ \boldsymbol{q} \end{bmatrix} \tag{2.136}$$

and rewritten in simple form

$$\dot{\boldsymbol{r}} = \boldsymbol{A}\,\boldsymbol{r} \quad , \tag{2.137}$$

where the matrix $\boldsymbol{A}$ is the state-space matrix periodic with period T.

By introducing initial conditions $\boldsymbol{q}(0) = \boldsymbol{q}_0$ and $\dot{\boldsymbol{q}}(0) = \dot{\boldsymbol{q}}_0$ and fundamental matrix $\boldsymbol{\Psi}(t)$, the Equation (2.137) is solved as homogenous solution of linear differential equations by using numerical integration from $t = 0$ to $t = T$. By taking the values after one period T of these homogenous solutions, the fundamental matrix $\boldsymbol{\Psi}(T)$ can be obtained. If $\boldsymbol{\Psi}(T)$ is denoted as transfer matrix after one period T, thus

$$\begin{bmatrix} \dot{\boldsymbol{q}} \\ \boldsymbol{q} \end{bmatrix}_{t=T} = \Big[\boldsymbol{\Psi}(T)\Big] \begin{bmatrix} \dot{\boldsymbol{q}}_0 \\ \boldsymbol{q}_0 \end{bmatrix} \quad . \tag{2.138}$$

By using superposition, the state-vector in the right part of the Equation (2.138) can be considered as

$$\begin{bmatrix} \dot{\boldsymbol{q}} \\ \boldsymbol{q} \end{bmatrix}_{t=T} = \sum_{n=1}^{2N} a_n \begin{bmatrix} \dot{\boldsymbol{q}}_n \\ \boldsymbol{q}_n \end{bmatrix}_{t=T} \quad , \tag{2.139}$$

where a_n is the coefficient of the partial solution of Equation (2.138).

By considering the proportionality of the Equation (2.139), the following equation is obtained

$$\begin{bmatrix} \dot{\boldsymbol{q}}_n \\ \boldsymbol{q}_n \end{bmatrix}_{t=T} = \mu_n \begin{bmatrix} \dot{\boldsymbol{q}}_n \\ \boldsymbol{q}_n \end{bmatrix}_{t=0} \quad . \tag{2.140}$$

Further, the characteristic multiplier can be considered as

$$[\boldsymbol{\Psi}(T) - \mu_n \boldsymbol{I}] \begin{bmatrix} \dot{\boldsymbol{q}}_n \\ \boldsymbol{q}_n \end{bmatrix} = 0 \quad . \tag{2.141}$$

The stabilities of the system can be determined by calculating the characteristic multiplier μ_n and the following conditions

- stable, if $|\mu_n| < 1$ for all $n = 1, 2, 3, ..., 2N$
- metastable, if $|\mu_n| = 1$ for at least one eigenvalue and the others $|\mu_n| < 1$
- unstable, if $|\mu_n| > 1$ for at least one eigenvalue

Direct investigation by means of spectral map of the dynamic responses

Considering of the time-varying system after Equation (2.111) can be conducted numerically, if all parameters in the equations are known. Since the matrix of bearing mass $\boldsymbol{M}_L$ is zero, the calculation is also possible by using the static condensation. Furthermore, the equations can be solved by using fourth-order Runge-Kutta method. In computing $\boldsymbol{q}(t_n)$, this method needs only the solution at the immediatelly preceding time point $\boldsymbol{q}(t_{n-1})$ [40]. Therefore, the dynamic responses $\boldsymbol{q}(t)$, especially the steady-state responses (i.e. the responses are assumed after a certain time) can be analyzed in frequency domain for example by using fast fourier transform (FFT). The responses are analyzed for all spin speeds and depicted in a spectral map.

2.10 Case study: constant angular speed

In this section, an anisotropic rotor with two different support conditions will be simulated numerically. The first condition is an anisotropic shaft with one rigid disk supported by rigid bearings and the other is the same anisotropic rotor but supported by anisotropic flexible bearings. Each type of the rotor will be analyzed at constant rotational speed. The stability of the rotor will be depicted in spectral map, frequency response function (FRF) and a non-dimensional CAMPBELL diagram.

2.10.1 Anisotropic rotor supported by rigid bearings

As depicted in Figure 2.11, the rotor shaft is modelled by two discrete elements which have different orientations of the principal axes of the element cross sections. The rotor is simply supported by two rigid bearings. In order to simplify the shaft anisotropy, a rectangular cross section of the shaft is used. The anisotropies of all shaft elements are the same and are defined as

$$\mu_W = \left| \frac{I_{\zeta^*} - I_{\eta^*}}{I_{\zeta^*} + I_{\eta^*}} \right| \quad . \tag{2.142}$$

In the numerical simulation, the coefficient μ_W of the element anisotropy is varied from 0 to 0.99. The width b of the rectangular cross section is defined to be constant and the thickness h of the cross section is formulated as

$$h = b\sqrt{\frac{1-\mu_W}{1+\mu_W}} \quad . \tag{2.143}$$

A rigid disk is also attached on the shaft at the distance ℓ_1 from the left shaft end or ℓ_2 from the right shaft end. The disk is assumed to be a thin disk with a ratio between polar mass and axial mass moment of inertia of 1.98 (i.e. disk radius = 0.06 m, disk thickness = 0.01 m). In the whole system, the internal and external dampings are neglected.

In this section, the instability areas of several models of the anisotropic rotor with different shaft orientations according to Figure 2.11 are investigated. Varying the element anisotropy from $\mu_W = 0$ to 0.99 and for various differences $\Delta\beta = 0^\circ$, 30°, 45°, 60° and 90° in the shaft orientations, a stability chart is obtained through analysis of eigenvalues according to Equation (2.125) and presented in Figure 2.12. Because the $\Delta\beta$ is defined as the difference of the orientation between the left and the right shaft ends, all possible values of the difference in the shaft orientation for the rotor models with two discrete shaft elements are between from 0° and 90°.

Based on the rotor models as mentioned above, the matrices $\boldsymbol{A}$ and $\boldsymbol{B}$ as presented in Equation (2.125) have the matrix size 8×8. Therefore, the solution of this equation gives eight complex eigenvalues (i.e. four complex conjugate pairs of eigenvalues). If the rotor rotates at a frequency in the stable area (e.g. rotational speed at $\Omega/\omega_{1\,at\,\Omega=0} < 1$ for various coefficients of the element

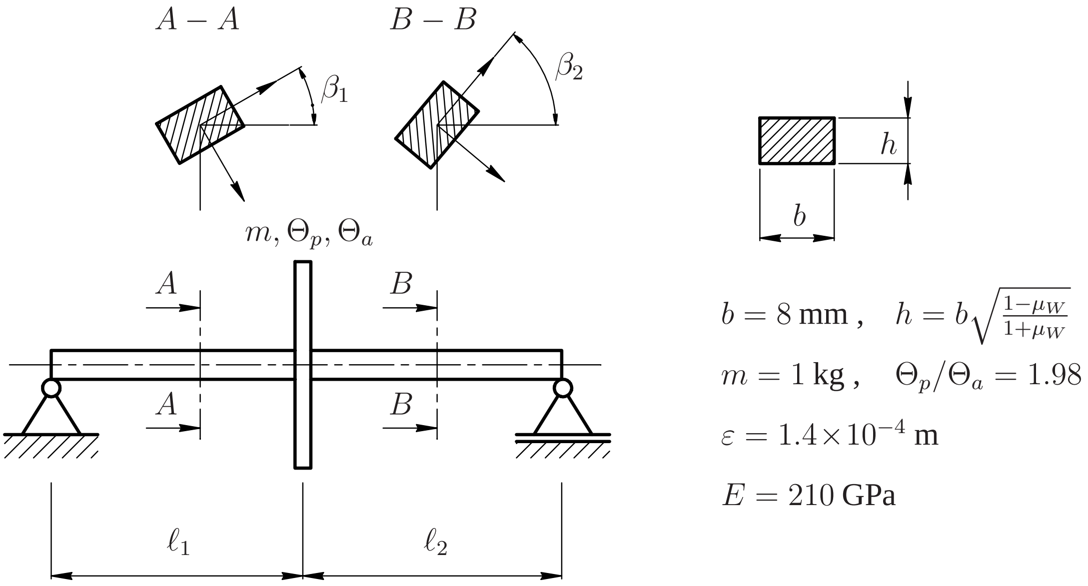

Figure 2.11: Anisotropic rotor with different shaft orientations supported by rigid bearings

anisotropy) then all eight eigenvalues are purely imaginary (i.e. the real parts of all eigenvalues are zero). In this case, if the eigenvalues are sorted and then separated into positive and negative imaginary values, they consist of four positive imaginary values which are termed forward whirl speeds ω^* and four negative imaginary values corresponding to backward whirl speeds $\bar{\omega}^*$. The natural frequencies (ω_1, ω_2, ω_3, ω_4) are considered from the forward whirl speeds at rotational speed $\Omega = 0$.

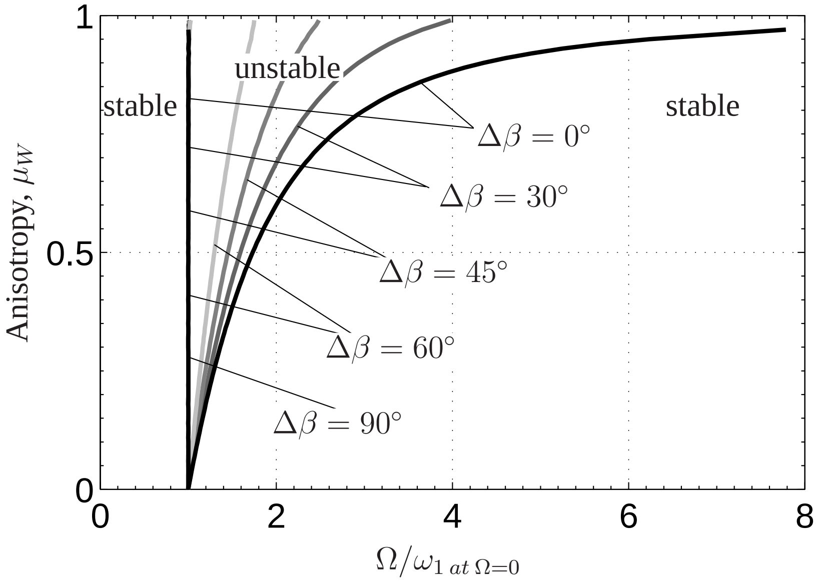

Figure 2.12: Stability chart obtained through eigenvalues analysis of undamped anisotropic rotor with sigle disk at various coefficients of the element anisotropy μ_W and the differences $\Delta\beta$ in the shaft orientation

If the rotor rotates at a frequency in the unstable area (e.g. for rotor with the coefficient of the element anisotropy $\mu_W = 0.3$, the difference $\Delta\beta = 30°$ in the shaft orientation and the rotational speed at $\Omega/\omega_{1\,at\,\Omega=0} = 1.2$), the solution of Equation (2.125) gives two of eight eigenvalues in which the values of the real parts are not zero. The other eigenvalues are purely imaginary. Similar results are obtained for the other rotor models at various coefficients of the element anisotropy and differences in the shaft orientation if the rotors rotate at frequencies in the unstable area in Figure 2.12. Through the analysis of the real parts of the complex eigenvalues, the instability area can be obtained. As discussed in [25], the vibration decays with time if the real part is negative and grows if the real part is positive.

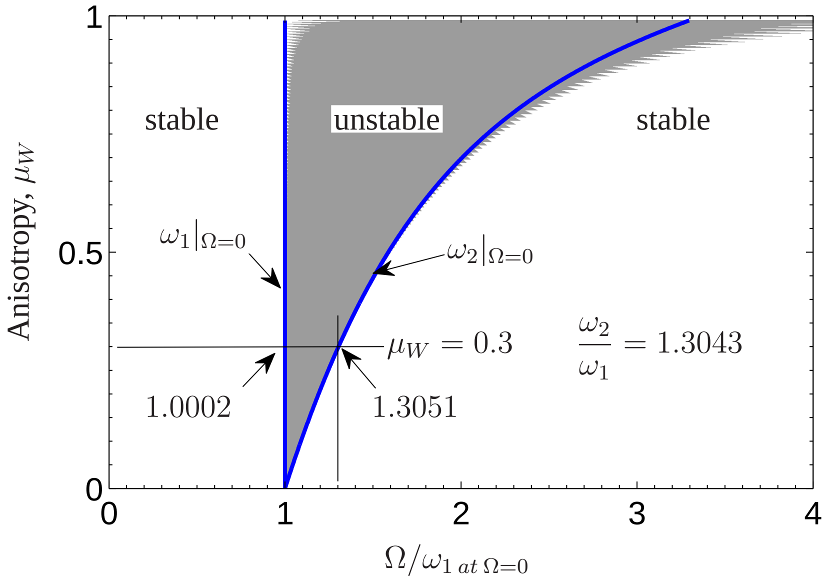

Figure 2.13: Stability chart obtained through eigenvalues analyses of the undamped anisotropic rotor with single disk and the difference $\Delta\beta = 30°$ of shaft orientation for various coefficients of the element anisotropy μ_W

The areas of stability and instability of the rotor with different shaft orentations are depicted in Figure 2.12 depending on the normalized rotational speed $\Omega/\omega_{1\,at\,\Omega=0}$. The normalized rotational speed of the rotor is defined as the ratio between rotational speed and the lowest natural frequency (ω_1) of the rotor at rest. Generally, the instability areas occur above the first natural frequency of the rotor with various ranges depending on the anisotropy and the difference in the shaft orientation. The shaft anisotropy influences the range of instabilities. The more anisotropic the shaft, the wider is the instabilty range. Comparing the anisotropic rotor with different shaft orientations ($\Delta\beta \neq 0$) to the case of a purely anisotropic rotor ($\Delta\beta = 0$), the unstable area of the purely anisotropic rotor is the widest. It means, the different shaft orientations contribute to the reduction of interval rotor instability. The bigger the difference $\Delta\beta$ in the shaft orientation, the narrower is the range of the unstable area. For the special case $\Delta\beta = 90°$, the unstable area is located only at the first natural frequency of the rotor. It means, the shaft characteristic becomes a ”quasi-round shaft".

In the following, a specific case of the simulated rotors above is analyzed in more detail. In Figure 2.13, the anisotropic rotor with $\Delta\beta = 30°$ and $\mu_W = 0.3$ has a range of instability of about $1.0002\,\omega_{1\;at\;\Omega=0}$ and $1.3051\,\omega_{1\;at\;\Omega=0}$, while the second natural frequency ω_2 is $1.3043\,\omega_1$. Hence, the instability interval is shifted slightly towards higher frequencies. In first appoximation, the stability interval is still in the range between the first and the second natural frequency of the rotor. Comparing the instability area of the anisotropic rotor at various shaft orientations to the instability area of the purely anisotropic rotor ($\Delta\beta = 0°$) in Figure 2.12, the lower and upper boundaries of the instability area of the purely anisotropic rotor coincide exactly with the first and the second natural frequencies of the rotor. As mentioned in Section 2.1, the anisotropic rotor with different shaft orientations is discretized by two shaft elements only. All elements have the same cross-sectional moment of inertia. The disk is attached symmetrically on the shaft ($\ell_1 = \ell_2$). Because of different orientation between the shaft elements, the angle position of the disk will not be equal to zero. Therefore, the effect of gyroscopic moments is no longer negligible. In this case, the occurence of the gyroscopic moments in the rotor is shown by shifting of the instability area to higher frequencies.

The system stability can also be depicted in a spectral map as shown in Figure 2.14a. The graphs are obtained by using the fast fourier transform (FFT) of the dynamic responses of the system which are analyzed at constant angular speed. In the figure, the dynamic responses at Ω and 2Ω can be shown clearly. It is well known that the main cause of dynamic responses at Ω comes from the unbalance mass of the system and at 2Ω from the anisotropy of the shaft. By projecting the spectral map along the $\omega/\omega_{1\;at\;\Omega=0}$-axis, the frequency plot in Figure 2.14b is obtained.

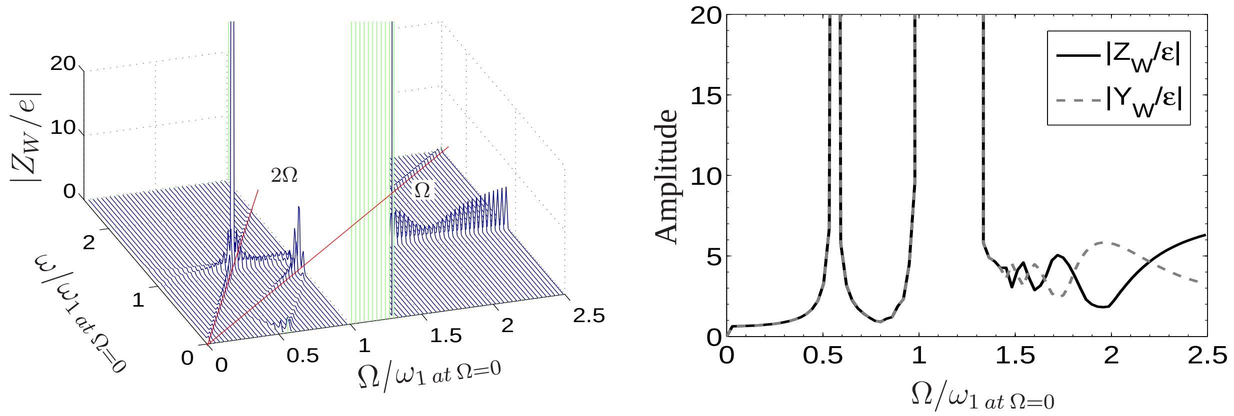

(a) (b)

Figure 2.14: (a) Spectral map and (b) dynamic responses of the undamped anisotropic rotor with single disk in frequency domain. The responses of the rotor are analyzed in fixed reference frame

While the spectral map can depict the dynamic responses of the rotor in the frequency domain including the amplitude of the responses, the CAMPBELL diagram shows the speed dependency of the natural frequency, see Figure 2.15a. In this figure, only three of the eight whirl speeds (i.e. four forward and four backward whirl speeds) are plotted. This diagram is obtained by solving the characteristic roots of the homogenous differential equations of the rotor system at each constant angular speed. Based on the Equation (2.125), the general solution of the eigenvalues can be written as

$$\lambda = \sigma + i\omega^* \quad , \tag{2.144}$$

where σ is the real part of the eigenvalues and ω^* is the whirl speed of the rotor which is analyzed in rotating reference frame. As mentioned above, the positive and negative whirl speeds are termed forward and backward whirl speeds, respectively. In order to simplify distinguishing these whirl speeds, the forward and backward whirl speed are denoted as ω^* and $\bar{\omega}^*$, respectively. These whirl speeds do not coincide with the whirl speeds ω of the rotor which is analyzed in fixed reference frame are linked by the following relationship

$$\omega^* = \omega - \Omega \quad . \tag{2.145}$$

In Figure 2.15a, the forward whirl speeds ω' have been normalized due to the first natural frequency of the rotor at rest, where

$$\omega' = \frac{\omega^* + \Omega}{\omega_{1\;at\;\Omega=0}} = \frac{\Im(\lambda) + \Omega}{\omega_{1\;at\;\Omega=0}} \quad . \tag{2.146}$$

The backward whirl speed is normalized accordingly and denoted as $\bar{\omega}'$.

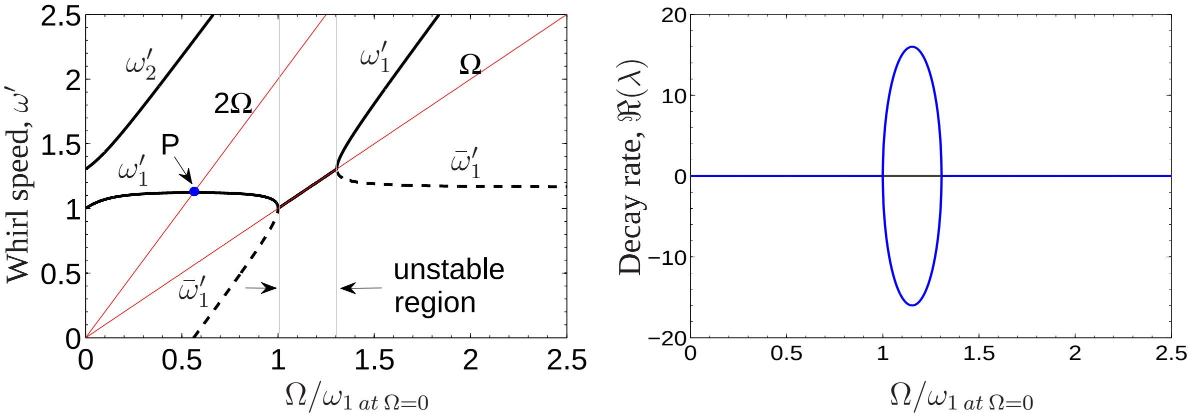

(a) (b)

Figure 2.15: (a) Non-dimensional CAMPBELL diagram of the undamped anisotropic rotor with single disk (shown only three of eight whirl speeds of the rotor) and (b) decay rate plot

Using the CAMPBELL diagram as presented in Figure 2.15a, the change in critical speeds of the rotating rotor, the forward whirl ω' and backward whirl speed $\bar{\omega}'$ can be identified. In case of the rotating rotor at frequency about 1.0 - 1.3, the first whirl speeds ω_1' and $\bar{\omega}_1'$ are the same and coincide with the Ω-line. It means, the values of the whirl speeds (ω^*) in the range of instability area according to Equation (2.145) are zero. Besides, this instability interval is shown in Figure 2.15b. In this figure, the real parts of the eight eigenvalues are plotted as the decay rate plot of the rotating rotor. In the range of the instability area (i.e. rotating rotor at frequency about 1.0 - 1.3), two of the eight eigenvalues have a non-zero real part. These real parts have positive and negative values. However, in the stable interval all of the eight eigenvalues possess purely imaginary values only.

In case of an anisotropic rotor with the weight critical phenomenon, a vibration with a frequency 2Ω will occur in the rotor. This case is depicted in Figure 2.15a and denoted as 2Ω-line. This line crosses one (or more) curve of whirl speeds. In the intersection point P, the system is not unstable, although the amplitude is relatively higher, because according to Figure 2.15b the decay rate at this rotational speed does not have a positive real part.

Comparison of different anisotropic rotors

Four cases of anisotropic rotors are discussed in this section. First, the simulation of a purely anisotropic rotor ($\Delta\beta = 0°$) supported by rigid bearings is performed. A disk is attached in the centre of the shaft. Similar to the investigation above, the model is analyzed to obtain the characteristics of stability through eigenvalue analyses of anisotropic rotor without gyroscopic moments acting on the system. In the other models, the effects of gyroscopic moments are taken into account. These effects are also distinguished into two types. In the first type, the disk is not attached in the centre of the shaft and the gyroscopic moments come only from the asymmetry of the rotor. This is simulated in Model 2. In the second type, the gyroscopic moments come only from the difference in the shaft orientation as simulated in Model 3. Finally, both sources of the gyroscopic moments from the asymmetry of the rotor and the difference in the shaft orientation are taken into account in Model 4. The parameters of the four rotor cases are listed in Table 2.1.

Table 2.1: Parameter of rotor cases

Model	ℓ_1 [m]	ℓ_2 [m]	β_1 [°]	β_2 [°]	Chart
1	0.25	0.25	0	0	Figure 2.16a
2	0.10	0.40	0	0	Figure 2.16b
3	0.25	0.25	0	30	Figure 2.16c
4	0.10	0.40	0	30	Figure 2.16d

The results of the stability investigations are depicted in Figure 2.16. The figures show the stability charts which are obtained through eigenvalue analyses for the four rotor models with variation of the element anisotropy and the difference in the shaft orientation. The shape of the stability areas of all rotor cases are similar. The shaft anisotropy influences the interval of instability. The more anisotropic the rotor, the wider is the instability range. For further analysis, each chart is investigated at the element anisotropies $\mu_W = 0.2$, 0.3, 0.5. The results are listed in Tables 2.2 - 2.4.

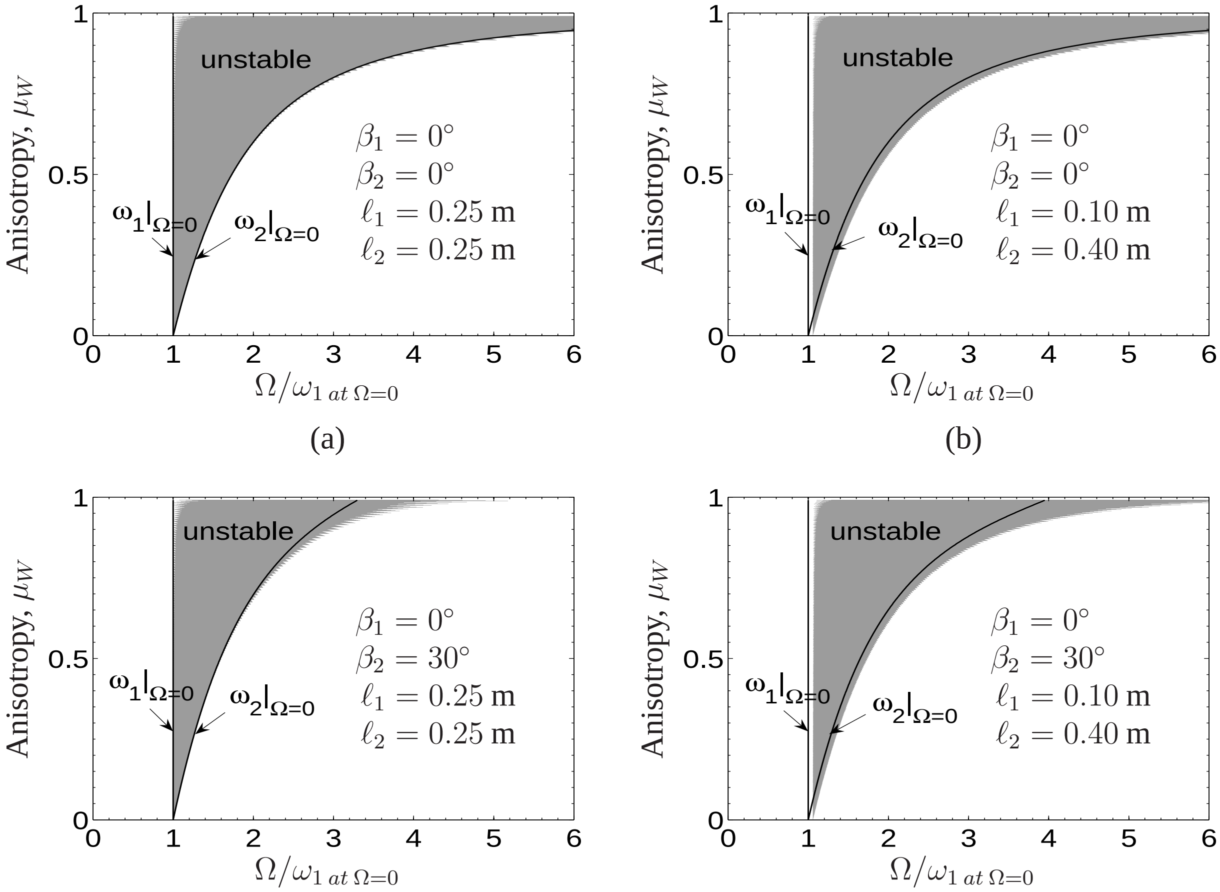

(a) (b)

(c) (d)

Figure 2.16: Comparison of stability charts of undamped anisotropic rotor cases with single disk: (a) Model 1, (b) Model 2, (c) Model 3 and (d) Model 4. The natural frequencies of the rotor are obtained at rotational speed $\Omega = 0$ (shown only two of four natural frequencies)

In case of the purely anisotropic rotor, the instability area as depicted in Figure 2.16a lies exactly in the range between the first and the second natural frequency of the anisotropic rotor. The coefficient of the element anisotropy is varied between $\mu_W = 0$ and 0.99. At each coefficient of the element anisotropy, the first and the second natural frequencies are considered as the forward whirl speeds at rotational speed $\Omega = 0$. These natural frequencies have been normalized by the first natural frequency. Because of purely anisotropic along the rotor shaft, the first and second natural frequencies of the rotor correspond to the mode of U-form of the shaft bending in each direction of shaft cross-section. At the third and the fourth natural frequencies the rotor modes have S-form of the shaft bending and no instability exists. The instability area depicted in Figure 2.16a is equivalent to the case of a purely anisotropic rotor investigated in [11] or [48].

Table 2.2: Rotor Cases with Anisotropy of Element, $\mu_W = 0.2$

Model	ω_1 [rad/s]	ω_2 [rad/s]	Lower boundary of unstable area [rad/s]	Upper boundary of unstable area [rad/s]	Width [rad/s]	Movement due to ω_1 [%]	Movement due to ω_2 [%]
1	122.40	149.91	122.40	149.91	27.51	0.00	0.00
2	185.86	227.63	196.76	240.97	44.21	5.86	5.86
3	123.79	147.45	123.80	147.48	23.68	0.01	0.02
4	187.00	225.54	198.32	238.24	39.92	6.05	5.63

Table 2.3: Rotor Cases with Anisotropy of Element, $\mu_W = 0.3$

Model	ω_1 [rad/s]	ω_2 [rad/s]	Lower boundary of unstable area [rad/s]	Upper boundary of unstable area [rad/s]	Width [rad/s]	Movement due to ω_1 [%]	Movement due to ω_2 [%]
1	104.29	142.12	104.29	142.12	37.83	0.00	0.00
2	158.35	215.79	167.64	228.44	60.80	5.87	5.86
3	105.93	138.16	105.95	138.25	32.30	0.02	0.07
4	159.70	212.40	169.50	224.09	54.59	6.14	5.50

Table 2.4: Rotor Cases with Anisotropy of Element, $\mu_W = 0.5$

Model	ω_1 [rad/s]	ω_2 [rad/s]	Lower boundary of unstable area [rad/s]	Upper boundary of unstable area [rad/s]	Width [rad/s]	Movement due to ω_1 [%]	Movement due to ω_2 [%]
1	72.78	126.06	72.78	126.06	53.28	0.00	0.00
2	110.51	191.41	117.00	202.63	85.63	5.87	5.86
3	74.44	118.19	74.48	118.56	44.08	0.05	0.31
4	111.87	184.45	118.90	194.16	75.26	6.28	5.26

In Figure 2.16b, the instability area of the Model 2 is presented. In this model, the position of the disk is asymmetric on the shaft and the rotor is purely anisotropic. Therefore, the significant gyroscopic moments will occur in the system. The increase of gyroscopic moments cause the stiffness of the rotor stiffer and the instability range is wider. Comparing the lower and upper boundaries of the instability area to the first and the second natural frequencies as listed in Tables 2.2 - 2.4, these boundaries are shifted about $5.86\,\%$ to higher frequencies.

In Model 3, the anisotropic rotor with a thin disk attached symmetrically ($\ell_1 = \ell_2 = 0.25$ m) on the shaft has different shaft orientations ($\beta_1 = 0°$ and $\beta_2 = 30°$) according to Figure 2.11 and the instability area of the model is plotted in Figure 2.16c. In this case, the inclination of the disk will not be equal to zero. Therefore, the gyroscopic moments still occur in the system, although they are negligible especially for lower values of μ_W. Based on the Tables 2.2 - 2.4, it is observed that the higher the coefficient of the element anisotropy of the shaft, the higher is the shift of the instability area to higher frequencies due to the first and the second natural frequencies. Nevertheless, the difference in the shaft orientation affects the reduction of the interval of the instability range.

The case of an anisotropic rotor with the disk located asymmetrically on the shaft ($\ell_1 \neq \ell_2$) together with the difference $\Delta\beta = 30°$ in the shaft orientation is described in Model 4. The instability area of this model is presented in Figure 2.16d. The parameters of the asymmetry position of the disk and the difference in the shaft orientation show the same effect in shifting the instability area to higher frequencies but a contrary effect in reduction the width of instability according to the Tables 2.2 - 2.4. While the asymmetric rotor increases, the difference in the shaft orientation decreases the width of instability.

2.10.2 Anisotropic rotor supported by anisotropic flexible bearings

In this section, a model of an anisotropic rotor supported by anisotropic flexible bearings is presented. A sketch of the anisotropic rotor model is shown in Figure 2.17. The following assumptions are made: the rotor is modelled as a massless shaft and a thin rigid disk is attached in the centre of the shaft ($\ell_1 = \ell_2 = 0.25$ m and $\Theta_p/\Theta_a = 1.98$). In order to simplify the differential equations of the rotor, the shaft is discretized by two discrete elements. Each element has the same dimension (i.e. length and rectangular cross section) but has different shaft orientations. The difference in the shaft orientation is set to $\Delta\beta$. Because of similarity of the resulting stability charts, only the anisotropic rotor with $\Delta\beta = 30°$ will be presented here. The present rotor model is equivalent to the Model 3 in Section 2.10.1 except the supporting conditions.

In the numerical simulation, the coefficient of the element anisotropy μ_W is varied from 0 to 0.8. The width b of the rectangular cross section is defined to be constant and the thickness h of the cross section is formulated as described in Equation (2.143).

The anisotropy in the bearing stiffness is considered by using the following formulations

$$\mu_{L_1} = \left| \frac{c_{1z} - c_{1y}}{c_{1z} + c_{1y}} \right| \qquad \text{and} \qquad \mu_{L_2} = \left| \frac{c_{2z} - c_{2y}}{c_{2z} + c_{2y}} \right| \quad , \tag{2.147}$$

where c_{1z} and c_{1y} are the stiffness parameters of the bearings on the left shaft end in z-direction and y-direction, respectively, and c_{2z} and c_{2y} on the right shaft end. The bearing stiffness in the z-direction are $c_{1z} = c_{2z} = 13\,763$ N/m. In this section, the anisotropic rotor with two different anisotropies of the bearing stiffness with $\mu_{L_1} = \mu_{L_2} = \mu_L = 0.3$ (i.e. $c_{1y} = c_{2y} = 7\,411$ N/m) and 0.6 (i.e. $c_{1y} = c_{2y} = 3\,441$ N/m) is simulated.

Because the equations of motion of the rotor system are time-variant, the FLOQUET theory is applied to obtain the stability charts as depicted in Figure 2.18. In the figures, the instability areas are shaded as grey area. Due to numerical restriction, narrow instability tongues between $\Omega/\omega = 2$ and 3 cannot be resolved.

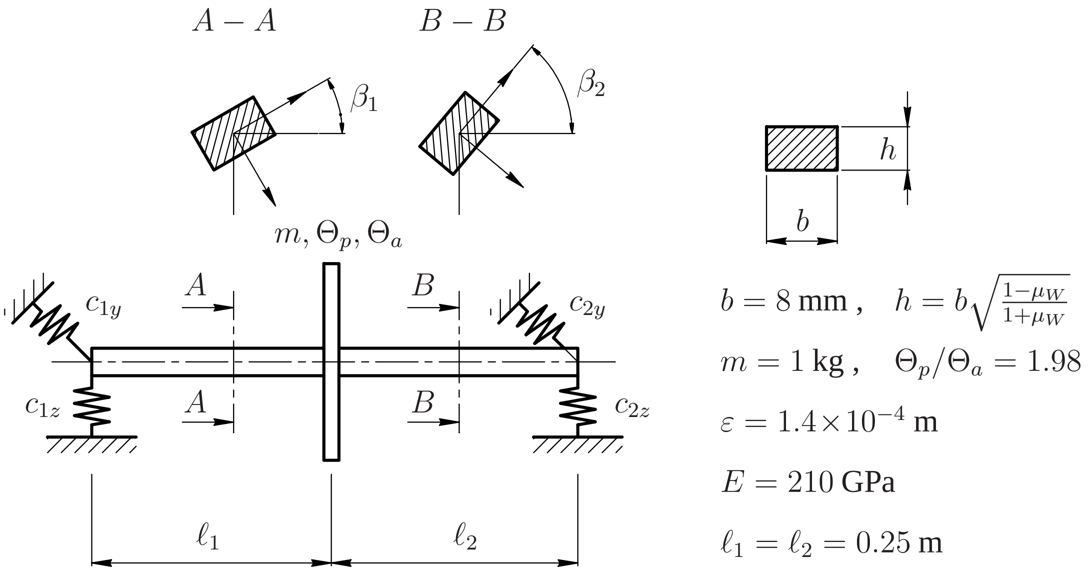

Figure 2.17: Anisotropic rotor with different shaft orientation supported by anisotropic flexible bearings

The stability chart of the anisotropic rotor supported by anisotropic flexible bearings as presented in Figure 2.18 is compared to the rotor which has the same parameters but is supported by rigid bearings in Figure 2.16c. While the stability chart of the rotor supported by rigid bearings has only a single region of instability in the whole varying coefficients of the element anisotropy, the rotor in flexible bearings has three separated intervals of instabilities at lower values of the element anisotropy. The anisotropy coefficient of the bearing stiffness affects the region where the three separated

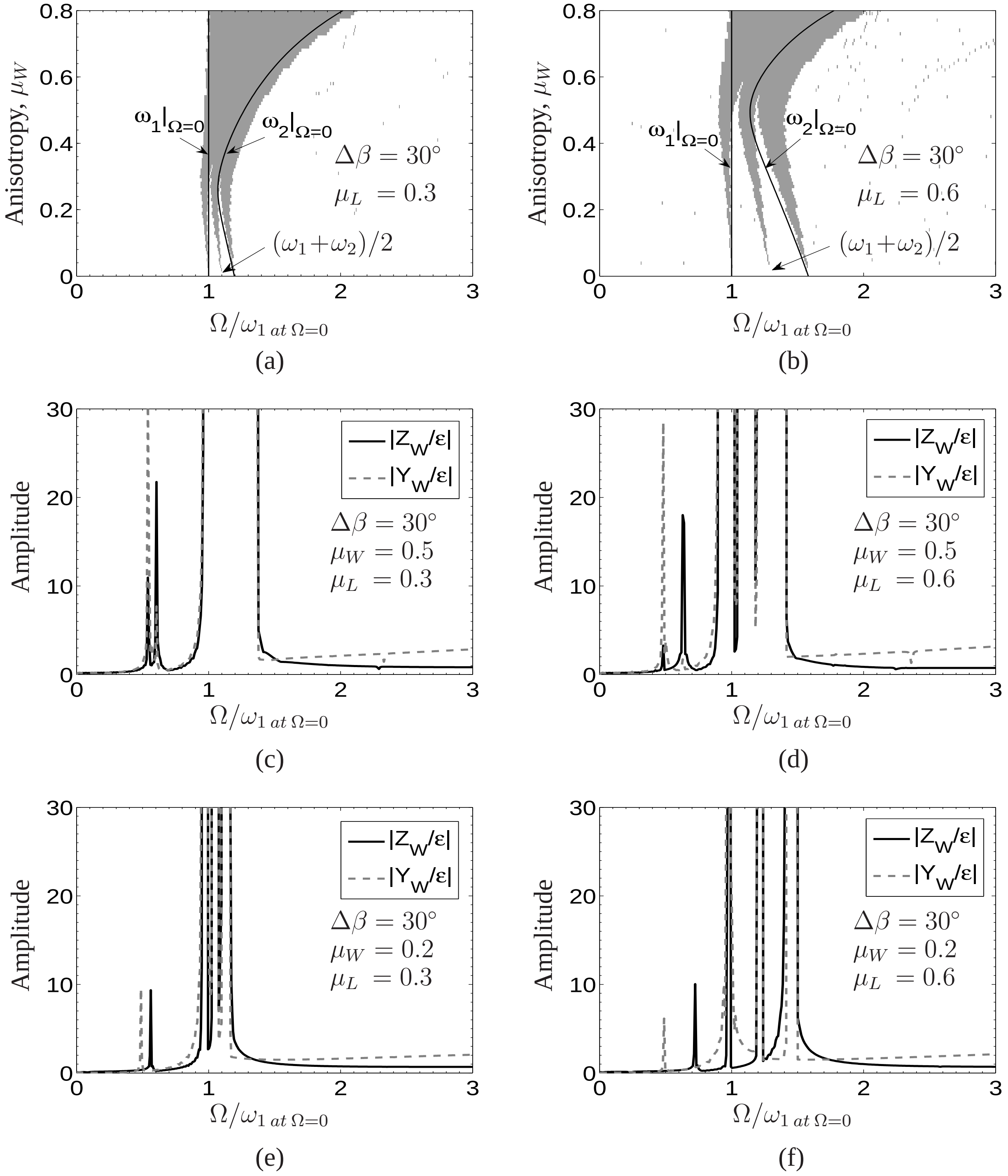

Figure 2.18: Stability charts according to FLOQUET of various coefficients of anisotropy ($\mu_W = 0$ to 0.8) of the undamped anisotropic rotor with single disk and the difference $\Delta\beta = 0°$ in the shaft orientation supported by anisotropic flexible bearings with (a) $\mu_L = 0.3$ and (b) $\mu_L = 0.6$. The dynamic responses in frequency domain of the rotor for anisotropy $\mu_W = 0.5$ supported by anisotropic flexible bearings with the coefficient (c) $\mu_L = 0.3$ and (d) $\mu_L = 0.6$ and for anisotropy $\mu_W = 0.2$ with (e) $\mu_L = 0.3$ and (f) $\mu_L = 0.6$

instability intervals emerge to a single interval at higher element anisotropy of the shaft. The higher the anisotropy coefficient of the bearing stiffness, the three separated regions of instabilities reach to a higher element anisotropy of the shaft. For the anisotropic rotor with the anisotropic coefficient of the bearing stiffness $\mu_{L_1} = \mu_{L_2} = \mu_L = 0.3$, the three separated regions of instability reach to the element anisotropy $\mu_W < 0.32$ of the shaft. For the same rotor with $\mu_{L_1} = \mu_{L_2} = \mu_L = 0.6$ reachs to $\mu_W < 0.56$.

For reference, the first and the second natural frequencies of the rotor-bearing system are also plotted in Figure 2.18a and b. In this case, the natural frequencies of the system are obtained by solving the characteristic roots of the homogenous differential equations of motion of the rotor according to Equation (2.111) after static condensation at rotational speed $\Omega = 0$ and time $t = 0$. At this condition, the first and the second natural frequencies of the system differ. Therefore, this system is unstable at rotational speed in these natural frequencies. Similar to [11], the second region of the instability at vanishing shaft anisotropy $\mu_W = 0$ is located at $(\omega_1 + \omega_2)/2$.

Furthermore, the comparison of dynamic responses in the frequency domain are plotted in Figures 2.18c, d, e and f. The figures show the responses in frequency domain of the rotor for each coefficient of the element anisotropy $\mu_W = 0.2$ and 0.5 and supported by anisotropic flexible bearings with the coefficient $\mu_{L_1} = \mu_{L_2} = \mu_L = 0.3$ (Figure 2.18c and e) and with $\mu_{L_1} = \mu_{L_2} = \mu_L = 0.6$ (Figure 2.18d and f). It is clear that the instability areas occur if the amplitudes of responses are very high either in z-direction or in y-direction. However, although the amplitudes of the weight critical speed (i.e. at normalized rotational speed about 0.5 - 0.7) are relatively high, but they are not defined as unstable areas in the FLOQUET stability charts.

2.11 Case study: acceleration through critical speeds

Several investigations have been published that study the characteristics of a rotor which runs through its critical speeds. However, most of these investigations dealt with the purely anisotropic rotors only, as outlined in Section 1. In the present work, the anisotropic rotors are presented with and without difference $(\Delta\beta)$ in the shaft orientation , which run through the range of the critical speeds. The first model is a rectangular rotor as defined by the Model 1 in Section 2.10.1. The coefficient of the element anisotropy is varied as $\mu_W = 0$, 0.2, 0.3 and 0.5. The internal and external dampings are set to $D_i = 0.001$ and $D_a = 0.02$, respectively. Other parameters are $(\varepsilon/\kappa)^2 = 10^{-5}$, where ε is the eccentricity of disk and κ is the gyration radius of the disk defined as

$$\kappa = \sqrt{\frac{\Theta_p}{m}} \quad . \tag{2.148}$$

By introducing a constant angular acceleration in the models, the result as depicted in Figure 2.19 is obtained. The figure shows the dynamic responses and the increase in angular speed of the rotor

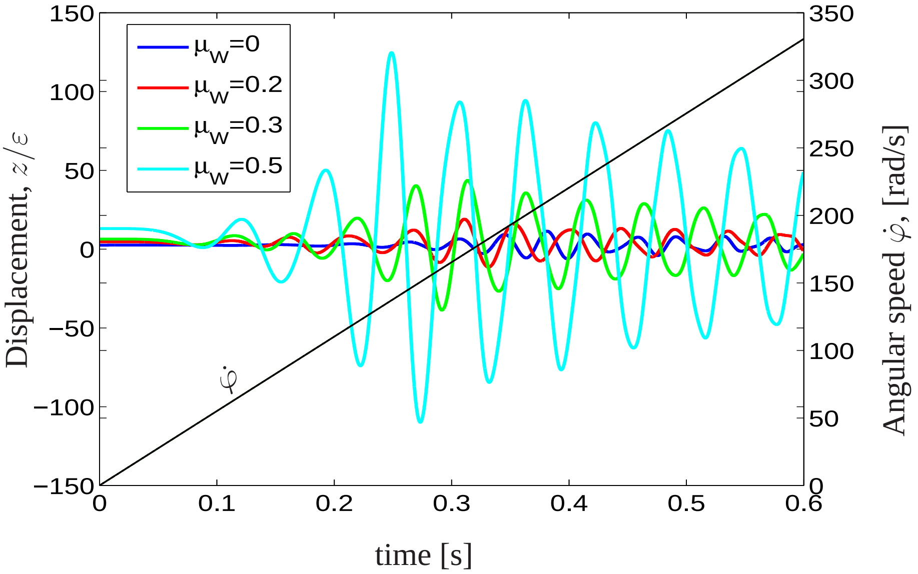

Figure 2.19: Dynamic responses of the damped purely anisotropic rotor ($D_a = 0.02$, $D_i = 0.001$ and $\Delta\beta = 0^\circ$) with single disk and various anisotropy coefficients μ_W of the shaft accelerated through the range of the critical speeds

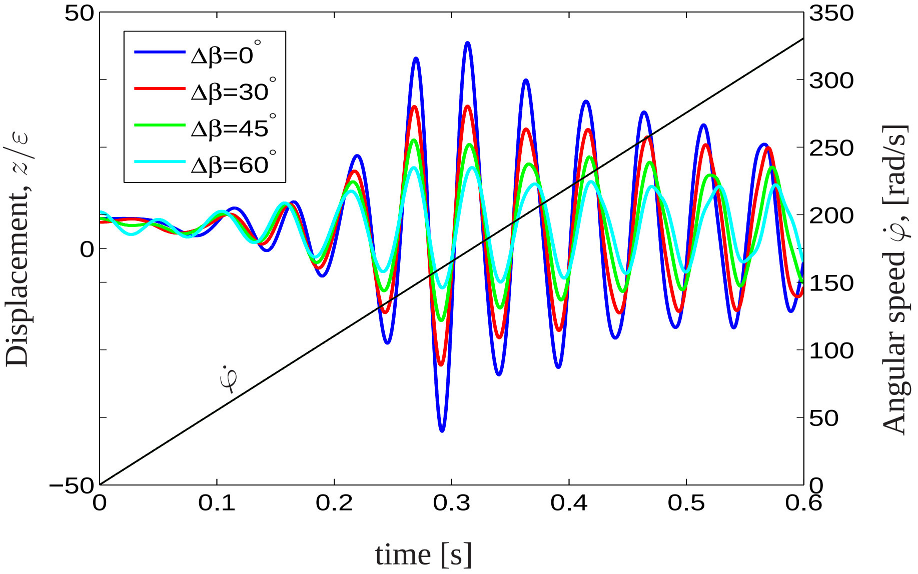

Figure 2.20: Dynamic responses of the damped anisotropic rotor with single disk and $\mu_W = 0.3$ for various differences $\Delta\beta = 0^\circ$, 30°, 45° and 60° in the shaft orientations accelerated through the range of the critical speeds

through the first range of the critical speeds at different values of the element anisotropy μ_W. By using the same value of the acceleration ($a = 0.02\,\omega^2_{1\,at\,\Omega=0} \approx 551\,$rad/s^2), the increase in angular speed is linear and the reached maximum amplitudes depend on the element anisotropy μ_W in the rotor. The higher the element anisotropy coefficient in the rotor, the higher is the reached maximum amplitude.

Furthermore, the anisotropic rotor with the shaft anisotropy $\mu_W = 0.3$ is simulated at various differences $\Delta\beta = 0°$, $30°$, $45°$ and $60°$ in the shaft orientations, see Figure 2.20. The bigger the difference in the shaft orientation, the lower is the maximum amplitude. In the previous section, it is well known that the different orientations of the shaft influence the interval of instability. The bigger the difference in the shaft orientation, the narrower is the range of instability. It means, the different shaft orientations do not only lead to a narrower range of instability but also to a lower level of instability.

Chapter 3

Anisotropic shaft with multiple disks and different shaft orientation

In this chapter, an anisotropic rotor with different shaft orientations which has N_d rigid disks is analyzed. Starting with a general rotor model, the differential equations of the rotor will be developed. Several examples of anisotropic rotor models will be presented. A special case of a twisted anisotropic shaft with two disks is also investigated. The stability charts for all rotor models are ilustrated.

3.1 Rotor model

As shown in Figure 3.1, a general rotor model which has many disks along the shaft is supported by two anisotropic flexible bearings at the ends of the shaft. The points L_1 and L_2 between shaft and bearings define the position of the left and the right bearing, respectively. A number of N_d rigid disks is attached on the rotor and the shaft is discretized into $(N_e = N_d + 1)$ elements. The joint point between two shaft elements is denoted as a node. A disk can be attached only in a node. Because each rigid disk in the rotor has four degrees of freedom, a rotor system supported by anisotropic flexible bearings has $(N = 4N_d + 4)$ degrees of freedom, whereas a rotor system supported by rigid bearings has $(N = 4N_d)$ degrees of freedom only. For the case of a rotor supported by rigid bearings, the motions in the bearings are assumed to be zero or the bearing stiffnesses are assumed to be infinite.

In order to simplify the structure of the equations of motion in matrix notation, the numbering of nodes is started from the first disk in the left position. It is possible that the first disk is numbered with an arbitrary number but this makes the structure of matrix unnecessarily complicated. Each node has four degrees of freedom. At a shaft node, the positive sign rule is used in numbering the forces and the displacements. The first step is to number the displacement and force in translational direction in ζ-axis and then in η-axis. The next step is to number the rotational displacement and moment in ζ-axis and then in η-axis. Further, because the flexible bearing is assumed to consist of a linear spring and damper (i.e. massless bearing), only two translational directions are defined in each bearing. Therefore, there are four degrees of freedom in total for the left and the right bearings. Generally, the numbering rule corresponds to Chapter 2. Note that, the rotor is modelled in the rotating reference frame denoted by the (x, η, ζ)-coordinate system.

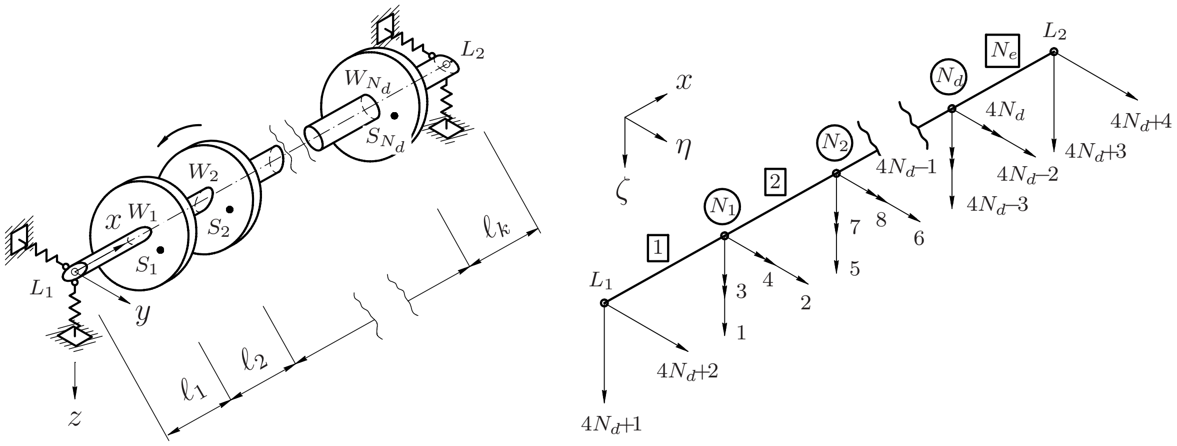

Figure 3.1: Model of multiple disks rotor with different shaft orientations

As discussed in Section 2.7, if the number of disks is less than the number of nodes then there are several dummy disks which have zero masses in the model. In order to eliminate the singularity of the diagonal of mass matrix, the method of static condensation is used (see Section 2.8).

3.2 Dynamic parameters of anisotropic rotor supported by rigid bearings

The same procedures with the assembly of differential equations of anisotropic rotor as in Section 2 are applied. All dynamic parameters of the anisotropic rotor model with multiple disks are considered. The concept of flexibility influence coefficients is developed based on the model in Figure 3.1. Because the support conditions, i.e. rigid or flexible bearings, influence the differential equations of the rotor (speed-dependent or time-variant), the assembly of the system matrices are distinguished into these two types of support conditions.

3.2.1 Flexibility matrix of shaft

In order to consider the stiffness matrix of a shaft, especially for a rotor with many degrees of freedom and different orientation in each element, the same formulation developed in Section

(2.5.1) for the rotor with two elements is used.

Let indices k and n be defined as the number of shaft elements and nodes, respectively.

For $i=4n-3, 4n$ and $j=4n-3, 4n$ with $n=1, 2, ..., N_d$

$$h_{ij} = \sum_{k=1}^{N_e} \int_{(\ell_k)} \frac{I_{k\zeta}}{E\left(I_{k\eta} I_{k\zeta} - I_{k\eta\zeta}^2\right)} \hat{M}_{ik\eta}(x)\, \hat{M}_{jk\eta}(x)\ dx \quad . \tag{3.1}$$

For $i=4n-2, 4n-1$ and $j=4n-2, 4n-1$ with $n=1, 2, ..., N_d$

$$h_{ij} = \sum_{k=1}^{N_e} \int_{(\ell_k)} \frac{I_{k\eta}}{E\left(I_{k\eta} I_{k\zeta} - I_{k\eta\zeta}^2\right)} \hat{M}_{ik\zeta}(x)\, \hat{M}_{jk\zeta}(x)\ dx \quad . \tag{3.2}$$

For $i=4n-3, 4n$ and $j=4n-2, 4n-1$ with $n=1, 2, ..., N_d$

$$h_{ij} = \sum_{k=1}^{N_e} \int_{(\ell_k)} \frac{-I_{k\eta\zeta}}{E\left(I_{k\eta} I_{k\zeta} - I_{k\eta\zeta}^2\right)} \hat{M}_{ik\eta}(x)\, \hat{M}_{jk\zeta}(x)\ dx \quad . \tag{3.3}$$

The components h_{ij} which are termed as flexibility influence coefficients can be arranged in a matrix with the size $4N_d \times 4N_d$ as

$$\boldsymbol{H} = \begin{bmatrix} h_{11} & h_{12} & \cdots & h_{1(4N_d)} \\ & h_{22} & \cdots & h_{2(4N_d)} \\ symm & & \ddots & \vdots \\ & & & h_{(4N_d)(4N_d)} \end{bmatrix} \quad . \tag{3.4}$$

Furthermore, by inverting the flexibility matrix in Equation (3.4), the stiffness matrix of the shaft can be obtained

$$\boldsymbol{C}_W = \boldsymbol{H}^{-1} \quad . \tag{3.5}$$

Shaft bending forces in rotating reference frame can be determined based on the stiffness matrix in Equation (3.5). In formulation, these forces are written in negative sign, hence

$$\begin{bmatrix} f_{c_1} \\ f_{c_2} \\ \vdots \\ f_{c_{(4N_d)}} \end{bmatrix} = - \begin{bmatrix} c_{11} & c_{12} & \cdots & c_{1(4N_d)} \\ & c_{22} & \cdots & c_{2(4N_d)} \\ symm & & \ddots & \vdots \\ & & & c_{(4N_d)(4N_d)} \end{bmatrix} \begin{bmatrix} q_1 \\ q_2 \\ \vdots \\ q_{(4N_d)} \end{bmatrix} \tag{3.6}$$

or rewritten in simple form

$$\boldsymbol{f}_c = -\boldsymbol{C}_W\, \boldsymbol{q}_W \quad . \tag{3.7}$$

3.2.2 Damping matrix of shaft

As presented in Section 2.5.2, the damping of rotor is separated into internal and external dampings. Since the stiffness matrix of the shaft is obtained in Equation (3.5), the internal damping matrix can be considered according to Equation (2.56). Therefore, the internal damping matrix for the anisotropic rotor with multiple disks can be written in matrix notation as

$$\boldsymbol{D}_i = \begin{bmatrix} d_{11} & d_{12} & \cdots & d_{1(4N_d)} \\ & d_{22} & \cdots & d_{2(4N_d)} \\ symm & & \ddots & \vdots \\ & & & d_{(4N_d)(4N_d)} \end{bmatrix} \quad . \tag{3.8}$$

Further, the internal damping forces that act on the shaft can be defined as a multiplication of the internal damping matrix and the vector of velocity. Because these forces are reaction damping forces, they are denoted by a negative sign, hence

$$\begin{bmatrix} f_{i_1} \\ f_{i_2} \\ \vdots \\ f_{i_{(4N_d)}} \end{bmatrix} = - \begin{bmatrix} d_{11} & d_{12} & \cdots & d_{1(4N_d)} \\ & d_{22} & \cdots & d_{2(4N_d)} \\ symm & & \ddots & \vdots \\ & & & d_{(4N_d)(4N_d)} \end{bmatrix} \begin{bmatrix} \dot{q}_1 \\ \dot{q}_2 \\ \vdots \\ \dot{q}_{(4N_d)} \end{bmatrix} \tag{3.9}$$

or rewritten in simple form

$$\boldsymbol{f}_i = -\boldsymbol{D}_i \, \dot{\boldsymbol{q}}_W \quad . \tag{3.10}$$

Furthermore, the external damping matrix with the size $4N_d \times 4N_d$ can be obtained according to Equation (2.67). If the coefficients in the Equation (2.67) are denoted as

$$\boldsymbol{f}_{a_{N_1}} = -\boldsymbol{D}_{a_{N_1}} \dot{\boldsymbol{q}}_{N_1} - \boldsymbol{C}_{a_{N_1}} \boldsymbol{q}_{N_1} + \boldsymbol{p}_{a_{N_1}} \tag{3.11}$$

then the external damping forces for anisotropic rotor with multiple disks can be written as follows

$$\begin{bmatrix} \boldsymbol{f}_{a_{N_1}} \\ \boldsymbol{f}_{a_{N_2}} \\ \vdots \\ \boldsymbol{f}_{a_{N_d}} \end{bmatrix} = - \begin{bmatrix} \boldsymbol{D}_{a_{N_1}} & & & \\ & \boldsymbol{D}_{a_{N_2}} & & \\ & & \ddots & \\ & & & \boldsymbol{D}_{a_{N_d}} \end{bmatrix} \begin{bmatrix} \dot{\boldsymbol{q}}_{N_1} \\ \dot{\boldsymbol{q}}_{N_2} \\ \vdots \\ \dot{\boldsymbol{q}}_{N_d} \end{bmatrix} - \begin{bmatrix} \boldsymbol{C}_{a_{N_1}} & & & \\ & \boldsymbol{C}_{a_{N_2}} & & \\ & & \ddots & \\ & & & \boldsymbol{C}_{a_{N_d}} \end{bmatrix} \begin{bmatrix} \boldsymbol{q}_{N_1} \\ \boldsymbol{q}_{N_2} \\ \vdots \\ \boldsymbol{q}_{N_d} \end{bmatrix} + \begin{bmatrix} \boldsymbol{p}_{a_{N_1}} \\ \boldsymbol{p}_{a_{N_2}} \\ \vdots \\ \boldsymbol{p}_{a_{N_d}} \end{bmatrix} \quad . \tag{3.12}$$

Now, the Equation (3.12) can be rewritten in simple form as

$$\boldsymbol{f}_a = -\boldsymbol{D}_a \, \dot{\boldsymbol{q}}_W - \boldsymbol{C}_a \, \boldsymbol{q}_W + \boldsymbol{p}_a \quad . \tag{3.13}$$

3.2.3 Differential equations of translatory inertia

Because the mass matrix in the rotor system is uncoupled, the differential equations of translatory inertia can be arranged analoque to the arranging of external damping forces as mentioned in Equation (3.12). If the Equation (2.72) is denoted as

$$\boldsymbol{M}_{T_{N_1}} \ddot{\boldsymbol{q}}_{N_1} + \boldsymbol{D}_{T_{N_1}} \dot{\boldsymbol{q}}_{N_1} + \boldsymbol{C}_{T_{N_1}} \boldsymbol{q}_{N_1} - \boldsymbol{p}_{T_{N_1}} = \boldsymbol{f}_{T_{N_1}} \tag{3.14}$$

then the differential equations for rotor with N_d disks on the shaft can be written in simple form as

$$\boldsymbol{M}_T \ddot{\boldsymbol{q}} + \boldsymbol{D}_T \dot{\boldsymbol{q}} + \boldsymbol{C}_T \boldsymbol{q} - \boldsymbol{p}_T = \boldsymbol{f}_T \quad , \tag{3.15}$$

where

$$\begin{bmatrix} \boldsymbol{M}_{T_{N_1}} & & & \\ & \boldsymbol{M}_{T_{N_2}} & & \\ & & \ddots & \\ & & & \boldsymbol{M}_{T_{N_d}} \end{bmatrix} \begin{bmatrix} \ddot{\boldsymbol{q}}_{N_1} \\ \ddot{\boldsymbol{q}}_{N_2} \\ \vdots \\ \ddot{\boldsymbol{q}}_{N_d} \end{bmatrix} + \begin{bmatrix} \boldsymbol{D}_{T_{N_1}} & & & \\ & \boldsymbol{D}_{T_{N_2}} & & \\ & & \ddots & \\ & & & \boldsymbol{D}_{T_{N_d}} \end{bmatrix} \begin{bmatrix} \dot{\boldsymbol{q}}_{N_1} \\ \dot{\boldsymbol{q}}_{N_2} \\ \vdots \\ \dot{\boldsymbol{q}}_{N_d} \end{bmatrix}$$
$$+ \begin{bmatrix} \boldsymbol{C}_{T_{N_1}} & & & \\ & \boldsymbol{C}_{T_{N_2}} & & \\ & & \ddots & \\ & & & \boldsymbol{C}_{T_{N_d}} \end{bmatrix} \begin{bmatrix} \boldsymbol{q}_{N_1} \\ \boldsymbol{q}_{N_2} \\ \vdots \\ \boldsymbol{q}_{N_d} \end{bmatrix} - \begin{bmatrix} \boldsymbol{p}_{T_{N_1}} \\ \boldsymbol{p}_{T_{N_2}} \\ \vdots \\ \boldsymbol{p}_{T_{N_d}} \end{bmatrix} = \begin{bmatrix} \boldsymbol{f}_{T_{N_1}} \\ \boldsymbol{f}_{T_{N_2}} \\ \vdots \\ \boldsymbol{f}_{T_{N_d}} \end{bmatrix} \quad . \tag{3.16}$$

Note that, the gravitational forces as derived in Equation (2.69) and (2.70) should be taken into account as part of $\boldsymbol{f}_{T_{N_1}}$ in Equation (3.14). For rotor with N_d disk, these gravitational forces can be written in matrix notation as

$$\boldsymbol{p}_g = \begin{bmatrix} \boldsymbol{p}_{g_{N_1}} \\ \boldsymbol{p}_{g_{N_2}} \\ \vdots \\ \boldsymbol{p}_{g_{N_d}} \end{bmatrix} \quad . \tag{3.17}$$

3.2.4 Differential equations of rotary inertia

Similar to Section 3.2.3, the differential equations of rotary inertia based on the Equation (2.76) can be arranged as follows

$$\boldsymbol{M}_{G_{N_1}} \ddot{\boldsymbol{q}}_{N_1} + \boldsymbol{D}_{G_{N_1}} \dot{\boldsymbol{q}}_{N_1} + \boldsymbol{C}_{G_{N_1}} \boldsymbol{q}_{N_1} = \boldsymbol{f}_{G_{N_1}} \quad . \tag{3.18}$$

Furthermore, the differential equations for rotor with N_d disks on the shaft can be written in matrix notation as

$$\begin{bmatrix} \boldsymbol{M}_{G_{N_1}} & & & \\ & \boldsymbol{M}_{G_{N_2}} & & \\ & & \ddots & \\ & & & \boldsymbol{M}_{G_{N_d}} \end{bmatrix} \begin{bmatrix} \ddot{\boldsymbol{q}}_{N_1} \\ \ddot{\boldsymbol{q}}_{N_2} \\ \vdots \\ \ddot{\boldsymbol{q}}_{N_d} \end{bmatrix} + \begin{bmatrix} \boldsymbol{D}_{G_{N_1}} & & & \\ & \boldsymbol{D}_{G_{N_2}} & & \\ & & \ddots & \\ & & & \boldsymbol{D}_{G_{N_d}} \end{bmatrix} \begin{bmatrix} \dot{\boldsymbol{q}}_{N_1} \\ \dot{\boldsymbol{q}}_{N_2} \\ \vdots \\ \dot{\boldsymbol{q}}_{N_d} \end{bmatrix}$$

$$+ \begin{bmatrix} \boldsymbol{C}_{G_{N_1}} & & & \\ & \boldsymbol{C}_{G_{N_2}} & & \\ & & \ddots & \\ & & & \boldsymbol{C}_{G_{N_d}} \end{bmatrix} \begin{bmatrix} \boldsymbol{q}_{N_1} \\ \boldsymbol{q}_{N_2} \\ \vdots \\ \boldsymbol{q}_{N_d} \end{bmatrix} = \begin{bmatrix} \boldsymbol{f}_{G_{N_1}} \\ \boldsymbol{f}_{G_{N_2}} \\ \vdots \\ \boldsymbol{f}_{G_{N_d}} \end{bmatrix} \tag{3.19}$$

or rewritten in simple form

$$\boldsymbol{M}_G \, \ddot{\boldsymbol{q}}_W + \boldsymbol{D}_G \, \dot{\boldsymbol{q}}_W + \boldsymbol{C}_G \, \boldsymbol{q}_W - \boldsymbol{f}_G = \boldsymbol{0} \quad . \tag{3.20}$$

3.2.5 Differential equations of rotor motion

Based on the Equations (3.7), (3.10), (3.13), (3.15) and (3.20 the whole differential equations of rotor motion can be summarized to

$$\begin{aligned} &(\boldsymbol{M}_T + \boldsymbol{M}_G)\, \ddot{\boldsymbol{q}}_W + (\boldsymbol{D}_T + \boldsymbol{D}_G + \boldsymbol{D}_a + \boldsymbol{D}_i)\, \dot{\boldsymbol{q}}_W + (\boldsymbol{C}_T + \boldsymbol{C}_G + \boldsymbol{C}_a + \boldsymbol{C}_W)\, \boldsymbol{q}_W \\ &\qquad = \boldsymbol{p}_T + \boldsymbol{p}_a + \boldsymbol{p}_g \quad . \end{aligned} \tag{3.21}$$

Torsion due to reaction forces in bearings

According to the reaction forces in the bearings in the Equations (3.6) and (3.9), the torsion T_ϵ in the centre of gravitation S_n of each disk is generated by the acting forces in the centre of each shaft W_n, hence

$$\begin{aligned} T_\epsilon = \sum_{n=1}^{N_d} &-\epsilon_n \left(\sin\phi_n \, \vec{e}_\eta + \cos\phi_n \, \vec{e}_\zeta \right) \\ &\times \left[\left(f_{i_{(4n-2)}} + f_{c_{(4n-2)}} \right) \vec{e}_\eta + \left(f_{i_{(4n-3)}} + f_{c_{(4n-3)}} \right) \vec{e}_\zeta \right] \quad . \end{aligned} \tag{3.22}$$

Furthermore, because the reaction forces of bending shaft do not act in the direction of shaft bending, the torque T_s will be brought forward from the shaft to the disks, thus

$$\begin{aligned} T_s = -\sum_{n=1}^{N_d} &\left(q_{4n-2} \, \vec{e}_\eta + q_{4n-3} \, \vec{e}_\zeta \right) \\ &\times \left[\left(f_{i_{(4n-2)}} + f_{c_{(4n-2)}} \right) \vec{e}_\eta + \left(f_{i_{(4n-3)}} + f_{c_{(4n-3)}} \right) \vec{e}_\zeta \right] \quad . \end{aligned} \tag{3.23}$$

Applying the driving torque T_a, T_ϵ and T_s into the dynamic equation in rotational x-direction, the differential equations of motion of the rotor with polar moments of inertia can be determined to

$$-\sum_{n=1}^{N_d} \Theta_{p_n} \ddot{\varphi}\, \vec{e}_x = -T_\epsilon - T_s - T_a \quad . \tag{3.24}$$

3.3 Dynamic parameters of anisotropic rotor supported by anisotropic flexible bearings

3.3.1 Flexibility matrix of shaft

Similar to the case in Section 3.2 and based on the equations in Section 2.6.1, the shaft bending forces in rotating reference frame for a general anisotropic rotor supported by anisotropic flexible bearings can be determined as follows

$$\begin{bmatrix} f_{c_1} \\ f_{c_2} \\ \vdots \\ f_{c_{(4N_d)}} \end{bmatrix} = - \begin{bmatrix} c_{11} & c_{12} & \cdots & c_{1(4N_d} \\ & c_{22} & \cdots & c_{2(4N_d)} \\ symm & & \ddots & \vdots \\ & & & c_{(4N_d)(4N_d)} \end{bmatrix} \begin{bmatrix} q_1 - q_{1L} \\ q_2 - q_{2L} \\ \vdots \\ q_{(4N_d)} - q_{(4N_d)L} \end{bmatrix} \tag{3.25}$$

Based on the Equations (2.82)-(2.85), the kinematic relationships in rotating reference frame for translational and rotational displacements and velocities of the bearings for the case of an anisotropic rotor with multiple disks can be obtained as follows:

for $n = 1, 2, \ldots, N_d$

$$q_{(4n-3)L} = \frac{1}{\ell} \sum_{k=n+1}^{N_e} \ell_k\, q_{(4N_d+1)} + \frac{1}{\ell} \sum_{k=1}^{n} \ell_k\, q_{(4N_d+3)} \tag{3.26}$$

$$q_{(4n-2)L} = \frac{1}{\ell} \sum_{k=n+1}^{N_e} \ell_k\, q_{(4N_d+2)} + \frac{1}{\ell} \sum_{k=1}^{n} \ell_k\, q_{(4N_d+4)} \tag{3.27}$$

$$q_{(4n-1)L} = \frac{1}{\ell} \left[q_{4N_d+1} - q_{4N_d+3} \right] \tag{3.28}$$

$$q_{(4n)L} = \frac{1}{\ell} \left[q_{4N_d+2} - q_{4N_d+4} \right] \quad . \tag{3.29}$$

The translational and rotational velocity of the bearings are obtained by derivation of the Equations (3.26) - (3.29) with time, hence for $n = 1$, 2, ..., N_d

$$\dot{q}_{(4n-3)L} = \frac{1}{\ell} \sum_{k=n+1}^{N_e} \ell_k \, \dot{q}_{(4N_d+1)} + \frac{1}{\ell} \sum_{k=1}^{n} \ell_k \, \dot{q}_{(4N_d+3)} \tag{3.30}$$

$$\dot{q}_{(4n-2)L} = \frac{1}{\ell} \sum_{k=n+1}^{N_e} \ell_k \, \dot{q}_{(4N_d+2)} + \frac{1}{\ell} \sum_{k=1}^{n} \ell_k \, \dot{q}_{(4N_d+4)} \tag{3.31}$$

$$\dot{q}_{(4n-1)L} = \frac{1}{\ell} \left[\dot{q}_{4N_d+1} - \dot{q}_{4N_d+3} \right] \tag{3.32}$$

$$\dot{q}_{(4n)L} = \frac{1}{\ell} \left[\dot{q}_{4N_d+2} - \dot{q}_{4N_d+4} \right] \quad . \tag{3.33}$$

Furthermore, the Equation (3.25) can be written as

$$\begin{bmatrix} f_{c_1} \\ f_{c_2} \\ \vdots \\ f_{c_{(4N_d)}} \end{bmatrix} = - \begin{bmatrix} c_{11} & c_{12} & \cdots & c_{1(4N_d)} \\ & c_{22} & \cdots & c_{2(4N_d)} \\ symm & & \ddots & \vdots \\ & & & c_{(4N_d)(4N_d)} \end{bmatrix} \begin{bmatrix} q_1 \\ q_2 \\ \vdots \\ q_{(4N_d)} \end{bmatrix}$$

$$+ \begin{bmatrix} c_{1\,(4N_d+1)} & c_{1\,(4N_d+2)} & c_{1\,(4N_d+3)} & c_{1\,(4N_d+4)} \\ c_{2\,(4N_d+1)} & c_{2\,(4N_d+2)} & c_{2\,(4N_d+3)} & c_{2\,(4N_d+4)} \\ \vdots & \vdots & \vdots & \vdots \\ c_{(4N_d)(4N_d+1)} & c_{(4N_d)(4N_d+2)} & c_{(4N_d)(4N_d+3)} & c_{(4N_d)(4N_d+4)} \end{bmatrix} \begin{bmatrix} q_{(4N_d+1)} \\ q_{(4N_d+2)} \\ q_{(4N_d+3)} \\ q_{(4N_d+4)} \end{bmatrix} \quad , \tag{3.34}$$

where for $j = 1, 2, \ldots, 4N_d$

$$c_{(j)(4N_d+1)} = \frac{1}{\ell} \sum_{n=1}^{N_d} \left[c_{(j)(4n)} + \sum_{k=n+1}^{N_e} \left(\ell_k \, c_{(j)(4n-3)} \right) \right]$$

$$c_{(j)(4N_d+2)} = \frac{1}{\ell} \sum_{n=1}^{N_d} \left[-c_{(j)(4n-1)} + \sum_{k=n+1}^{N_e} \left(\ell_k \, c_{(j)(4n-2)} \right) \right]$$

$$c_{(j)(4N_d+3)} = \frac{1}{\ell} \sum_{n=1}^{N_d} \left[-c_{(j)(4n)} + \sum_{k=1}^{n} \left(\ell_k \, c_{(j)(4n-3)} \right) \right]$$

$$c_{(j)(4N_d+4)} = \frac{1}{\ell} \sum_{n=1}^{N_d} \left[c_{(j)(4n-1)} + \sum_{k=1}^{n} \left(\ell_k \, c_{(j)(4n-2)} \right) \right] \quad . \tag{3.35}$$

In simple form the Equation (3.34) can be written as

$$\boldsymbol{f}_c = -\boldsymbol{C}_W \, \boldsymbol{q}_W + \boldsymbol{C}_{W_L} \, \boldsymbol{q}_L \quad . \tag{3.36}$$

3.3.2 Damping matrix of shaft

Similar to the formulation of the shaft bending forces in Section 3.3.1, the internal damping forces of the shaft in rotating reference frame can be formulated as

$$\begin{bmatrix} f_{i_1} \\ f_{i_2} \\ \vdots \\ f_{i_{(4N_d)}} \end{bmatrix} = - \begin{bmatrix} d_{11} & d_{12} & \cdots & d_{1(4N_d)} \\ & d_{22} & \cdots & d_{2(4N_d)} \\ symm & & \ddots & \vdots \\ & & & d_{(4N_d)(4N_d)} \end{bmatrix} \begin{bmatrix} \dot{q}_1 - \dot{q}_{1L} \\ \dot{q}_2 - \dot{q}_{2L} \\ \vdots \\ \dot{q}_{(4N_d)} - \dot{q}_{(4N_d)L} \end{bmatrix} \quad . \tag{3.37}$$

Furthermore, the Equation (3.37) can be rearranged to become

$$\begin{aligned} \begin{bmatrix} f_{i_1} \\ f_{i_2} \\ \vdots \\ f_{i_{(4N_d)}} \end{bmatrix} = & - \begin{bmatrix} d_{11} & d_{12} & \cdots & d_{1(4N_d)} \\ & d_{22} & \cdots & d_{2(4N_d)} \\ symm & & \ddots & \vdots \\ & & & d_{(4N_d)(4N_d)} \end{bmatrix} \begin{bmatrix} \dot{q}_1 \\ \dot{q}_2 \\ \vdots \\ \dot{q}_{(4N_d)} \end{bmatrix} \\ & + \begin{bmatrix} d_{(1)(4N_d+1)} & d_{(1)(4N_d+2)} & d_{(1)(4N_d+3)} & d_{(1)(4N_d+4)} \\ d_{(2)(4N_d+1)} & d_{(2)(4N_d+2)} & d_{(2)(4N_d+3)} & d_{(2)(4N_d+4)} \\ \vdots & \vdots & \vdots & \vdots \\ d_{(4N_d)(4N_d+1)} & d_{(4N_d)(4N_d+2)} & d_{(4N)(4N_d+3)} & d_{(4N_d)(4N_d+4)} \end{bmatrix} \begin{bmatrix} \dot{q}_{(4N_d+1)} \\ \dot{q}_{(4N_d+2)} \\ \dot{q}_{(4N_d+3)} \\ \dot{q}_{(4N_d+4)} \end{bmatrix} \quad , \end{aligned} \tag{3.38}$$

where for $j = 1, 2, \ldots, 4N_d$

$$\begin{aligned} d_{(j)(4N_d+1)} &= \frac{1}{\ell} \sum_{n=1}^{N_d} \left[d_{(j)(4n)} + \sum_{k=n+1}^{N_e} \left(\ell_k \, d_{(j)(4n-3)} \right) \right] \\ d_{(j)(4N_d+2)} &= \frac{1}{\ell} \sum_{n=1}^{N_d} \left[-d_{(j)(4n-1)} + \sum_{k=n+1}^{N_e} \left(\ell_k \, d_{(j)(4n-2)} \right) \right] \\ d_{(j)(4N_d+3)} &= \frac{1}{\ell} \sum_{n=1}^{N_d} \left[-d_{(j)(4n)} + \sum_{k=1}^{n} \left(\ell_k \, d_{(j)(4n-3)} \right) \right] \\ d_{(j)(4N_d+4)} &= \frac{1}{\ell} \sum_{n=1}^{N_d} \left[d_{(j)(4n-1)} + \sum_{k=1}^{n} \left(\ell_k \, d_{(j)(4n-2)} \right) \right] \end{aligned} \tag{3.39}$$

or in simple form the Equation (3.38) can be written as

$$\boldsymbol{f}_i = -\boldsymbol{D}_i \, \dot{\boldsymbol{q}}_W + \boldsymbol{D}_{i_L} \, \boldsymbol{q}_L \quad . \tag{3.40}$$

Because the external damping forces are formulated by proportional damping corresponding to the absolute velocity of disk, there is no difference between the formulation of the anisotropic rotor supported by anisotropic flexible bearings and the anisotropic rotor supported by rigid bearings as derived in Equation (3.12).

3.3.3 Reaction forces at the shaft ends

The reaction forces at the shaft ends for anisotropic rotor with one disk have been considered in Section 2.6.1. In order to derive the reaction forces for a rotor with multiple disks, the same way as the formulation in Equations (2.94)-(2.98) can be used, because the bearing models of the rotor with one disk in Section 2.6.1 and the rotor with multiple disks are the same. In both rotors, the anisotropic bearings in the whole system have four degrees of freedom (i.e. two degrees of freedom at each shaft end). Therefore, the Equation (2.99) can be used again.

$$\boldsymbol{f}_{L_W} = \boldsymbol{D}_{i_L}^T \,\dot{\boldsymbol{q}}_W - \boldsymbol{D}_{L_L}\,\dot{\boldsymbol{q}}_L + \boldsymbol{C}_{W_L}^T\,\boldsymbol{q}_W - \boldsymbol{C}_{L_L}\,\boldsymbol{q}_L \quad . \tag{3.41}$$

Furthermore, the matrix components of $\boldsymbol{D}_{L_L}$ and $\boldsymbol{C}_{L_L}$ are obtained as follows

$$\boldsymbol{D}_{L_L} = \begin{bmatrix} d_{L_L(4N_d+1)(4N_d+1)} & d_{L_L(4N_d+1)(4N_d+2)} & d_{L_L(4N_d+1)(4N_d+3)} & d_{L_L(4N_d+1)(4N_d+4)} \\ d_{L_L(4N_d+2)(4N_d+1)} & d_{L_L(4N_d+2)(4N_d+2)} & d_{L_L(4N_d+2)(4N_d+3)} & d_{L_L(4N_d+2)(4N_d+4)} \\ d_{L_L(4N_d+3)(4N_d+1)} & d_{L_L(4N_d+3)(4N_d+2)} & d_{L_L(4N_d+3)(4N_d+3)} & d_{L_L(4N_d+3)(4N_d+4)} \\ d_{L_L(4N_d+4)(4N_d+1)} & d_{L_L(4N_d+4)(4N_d+2)} & d_{L_L(4N_d+4)(4N_d+3)} & d_{L_L(4N_d+4)(4N_d+4)} \end{bmatrix} , \tag{3.42}$$

where for $j = 1, 2, 3, 4$

$$\begin{aligned} d_{L_L(4N_d+1)(4N_d+j)} &= \frac{1}{\ell} \sum_{n=1}^{N_d} \left[d_{(4n)(4N_d+j)} + \sum_{k=n+1}^{N_e} \left(\ell_k \, d_{(4n-3)(4N_d+j)} \right) \right] \\ d_{L_L(4N_d+2)(4N_d+j)} &= \frac{1}{\ell} \sum_{n=1}^{N_d} \left[-d_{(4n-1)(4N_d+j)} + \sum_{k=n+1}^{N_e} \left(\ell_k \, d_{(4n-2)(4N_d+j)} \right) \right] \\ d_{L_L(4N_d+3)(4N_d+j)} &= \frac{1}{\ell} \sum_{n=1}^{N_d} \left[-d_{(4n)(4N_d+j)} + \sum_{k=1}^{n} \left(\ell_k \, d_{(4n-3)(4N_d+j)} \right) \right] \\ d_{L_L(4N_d+4)(4N_d+j)} &= \frac{1}{\ell} \sum_{n=1}^{N_d} \left[d_{(4n-1)(4N_d+j)} + \sum_{k=1}^{n} \left(\ell_k \, d_{(4n-2)(4N_d+j)} \right) \right] \end{aligned} \tag{3.43}$$

and

$$\boldsymbol{C}_{L_L} = \begin{bmatrix} c_{L_L(4N_d+1)(4N_d+1)} & c_{L_L(4N_d+1)(4N_d+2)} & c_{L_L(4N_d+1)(4N_d+3)} & c_{L_L(4N_d+1)(4N_d+4)} \\ c_{L_L(4N_d+2)(4N_d+1)} & c_{L_L(4N_d+2)(4N_d+2)} & c_{L_L(4N_d+2)(4N_d+3)} & c_{L_L(4N_d+2)(4N_d+4)} \\ c_{L_L(4N_d+3)(4N_d+1)} & c_{L_L(4N_d+3)(4N_d+2)} & c_{L_L(4N_d+3)(4N_d+3)} & c_{L_L(4N_d+3)(4N_d+4)} \\ c_{L_L(4N_d+4)(4N_d+1)} & c_{L_L(4N_d+4)(4N_d+2)} & c_{L_L(4N_d+4)(4N_d+3)} & c_{L_L(4N_d+4)(4N_d+4)} \end{bmatrix} , \tag{3.44}$$

where for $j = 1, 2, 3, 4$

$$\begin{aligned} c_{L_L(4N_d+1)(4N_d+j)} &= \frac{1}{\ell} \sum_{n=1}^{N_d} \left[c_{(4n)(4N_d+j)} + \sum_{k=n+1}^{N_e} \left(\ell_k \, c_{(4n-3)(4N_d+j)} \right) \right] \\ c_{L_L(4N_d+2)(4N_d+j)} &= \frac{1}{\ell} \sum_{n=1}^{N_d} \left[-c_{(4n-1)(4N_d+j)} + \sum_{k=n+1}^{N_e} \left(\ell_k \, c_{(4n-2)(4N_d+j)} \right) \right] \end{aligned}$$

$$c_{L_L(4N_d+3)(4N_d+j)} = \frac{1}{\ell}\sum_{n=1}^{N_d}\left[-c_{(4n)(4N_d+j)} + \sum_{k=1}^{n}\left(\ell_k\, c_{(4n-3)(4N_d+j)}\right)\right]$$

$$c_{L_L(4N_d+4)(4N_d+j)} = \frac{1}{\ell}\sum_{n=1}^{N_d}\left[c_{(4n-1)(4N_d+j)} + \sum_{k=1}^{n}\left(\ell_k\, c_{(4n-2)(4N_d+j)}\right)\right] \quad . \tag{3.45}$$

Furthermore, the equations in the bearing system can be considered based on the Equation (2.110) by inserting the Equations (3.41), (2.106) and (2.109), thus

$$\boldsymbol{M}_L\,\ddot{\boldsymbol{q}}_L = \boldsymbol{D}_{i_L}^T\,\dot{\boldsymbol{q}}_W - \left(\boldsymbol{D}_{L_L} + \boldsymbol{D}_{d_L}\right)\dot{\boldsymbol{q}}_L + \boldsymbol{C}_{W_L}^T\,\boldsymbol{q}_W - \left(\boldsymbol{C}_{L_L} + \boldsymbol{C}_{d_L} + \boldsymbol{C}_L\right)\boldsymbol{q}_L \tag{3.46}$$

3.3.4 Differential equations of rotor motion

The whole differential equations of motion of the rotor-bearing system can be arranged by reformulation the Equation (3.21) together with the Equation (3.46) in matrix notation as follows

$$\left[\begin{array}{c|c} \boldsymbol{M}_T + \boldsymbol{M}_G & \boldsymbol{0} \\ \hline \boldsymbol{0} & \boldsymbol{M}_L \end{array}\right]\begin{bmatrix} \ddot{\boldsymbol{q}}_W \\ \ddot{\boldsymbol{q}}_L \end{bmatrix} + \left[\begin{array}{c|c} \boldsymbol{D}_T + \boldsymbol{D}_G + \boldsymbol{D}_a + \boldsymbol{D}_i & -\boldsymbol{D}_{i_L} \\ \hline -\boldsymbol{D}_{i_L}^T & \boldsymbol{D}_{L_L} + \boldsymbol{D}_{d_L} \end{array}\right]\begin{bmatrix} \dot{\boldsymbol{q}}_W \\ \dot{\boldsymbol{q}}_L \end{bmatrix}$$

$$+ \left[\begin{array}{c|c} \boldsymbol{C}_T + \boldsymbol{C}_G + \boldsymbol{C}_a + \boldsymbol{C}_W & -\boldsymbol{C}_{W_L} \\ \hline -\boldsymbol{C}_{W_L}^T & \boldsymbol{C}_{L_L} + \boldsymbol{C}_{d_L} + \boldsymbol{C}_L \end{array}\right]\begin{bmatrix} \boldsymbol{q}_W \\ \boldsymbol{q}_L \end{bmatrix} = \begin{bmatrix} \boldsymbol{p}_T + \boldsymbol{p}_a + \boldsymbol{p}_g \\ \boldsymbol{0} \end{bmatrix} . \tag{3.47}$$

In general form the Equation (3.47) can be written as

$$\boldsymbol{M}\,\ddot{\boldsymbol{q}} + \boldsymbol{D}\,\dot{\boldsymbol{q}} + \boldsymbol{C}\,\boldsymbol{q} = \boldsymbol{p} \quad . \tag{3.48}$$

In numerical simulation, usually the mass of bearings in sub matrix $\boldsymbol{M}_L$ in Equation (3.47) is assumed to be zero. Here, the method of static condensation can be applied in order to reduce the degree of freedom of the system.

Similar to the case of the rotor supported by rigid bearings as presented in Section 3.2.5, the Equation (3.24) for the torsion due to reaction forces in bearings can be used again.

3.4 Case study: anisotropic rotor with two disks supported by rigid bearings

In this section, several anisotropic rotor models with two disks supported by rigid or anisotropic flexible bearings are investigated. Based on these models, stability charts will be presented. The additionally case of a twisted anisotropic shaft with two disks is also studied. In this case, the influence of the number of elements in the shaft modelling is studied.

3.4.1 Rotor model

An anisotropic shaft with two disks as shown in Figure 3.2 is supported by rigid bearings. The shaft is assumed as a massless, but has different orientations along the shaft. If the minimal number approach of discrete elements is used in the model, the shaft will have three elements because two disks are attached on the shaft and each disk must be placed in a node. The two identical disks are thin and rigid and have a ratio of mass moment of inertia $\Theta_{p_1}/\Theta_{a_1} = \Theta_{p_2}/\Theta_{a_2} = 1.98$ (i.e. disk radius = 0.06 m, disk thickness = 0.01 m). The first disk is placed with the distance ℓ_1 from the left shaft end and the second disk ℓ_3 from the right shaft end. In order to simplify the shaft anisotropy, a rectangular cross section of each element is used. The shaft anisotropy is varied from 0 to 0.99. In the whole system, the internal and external damping is neglected.

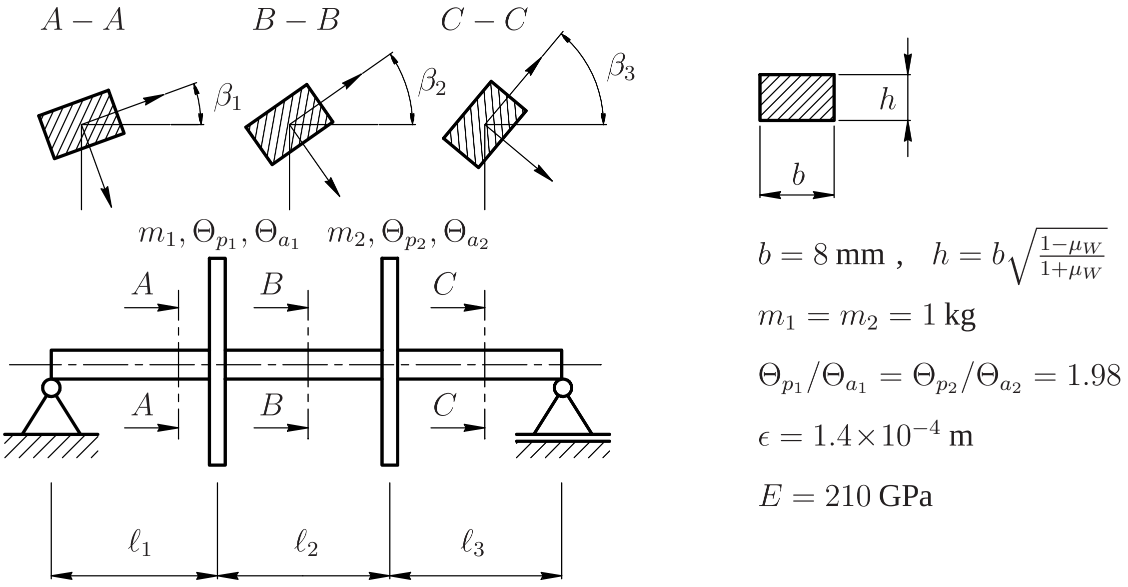

Figure 3.2: Model of anisotropic rotor with two disks supported by rigid bearings

Furthermore, six examples of anisotropic rotors based on the model in Figure 3.2 with varying orientations are calculated numerically. The parameters of these models are listed in Table (3.1). All models have the same length of shaft elements ($\ell_1 = \ell_2 = \ell_3 = 0.1\,\text{m}$). Therefore, the first disk is attached $0.1\,\text{m}$ from the left shaft end, whereas the second disk is placed at the distance $0.1\,\text{m}$ from the right shaft end. At this position of the disks the gyroscopic moments must have significant effects on the rotor. Corresponding to the shaft bending mode of U-form or S-form, the angular positions of the disks are not equal to zero.

In the six rotor models, the investigation is limited to study of the effects of different orientations of shaft elements. In Model 5, a purely anisotropic rotor with two disks is investigated. In Models 6, 7 and 8, the effect of different orientations on the shaft is compared. The difference $\Delta\beta$ in the shaft orientation (i.e. the difference in orientation between both shaft ends) is varied to $30°$, $60°$

and 120°. In these models, the orientation of elements is distributed linearly. Furthermore, as represented in Models 9 and 10, the effect of an arbitrary distribution of the shaft orientations is studied.

Table 3.1: Parameter of rotor cases

Model	$\ell_1 = \ell_2 = \ell_3$ [m]	β_1 [°]	β_2 [°]	β_3 [°]	Chart
5	0.10	0	0	0	Figure 3.3a
6	0.10	0	15	30	Figure 3.3b
7	0.10	0	30	60	Figure 3.3c
8	0.10	0	60	120	Figure 3.3d
9	0.10	0	60	30	Figure 3.3e
10	0.10	0	30	0	Figure 3.3f

3.4.2 Stability analysis

As investigated in Section 2.10.1, the stability of the rotor supported by rigid bearings is determined easily through the analysis of the eigenvalues according to Equation (2.125). In this section, the stability of the six rotor models above are presented in Figure 3.3.

In Figure 3.3a, the stability chart of the purely anisotropic rotor with two disks as described by Model 5 is depicted. Generally, the instability area (shown in grey) has two regions especially for a rotor for which the coefficient of element anisotropy is $\mu_W < 0.85$. For a rotor with a higher value of the element anisotropy, the two instability regions combine to a single area with a very wide range of instability. The system possesses eight natural frequencies. These natural frequencies are obtained from the forward whirl speeds of the rotor in Section 2.10.1. In the figures, the natural frequencies which are considered at rotational speed $\Omega = 0$ are plotted for rotor with various coefficients of element anisotropy. The first region of instability is termed as the instability area 1 and the second region instability as the instability area 3. Comparing the instability area of the purely anisotropic rotor with one disk as described in Model 1 and presented in Figure 2.16a to the purely anisotropic rotor with two disks in Model 5 as presented in Figure 3.3a, the rotor in Model 1 has only one region of instability and lies exactly between the first and the second natural frequencies (ω_1 and ω_2). As represented for Model 5, because of the effect of gyroscopic moments in the rotor the first instability area is not exactly between the first and the second natural frequencies but shifted to a higher frequency. Generally, the first instability area is shifted about $3.72\,\%$ and the instability area 3 is shifted about $10.73\,\%$ to higher frequencies (see Tables C.1, C.2 and C.3 in Appendix C). The rate of the shifted frequency depends on the parameters of gyroscopic moments in a system.

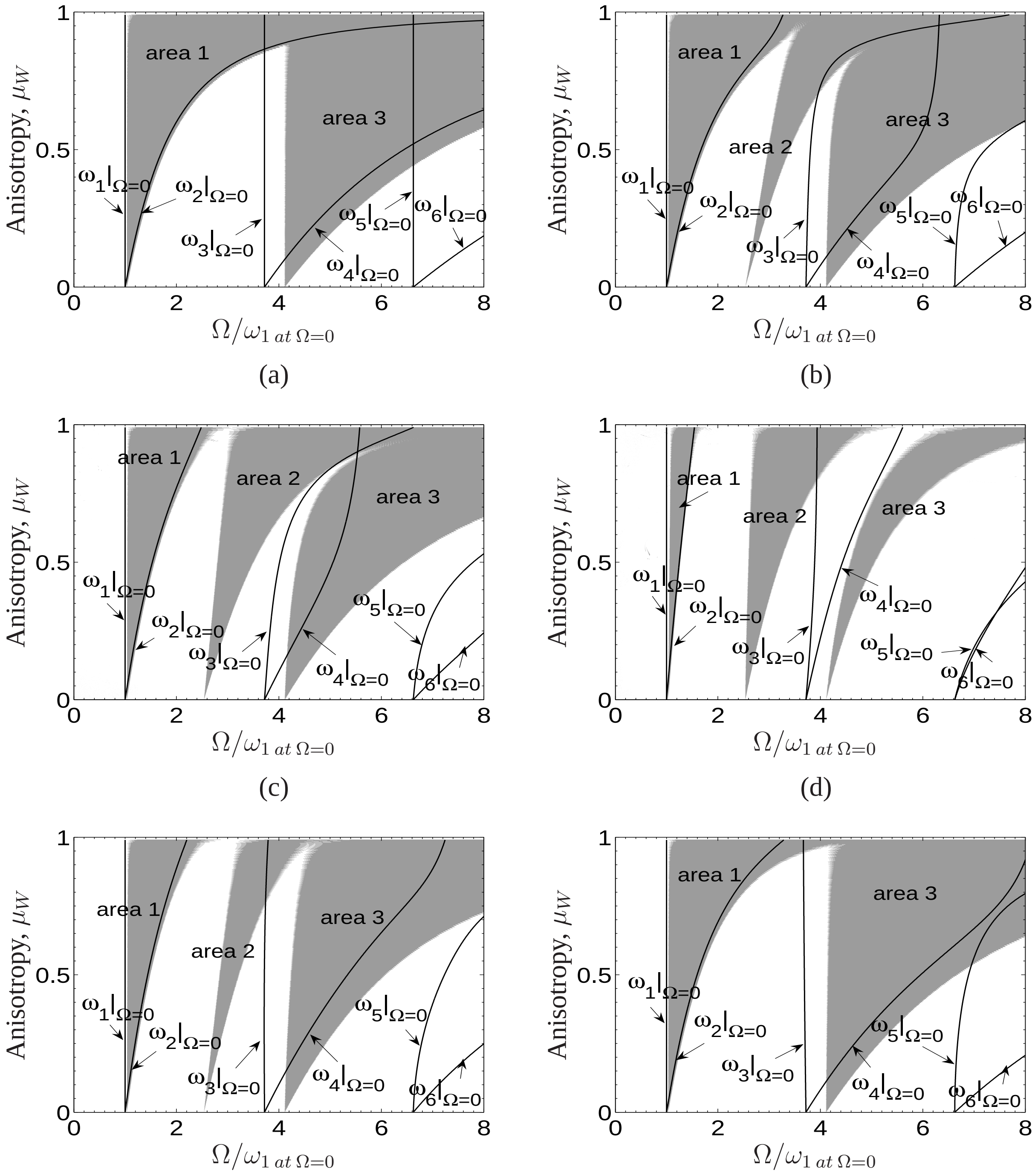

(a) (b)

(c) (d)

(e) (f)

Figure 3.3: Stability charts of undamped anisotropic rotor cases with two disks and three shaft elements: (a) Model 5 ($\beta_1 = \beta_2 = \beta_3 = 0°$), (b) Model 6 ($\beta_1 = 0°, \beta_2 = 15°, \beta_3 = 30°$), (c) Model 7 ($\beta_1 = 0°, \beta_2 = 30°, \beta_3 = 60°$), (d) Model 8 ($\beta_1 = 0°, \beta_2 = 60°, \beta_3 = 120°$), (e) Model 9 ($\beta_1 = 0°, \beta_2 = 60°, \beta_3 = 30°$) and (f) Model 10 ($\beta_1 = 0°, \beta_2 = 30°, \beta_3 = 0°$). The natural frequencies of the rotor are obtained at rotational speed $\Omega = 0$ (shown only six of eight natural frequencies). The areas of instability are indicated by a shaded area

A detailed investigation of the purely anisotropic rotor as described by Model 5 is presented in Figure 3.4 especially for the rotor with the coefficient of element anisotropy at $\mu_W = 0.3$. In the figure, the whirl speeds of the rotor are analyzed in fixed reference frame and have been normalized due to the first natural frequency ω_1 which is obtained at the rotational speed $\Omega = 0$. According to Equation (2.125), the matrices have the size of $16{\times}16$. The solution of this equation gives 16 eigenvalues which consist of eight complex conjugate pairs. As mentioned in Section 2.10.1, the imaginary part corresponds to the whirl speeds as plotted in Figure 3.4a and the real parts to the decay rate as depicted in Figure 3.4b. In case of the rotating rotor at a frequency about 1.04 - 1.41 and about 4.12 - 5.61, the first whirl speeds of both forward and backward whirl speeds (ω_1' and $\bar{\omega}_1'$) have the same values and coincide with the Ω-line. According to the decay rate plot in Figure 3.4b, there are two of 16 eigenvalues in which the real parts are not zero. These real parts have positive and negative values.

In Figure 3.3b, c, d and f, the stability charts of the cases of anisotropic rotors with two disks and different shaft orientations are presented. Special for Figures 3.3b, 3.3c and 3.3d, the differences of element orientations are distributed linearly along the shafts as listed for Model 6, 7 and 8 in Table 3.1. The difference in the shaft orientation in the rotor in Model 7 with $\Delta\beta = 60°$ is twice as big as for the rotor in Model 6 with $\Delta\beta = 30°$. Similarly, the orientation in the rotor in Model 8 is twice as big as for the one in Model 7.

In general, the stability charts of the anisotropic rotors in Models 6, 7 and 8 have a similar form. Each chart has three regions of instability. Comparing the Figure 3.3b, 3.3c and 3.3d to the Figure 3.3a, there is a new region of instability which occurs between the first and the third region. Here, the new instability region is termed as the instability area 2. In Model 7 (i.e. rotor with $\Delta\beta = 60°$), the width of the second instability area is wider than the one in Model 6. The largest width occurs if the difference of shaft orientation is $\Delta\beta = 90°$ with the distribution of orientation $\beta_1 = 0°$, $\beta_2 = 45°$ and $\beta_3 = 90°$ (not presented in the figure). For $\Delta\beta > 90°$ as presented in Model 8, the width of the second instability region becomes narrower as depicted in Figure 3.3d. Furthermore, the first instability area is shifted to higher frequencies. The higher the coefficient of element anisotropy in the rotor, the bigger is the shift of the instability area. It means the higher the coefficient of element anisotropy in the rotor, the wider is the first instability area. Besides, the bigger the difference $\Delta\beta$ in the shaft orientation, the higher is the shift of the lower boundary of instability corresponding to ω_1 but the lower is the shift of the upper boundary of instability due to ω_2. Generally, the difference in the shaft orientation decreases the width of the first instability area. In the third instability area, the shift of the lower and upper boundary of the instability area due to ω_3 and ω_4, respectively is higher than for the first instability area. These trends are confirmed by the corresponding values for the rotor with the coefficient of element anisotropy at $\mu_W = 0.2$, 0.3 and 0.5 and presented in Tables C.1, C.2 and C.3 in Appendix C, respectively.

Similar to Figure 3.4, a detailed investigation of the anisotropic rotor as described in Model 7 is presented in Figure 3.5 especially for the rotor with the coefficient of element anisotropy at

$\mu_W = 0.3$. In Figure 3.5a, it can be seen that in case the rotor rotates at a frequency about 1.04 - 1.32 and about 4.22 - 5.27 where these instability regions are denoted as area I and III, respectively, the first whirl speeds of both forward and backward whirl speeds (ω_1' and $\bar{\omega}_1'$) have the same value and coincide with the Ω-line. According to the decay rate plot in Figure 3.5b, there are also two of 16 eigenvalues in which the real parts are not zero. These real parts have positive and negative values. Besides, in case of the rotating rotor at frequency about 2.70 - 3.05 where the second region of instability is existing and denoted as region II, the first and the second backward whirl speeds coincide. As depicted in Figure 3.5b, there are two of 16 eigenvalues in which the real parts are not zero. These real parts have also positive and negative values. Therefore, this range is denoted as unstable region.

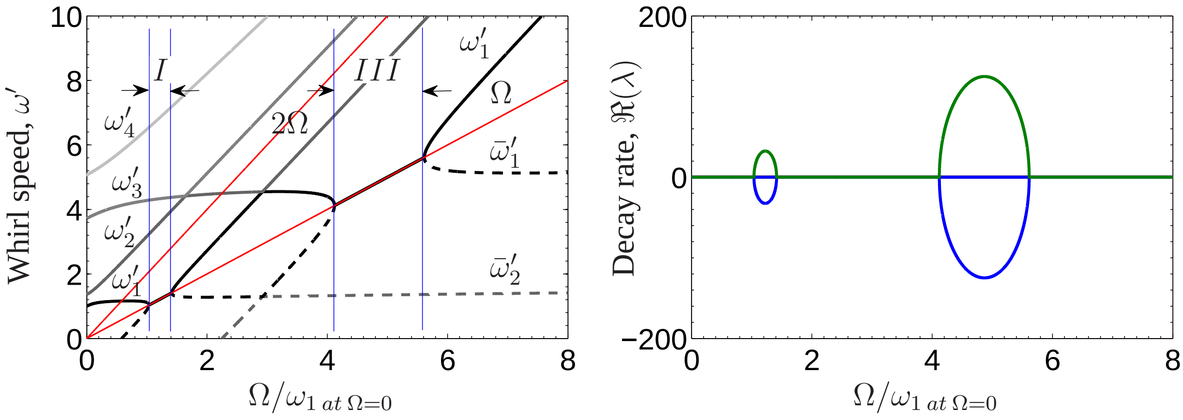

(a) (b)

Figure 3.4: (a) Non-dimensional CAMPBELL diagram (shown only four of eight forward whirl and two of eight backward whirl speeds) of the undamped anisotropic rotor with two disks in Model 5 ($\beta_1 = \beta_2 = \beta_3 = 0°$) with the coefficient of element anisotropy at $\mu_W = 0.3$ and (b) decay rate plot

In Model 9, the shaft element orientations of the anisotropic rotor with two disks is not distributed linearly. The difference in the shaft orientation between both shaft ends is $30°$ (as in Model 6), but the orientation of the second shaft element is $60°$. The model represents an anisotropic rotor with arbitrary orientations along the shaft. The stability chart is depicted in Figure 3.3e. Now, the form of the instability region in Model 9 is qualitatively similar to the instability region in Models 6, 7 or 8. The chart has three regions of instability. The first and the third regions of instability of Model 9 are narrower than the one in Model 6, the second region of instability is only slightly narrower than the one in Model 6.

In Model 10, the difference in orientation between both shaft ends is zero, but the orientation of the second shaft element is $30°$. The stability chart is shown in Figure 3.3f. Although the rotor has a nonvanishing orientation in the central section of the shaft (i.e. in the second shaft element), an instability occurs only in two regions similar to the case of purely anisotropic rotor in Model

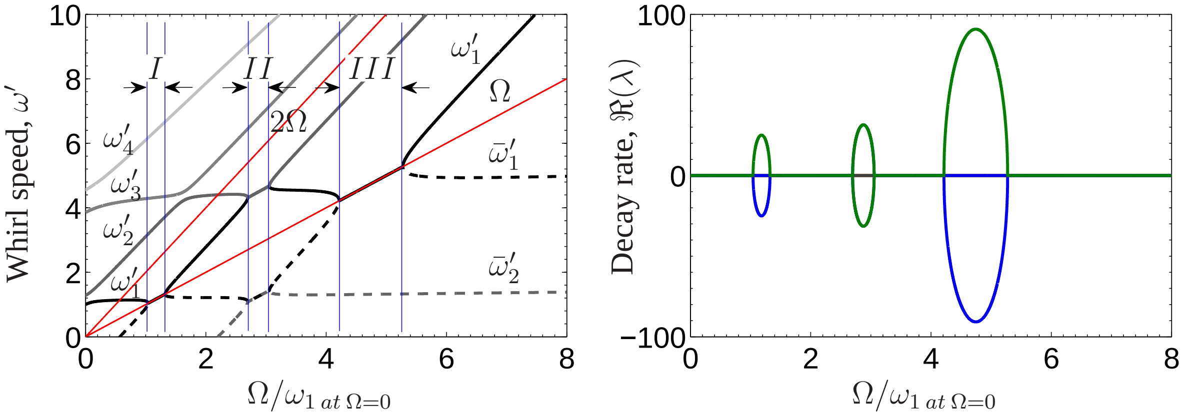

(a)

(b)

Figure 3.5: (a) Non-dimensional CAMPBELL diagram (shown only four of eight forward whirl and two of eight backward whirl speeds) of the undamped anisotropic rotor with two disks in Model 7 ($\beta_1 = 0°$, $\beta_2 = 30°$, $\beta_3 = 60°$) with the coefficient of element anisotropy at $\mu_W = 0.3$ and (b) decay rate plot

5. Comparing the instability area of the rotor in Model 10 as presented in Figure 3.3f to Model 5 in Figure 3.3a, the width of the instability range in Figure 3.3f is slightly narrower and the shift of the instability areas to higher frequencies is larger.

Based on the models presented in this section, it can be concluded that the difference in the shaft orientation affects the occurrence of the second region of instability. The bigger the difference between the actual shaft orientation and the maximum value $90°$, the wider is the range of the second instability region. The different shaft orientations cause a reduction of the width of instability in the case of an anisotropic rotor with one disk and two disks, too.

3.4.3 A twisted anisotropic shaft with two disks

In this section, the difference in the shaft orientation between both shaft ends of a twisted anisotropic shaft with two disks is assumed to be $60°$. By using the minimal number of elements and linearly distributed orientations along the shaft, the twisted anisotropic rotor is identical to Model 5 in Section 3.4.1 with the orientations $(0°$ - $30°$ - $60°)$ for the three shaft elements. The stability chart of this model was presented in Figure 3.3c. Whereas the rotor is discretized by 6 shaft elements, the linearly distributed orientations of the shaft elements become $(0°$ - $12°$ - $24°$ - $36°$ - $48°$ - $60°)$. For 24 elements, the orientations of elements are $(0°$ - $2.6°$ - $5.2°$ - $\cdots$ - $60°)$. The stability charts of the model with 6 and 24 elements are plotted in Figure 3.6.

The stability charts of the twisted anisotropic rotor with two disks show three instability regions. Detailed values for the rotor with the coefficient of element anisotropy at $\mu_W = 0.2$ and 0.3 are listed in Tables C.4 and C.5 in Appendix C. For example, based on the tables, the width of the first and the third instability regions increases until it reaches an asymptotic value at a large number of shaft elements as presented in Figures 3.7 to 3.9. The increase in the instability intervals is shown as a decrease in the lower boundary and increase in the upper boundary of instabilities for the rotor with a larger number of shaft elements. In contrary, the width of the second instability region decreases for larger number of elements and tends to small values as plotted in Figure 3.8.

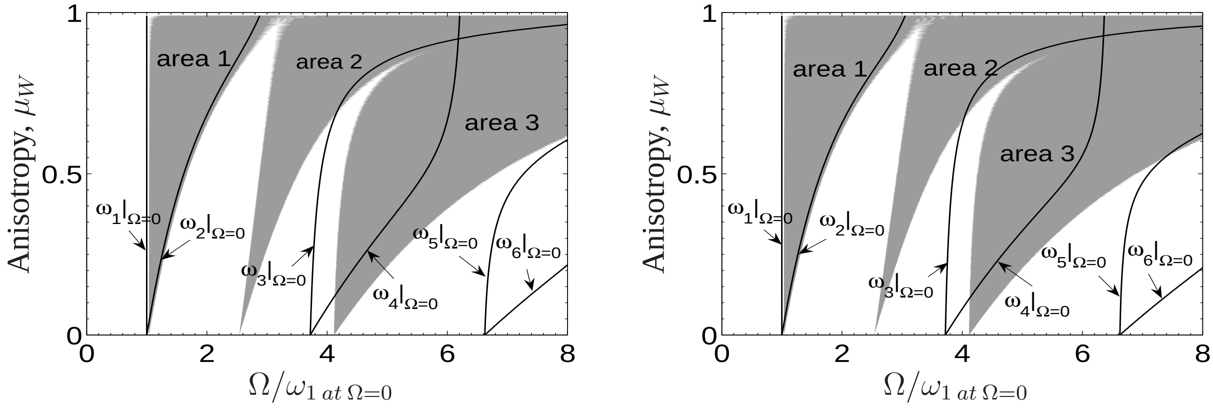

(a) (b)

Figure 3.6: Comparison of stability charts of undamped twisted anisotropic shaft with two disks and the difference $\Delta\beta = 60°$ in the shaft orientation supported by rigid bearings: (a) model with 6-elements and (b) 24-elements. The natural frequencies of the rotor are obtained at rotational speed $\Omega = 0$ (shown only six of eight natural frequencies)

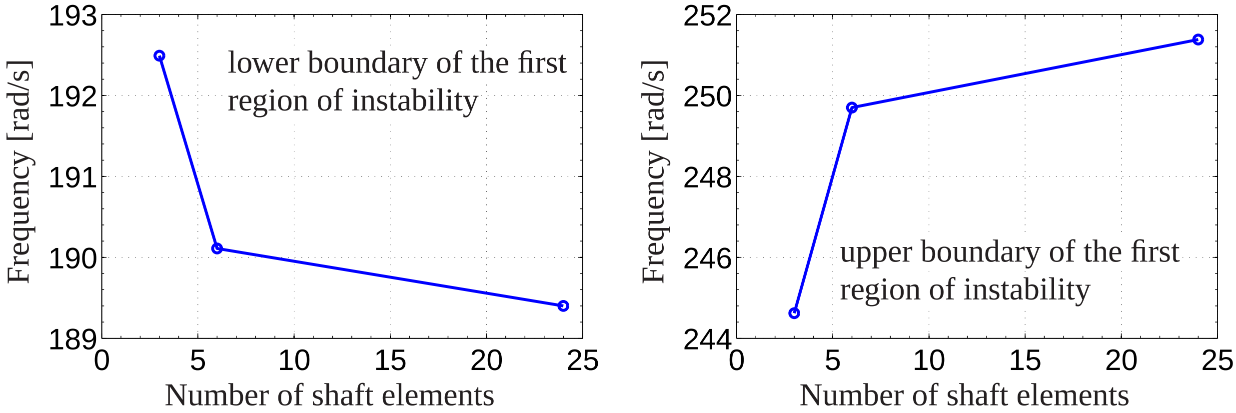

(a) (b)

Figure 3.7: Comparison of the lower and upper boundaries of the first instability region of undamped twisted anisotropic shaft with two disks supported by rigid bearings. The coefficient of element anisotropy at $\mu_W = 0.3$ for various number (3, 6 and 24) of the discrete shaft elements

In this research, the number of shaft elements of the rotor is limited to 24 elements. By using 24 shaft elements on the shaft, the investigation of the second instability region cannot be concluded yet. It needs a further investigation by using a higher number of shaft elements in order to proof whether the width of the second instability tends to zero or an asymptotic value. If the rotor shaft is discretized by a very large number of shaft elements the difference of the linearly distributed orientations of the shaft elements is very small.

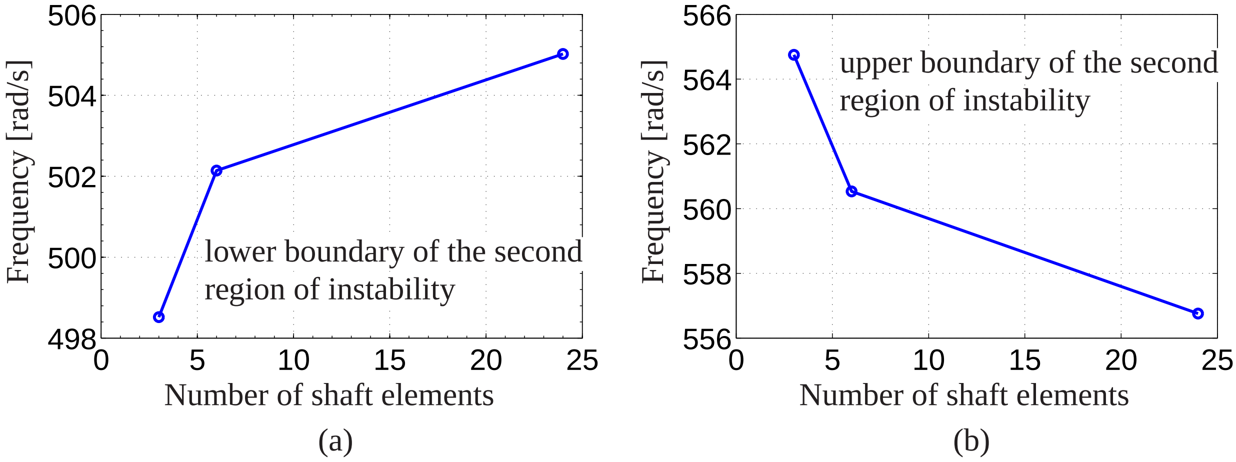

(a) (b)

Figure 3.8: Comparison of the lower and upper boundaries of the second instability region of undamped twisted anisotropic shaft with two disks supported by rigid bearings. The coefficient of element anisotropy at $\mu_W = 0.3$ for various number (3, 6 and 24) of the discrete shaft elements

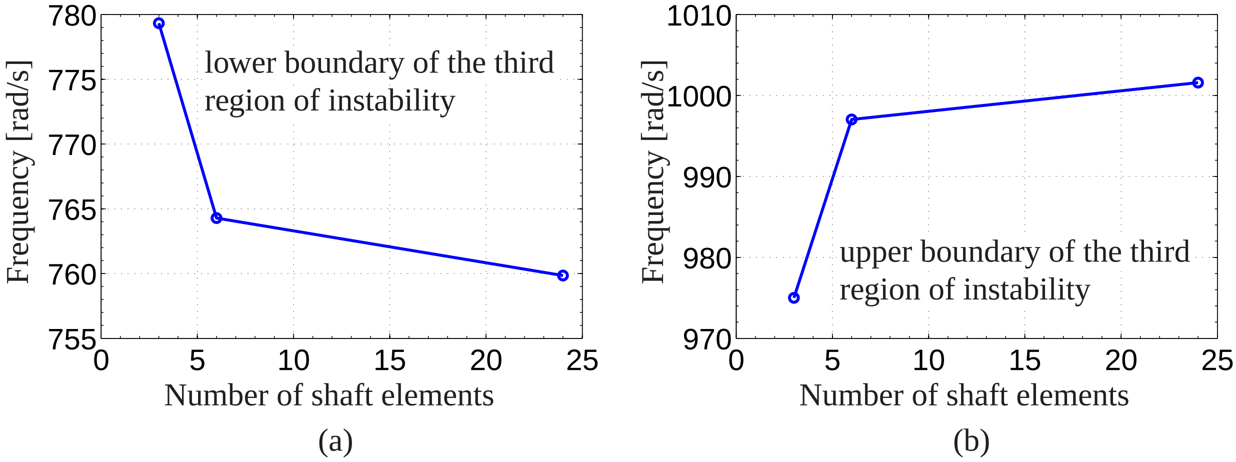

(a) (b)

Figure 3.9: Comparison of the lower and upper boundaries of the third instability region of undamped twisted anisotropic shaft with two disks supported by rigid bearings. The coefficient of element anisotropy at $\mu_W = 0.3$ for various number (3, 6 and 24) of the discrete shaft elements

Based on the Table C.5 in Appendix C, comparing the natural frequencies of the anisotropic rotor with various discretized number of shaft elements (i.e. the element anisotropy $\mu_W = 0.3$), while the first and the third natural frequency increase until they reach asymptotic values, the second and the fourth natural frequency decrease for anisotropic rotor with a larger number of shaft elements. In the tables, only four of the eight natural frequencies are listed. The change of the natural frequencies of the models as shown in Figures 3.10 are relative small (less than 5% for the model with 6 elements compared to the model with 3 elements and less than 2% for model with 24 elements compared to the model with 6 elements). Especially for the first and the second natural frequency, the change is less than 2% for the model with 6 elements compared to the model with 3 elements and less than 1% for model with 24 elements compared to the model with 6 elements.

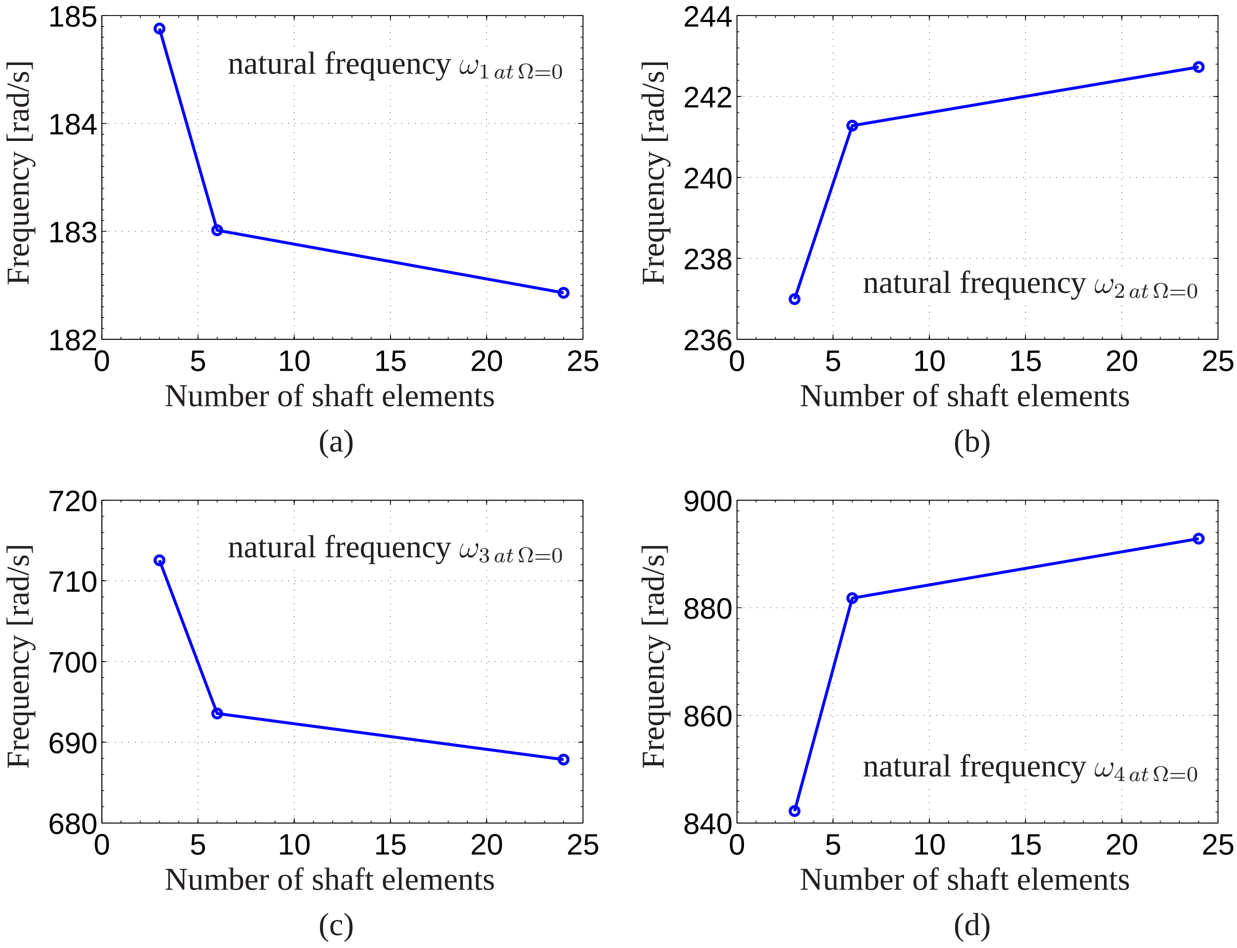

(a) (b)

(c) (d)

Figure 3.10: Comparison of the first four natural frequencies of undamped twisted anisotropic shaft with two disks supported by rigid bearings. The coefficient of element anisotropy at $\mu_W = 0.3$ for various number (3, 6 and 24) of the discrete shaft elements

3.5 Case study: anisotropic rotor with two disks supported by anisotropic flexible bearings

In this section, four cases of an anisotropic rotor with two disks supported by anisotropic flexible bearings are presented. The first two cases are purely anisotropic rotor and the others are anisotropic rotor with different shaft orientations. The stability charts of the models are determined by using the FLOQUET theory and the dynamic responses of the rotors are obtained by solving the differential equations of the forced vibration numerically.

3.5.1 Rotor model

As mentioned above, the first two models are purely anisotropic rotors supported by anisotropic flexible bearings as shown in Figure 3.11. The rotor shaft is discretized by three shaft elements without different orientations ($\beta_1 = \beta_2 = \beta_3 = 0°$) or $\Delta\beta = 0°$. The length of the shaft elements are the same ($\ell_1 = \ell_2 = \ell_3 = 0.1\,\mathrm{m}$). The two identical thin disks are attached on the shaft. Generally, the shaft model is similar to the case in Section 3.4.1. Further, the condition of bearings are identical to the case in Section 2.10.2. The anisotropy of the bearing stiffness is defined as presented in Equation (2.147), where c_{1z} and c_{1y} are the stiffness parameters of the bearings on the left shaft end in z-direction and y-direction, respectively, and c_{2z} and c_{2y} on the right shaft end. The bearing stiffness as in the z-direction are $c_{1z} = c_{2z} = 13\,763$ N/m. In this section, two different anisotropies of the bearing stiffness with $\mu_{L_1} = \mu_{L_2} = \mu_L = 0.3$ (i.e. $c_{1y} = c_{2y} = 7\,411$ N/m) and 0.6 (i.e. $c_{1y} = c_{2y} = 3\,441$ N/m) are simulated. The stability charts are obtained by using the FLOQUET theory and presented in Figure 3.12a and b. The areas of instability are indicated by a shaded area. In order to verify the stability charts, the dynamic responses in frequency domain of the rotor models with the coefficient of element anisotropy at $\mu_W = 0.3$ and 0.5 in both support conditions of the anisotropic flexible bearings are presented in Figure 3.12c, d, e and f. These models are forced vibration systems, in which the eccentricity of unbalance mass in each disk is $\epsilon = 1.4 \times 10^{-4}\,\mathrm{m}$. Besides, all internal and external dampings in the shaft and bearings are neglected.

Furthermore, the other two models are anisotropic rotor with different shaft orientations supported by anisotropic flexible bearings. The shaft orientations are chosen as $\beta_1 = 0°$, $\beta_2 = 30°$ and $\beta_3 = 60°$ or $\Delta\beta = 60°$, according to Figure 3.11. Other parameters are the same with the first two models above. The stability charts are presented in Figure 3.13a and b and the dynamic responses in frequency domain in Figure 3.13c, d, e and f.

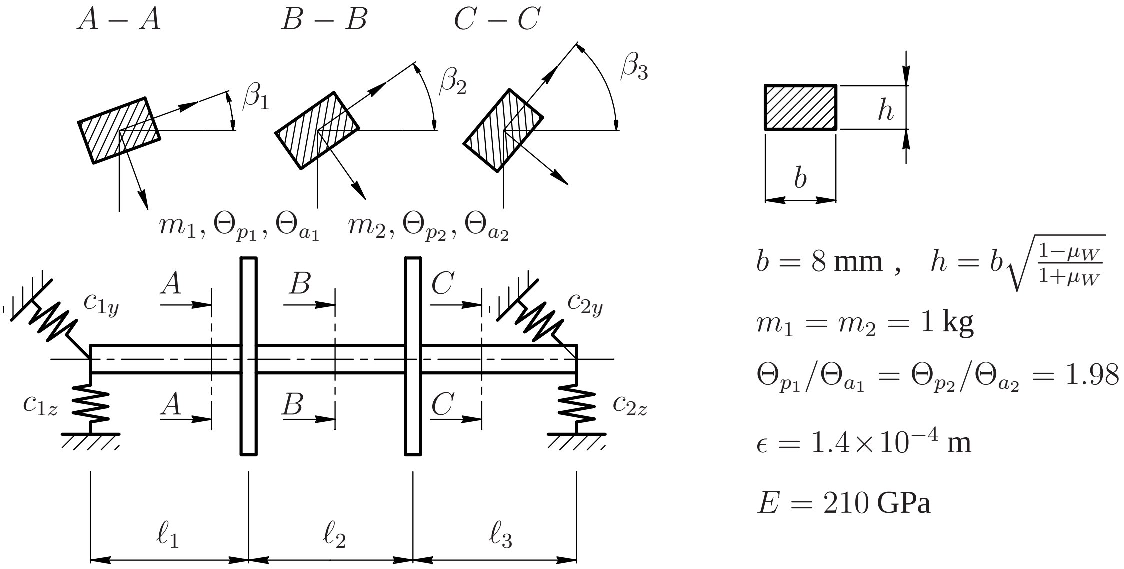

Figure 3.11: Anisotropic rotor model with two disks supported by anisotropic flexible bearings

3.5.2 Stability analysis

As studied in Chapter 2, comparing the anisotropic rotor with one disk supported by rigid or anisotropic flexible bearings, it is observed that the stability chart of the rotor supported by flexible bearings is separated into three regions of instability especially for rotor with a lower anisotropy (comparing Figure 2.16c to Figure 2.18).

In case of the pure anisotropic rotor with two disks supported by anisotropic flexible bearings, the stability charts are presented in Figures 3.12a and b. Comparing the stability charts of these models to the anisotropic rotor supported by rigid bearings (Model 5) as shown in Figure 3.3a, the first instability area in the frequency region 1.0 to 1.3 is also separated into three regions of instability. Especially in Figure 3.12a and b, the three separated areas widen for higher anisotropy ($\mu_W < 0.64$) for the bearing anisotropy $\mu_{L_1} = \mu_{L_2} = \mu_L = 0.3$ and ($\mu_W < 0.8$) for the bearing anisotropy $\mu_{L_1} = \mu_{L_2} = \mu_L = 0.6$. In the third instability area, there is no separated area as in the first instability area. Nevertheless, the third instability area becomes narrower and the vicinity of an anisotropy $\mu_W = 0.3$ the instability area vanishes. The second instability area does not occur, however, several tongues of instabilites occur in the left and the right of the third instability area.

In order to verify these FLOQUET stability charts, the dynamic responses in frequency domain of the rotor with a certain anisotropy are considered. In this section, the responses of the rotor with the anisotropy $\mu_W = 0.5$ and 0.3 supported by flexible bearings (the bearing anisotropy $\mu_{L_1} = \mu_{L_2} = \mu_L = 0.3$) are presented in Figure 3.12c and e, respectively.

For the same rotor cases supported by flexible bearings with the bearing anisotropy $\mu_{L_1} = \mu_{L_2} = \mu_L = 0.6$, the results are depicted in Figure 3.12d and f. In the instability area of the tongue

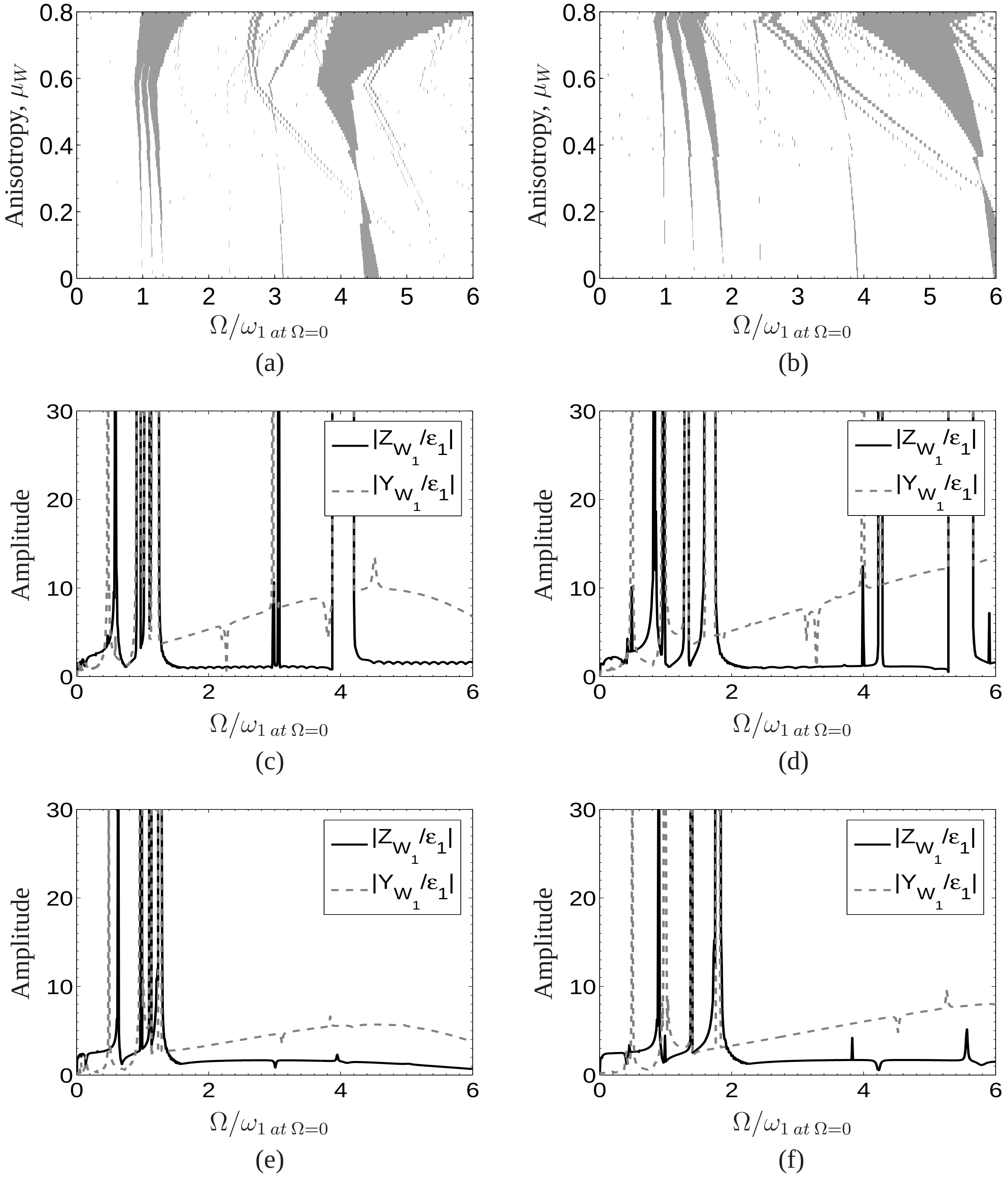

(a) (b)

(c) (d)

(e) (f)

Figure 3.12: Stability charts according to Floquet of undamped purely anisotropic rotor with two disks and for various shaft anisotropy ($\mu_W = 0$ to 0.8) supported by anisotropic flexible bearings with (a) $\mu_L = 0.3$ and (b) $\mu_L = 0.6$. The dynamic responses in frequency domain of the rotor for anisotropy $\mu_W = 0.5$ supported by anisotropic flexible bearings with the coefficient (c) $\mu_L = 0.3$ and (d) $\mu_L = 0.6$ and for anisotropy $\mu_W = 0.3$ with (e) $\mu_L = 0.3$ and (f) $\mu_L = 0.6$

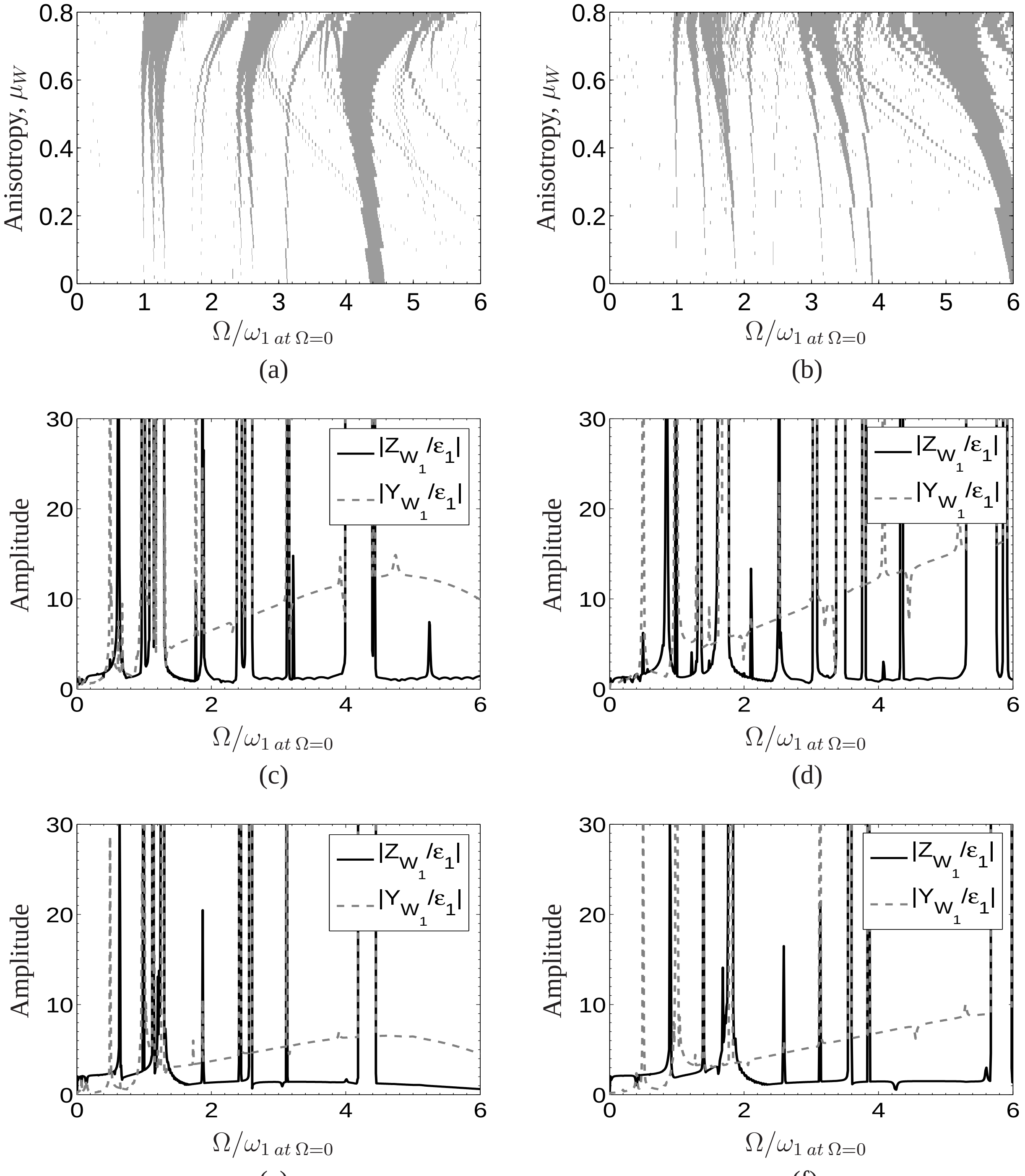

(a) (b)

(c) (d)

(e) (f)

Figure 3.13: Stability charts according to Floquet of undamped anisotropic rotor with two disks and for various shaft anisotropy ($\mu_W = 0$ to 0.8) with different shaft orientations $(\beta_1 = 0°, \beta_2 = 30°, \beta_3 = 60°)$ supported by anisotropic flexible bearings with (a) $\mu_L = 0.3$ and (b) $\mu_L = 0.6$. The dynamic responses in frequency domain of the rotor for anisotropy $\mu_W = 0.5$ supported by anisotropic flexible bearings with the coefficient (c) $\mu_L = 0.3$ and (d) $\mu_L = 0.6$ and for anisotropy $\mu_W = 0.3$ with (e) $\mu_L = 0.3$ and (f) $\mu_L = 0.6$

at rotational speed about 3 (see Figure 3.12c) or at rotational speed about 4.0 - 4.3 (see Figure 3.12d), the amplitude of the rotor is also higher. However, for the rotor with the ansotropy $\mu_W = 0.3$ as shown in Figures 3.12e and f, the amplitudes of the responses are very high only in the range of the three separated regions of the first instability area.

Furthermore, the cases of anisotropic rotor with different shaft orientations supported by anisotropic bearings are also investigated. The stability charts as shown in Figure 3.13a and b are presented. Similar to the analysis above, comparing these stability charts to the stability chart of the anisotropic rotor supported by rigid bearings (Model 7) as presented in Figure 3.3c, the three separated regions of instability occur in the first and the second instability areas, but not in the third instability region. Besides that, several tongues of instabilities also occur in the left and the right of the second and the third instability areas. Because of the separated regions and the occuring of tongues of instabilities the higher amplitudes of the responses also occur according to these stability areas. In case of an anisotropic rotor with the weight critical phenomenon, the amplitudes of the responses are relatively higher at rotational speed about half of the first critical speed. However, the weight critical speed is not defined as instability area in the FLOQUET stability charts.

Chapter 4

Experimental and numerical investigation

In this chapter, the developed model based on the strain energy method for asymmetric bending of a beam as presented in Chapters 2 and 3 will be benchmarked on a real anisotropic rotor with different shaft orientations supported by rigid bearings. Only one model of the rotor case is considered here. The dynamic behavior of the rotor is investigated not only at constant angular speed but also at constant angular acceleration. The experimental results are compared to the numerical results. For the numerical simulation, several assumptions are made to model the experimental anisotropic rotor. The natural frequencies will be determined from the whirl speeds of the rotor at rotational speed $\Omega = 0$. The dynamic responses which are influenced by unbalance disks and element anisotropy of the shaft will be shown in a spectral map and a Campbell diagram.

4.1 Experimental investigation

4.1.1 Rotor prototype

A prototype of an anisotropic rotor with two disks and different shaft orientations supported by four quasi-rigid bearings is depicted in Figure 4.1. The detail components are drawn in Figure 4.2 and outlined in the following:

- A steel shaft (X 90 CrMoV 18) with a diameter of 8 mm and a total length of 626 mm. The shaft length between the bearing (b) and the bearing (k) is 540 mm. The shaft is devided into three sections (A, B and C) with differently oriented cross-sections. The length of each section is 180 mm. Along 166 mm of the shaft section the thickness of the cross section is 5 mm. If the orientation of the first section is defined to be $\beta_1 = 0°$, the second and the third sections are $\beta_2 = 30°$ and $\beta_3 = 60°$, respectively.
- Four quasi-rigid bearings (b), (c), (j) and (k). The type of bearings are self-aligning ball bearings. In the radial direction, they are assumed to be rigid compared to the shaft stiffness.

- Two rigid disks (e) and (h) with the mass of each disk of 1.153 kg. The ratios of mass moment of inertia are $\Theta_{p_1}/\Theta_{a_1} = \Theta_{p_2}/\Theta_{a_2} = 1.90$. In each disk, 24 holes are drilled every $15°$ in order to attach well-defined unbalance masses.
- Two safety bearings (d) and (i) including four displacement sensors (only one sensor l, m of each safety bearing is shown). The V-position of the two sensors spans an angle of $90°$. By using a rotary transformation of $45°$, the displacement of the disk in horizontal and vertical direction can be measured.
- Two external dampers (f) and (g). The actual distance between a damper and the next disk is 55 mm,
- A coupling (a) that connects a servo-motor to the shaft.
- A servo-motor (shown in Figure 4.1 on the far left) attached at point (a) for generating the driving torque.

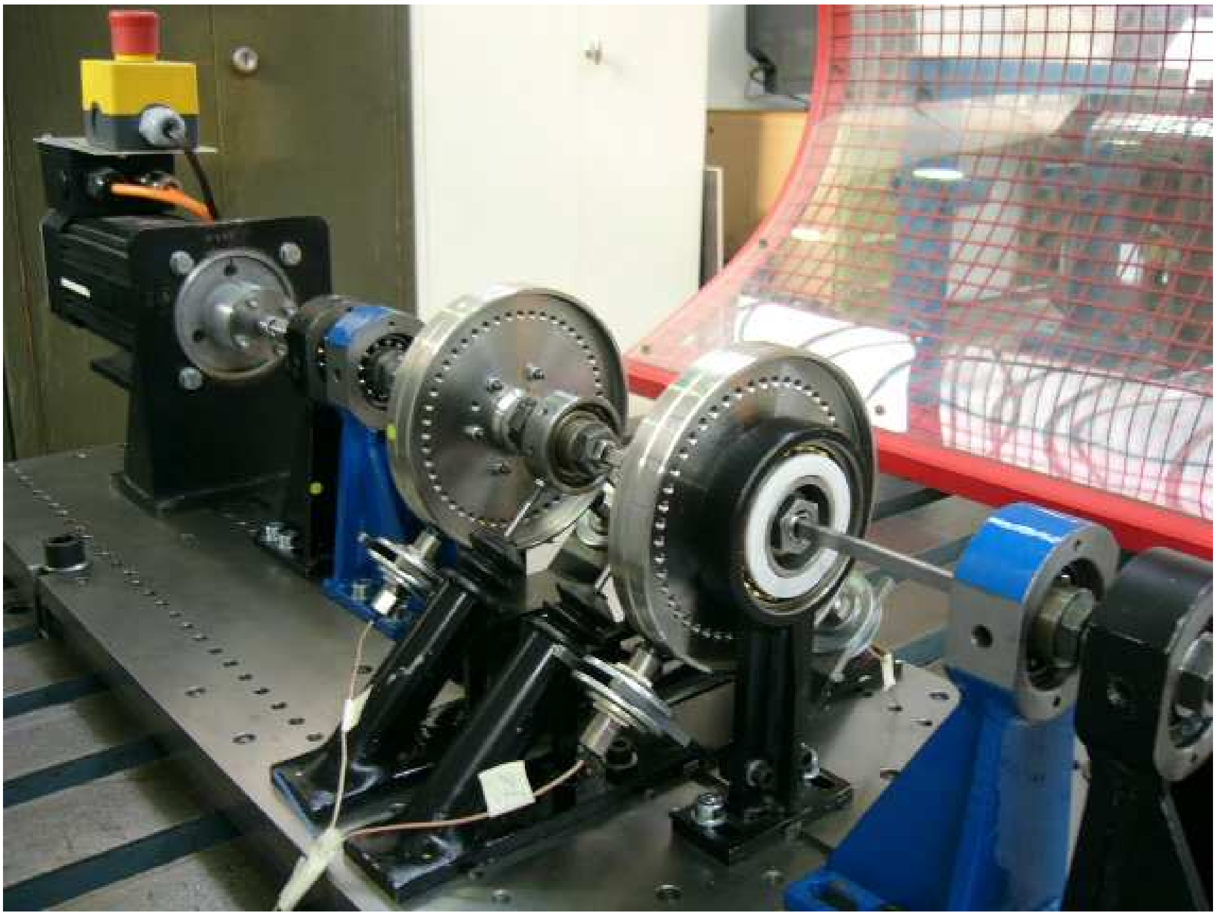

Figure 4.1: Prototype of an anisotropic rotor with two disks and different shaft orientations supported by four quasi-rigid bearings

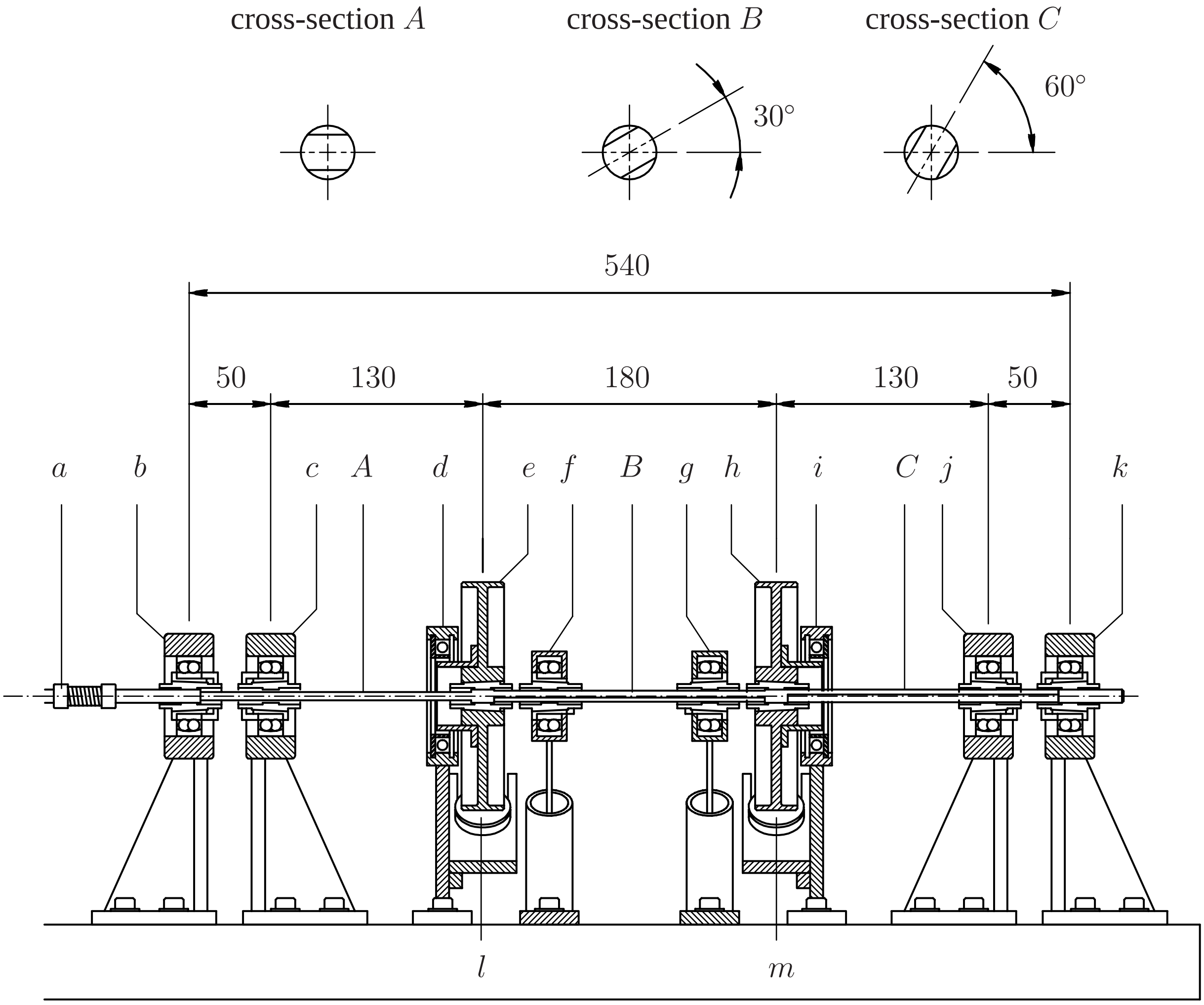

Figure 4.2: Technical drawing of the rotor prototype in Figure 4.2. Length unit is in milimeter

4.1.2 Running at constant angular speed

As mentioned in Section 4.1.1, two displacement sensors are fixed in each safety bearing in order to measure the displacement of the disk. The signals of the four displacement sensors are acquired by using the dSpace hardware type DS1103. The MATLAB software is used to control the dSpace and to process the signal data. The signals are filtered by a fourth order low-pass butterworth filter in MATLAB with a cut off frequency at 100 Hz. Using the sampling rate of $10\,000$ data/second and the number of sampling data 2^{16}, the data in one run are recorded in 6.5536 seconds.

A sample set of recorded data of the disk 1 in z-direction at the rotational speed $\Omega/2\pi = 10$ Hz is plotted in Figure 4.3a. This data is transformed into the frequency domain by using the fast fourier transform (FFT). The frequency content of the signal data is plotted in Figure 4.3b. The signal components at frequency Ω and 2Ω can be seen clearly. These correspond to the unbalance of the disk and the shaft anisotropy, respectively. At the rotational speed $\Omega/2\pi = 10$ Hz, the signal component corresponding to the shaft anisotropy occurs at frequency 20 Hz.

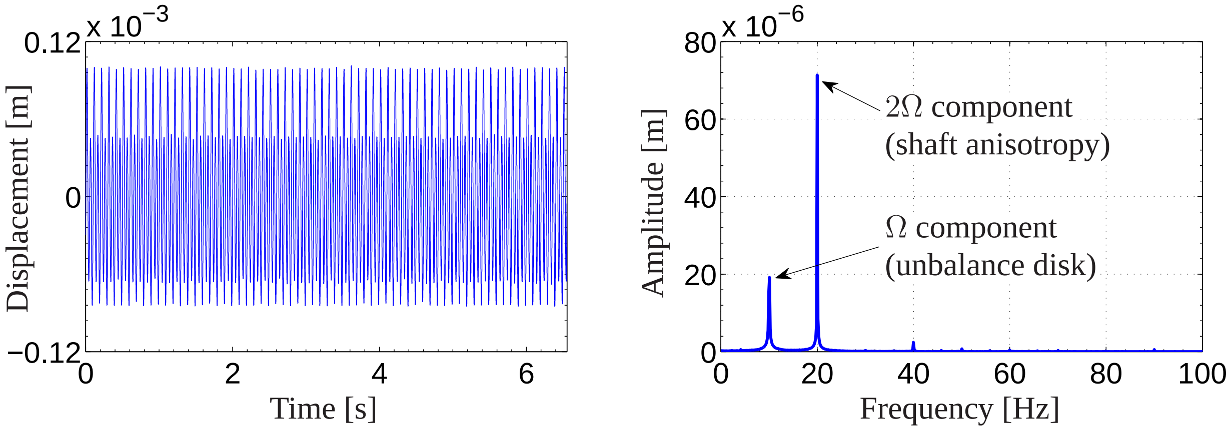

(a) (b)

Figure 4.3: (a) Signal data in the time domain of the disk 1 in z-direction (z_{W_1}) at rotational speed $\Omega/2\pi = 10$ Hz and (b) signal data in the frequency domain (Z_{W_1})

During the experiment, the rotor is operated at constant angular speed in the region between 1 and 80 Hz with an incremental step of 1 Hz. Again, the experimental data in time domain are transformed into the frequency domain by using FFT. The results are shown as spectral maps in Figure 4.4 for the responses at the disk 1 and 2, respectively. In these figures, the response amplitude R_{W_i} is the resultant of the response amplitudes of the disk i in y and z-direction,

$$|R_{W_i}| = \sqrt{Y_{W_i}^2 + Z_{W_i}^2} \tag{4.1}$$

At rotational speeds between 56 and 71 Hz (i.e. unstable region), the responses of the disks are very high and the prototype rotor is secured by the two safety bearings from a fatal damage. In order to avoid any damage to the rotor, the rotor is accelerated through this unstable region and no data is recorded.

The amplitudes of the Ω and 2Ω components in Figure 4.4 in dependency of the rotational speed are plotted in Figure 4.5. Comparing the Figure 4.5a to 4.5b, the Ω and 2Ω components are comparable but different although the assembly in Figure 4.2 is symmetric. This is mainly due to bowing of the shaft. While the Ω component in Figure 4.5a is slightly higher at rotational speeds around 25 Hz and very high about 56 - 71 Hz, the same component in Figure 4.5b is moderately higher at rotational speeds around 23 Hz and around 36 Hz and much higher about 56 - 71 Hz. The first interval (I) of these higher amplitudes corresponds to the range between the first and the second natural frequencies and the third interval (III) to the range between the third and the fourth natural frequencies of the rotor as presented in Figure 4.6a. This figure shows the responses in the frequency domain of the free vibration of the rotor at rest after an impact force at disk 2 in z-direction, in which the natural frequencies are defined by $f_1 \approx 21$ Hz, $f_2 \approx 26$ Hz, $f_3 \approx 55$ Hz and $f_4 \approx 68$ Hz. Because the peaks of the response magnitudes in Figure 4.6a have the different

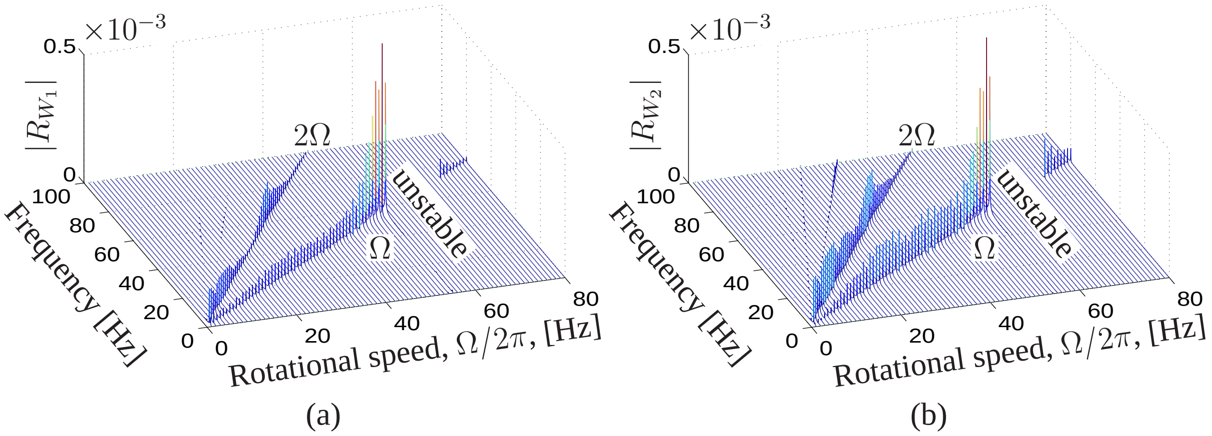

Figure 4.4: Spectral map of (a) the disk 1 and (b) the disk 2. No data is recorded at rotational speeds between 56 and 71 Hz (unstable)

values of the peaks of each natural frequency, these frequencies are approximation values based on the peaks in Figure 4.6a and the phases of the responses in Figure 4.6b. Besides, the first and the second natural frequency have wide peaks, in which the rotor system experiences high damping.

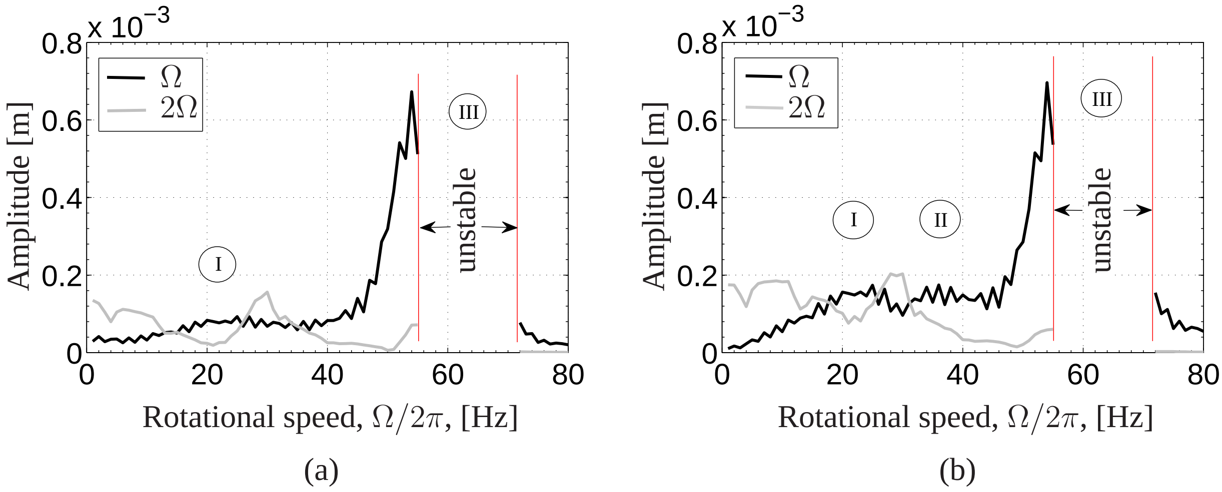

Figure 4.5: Dynamic responses in frequency domain of (a) the disk 1 and (b) the disk 2. No data is recorded for rotational speeds between 56 and 71 Hz (unstable region)

The responses of the disk 2 in Figure 4.5b tend to similar results which have three separated regions of instability as shown for the rotor cases in Chapter 3. The first region of instability corresponds to the region between the first and the second natural frequency (f_1 and f_2) and the third instability region to the third and the fourth natural frequency (f_3 and f_4) with a shift to higher frequencies. However, the response amplitudes in the first region (18 - 27 Hz) and the second region (around 36 Hz) do not show unstable responses. It was verified experimentally in Figure 4.6 that the rotor may be influenced by higher damping coefficient especially by the external dampers (f) and (g) in Figure 4.2. Besides, the three separated regions with slightly or moderately higher amplitudes do not occur in the responses of the disk 1 in Figure 4.5a. This may be caused by two possibilities. First, it may be caused by the coupling (a) in Figure 4.2 which holds the free motion of the shaft end. Therefore, a bending moment occurs in the bearing (b) which reduces the displacement near this bearing. For the disk 2, this effect is small because of the larger distance to the bearing (b). Second, it may be caused by a misalignment or bowing at the shaft centre line.

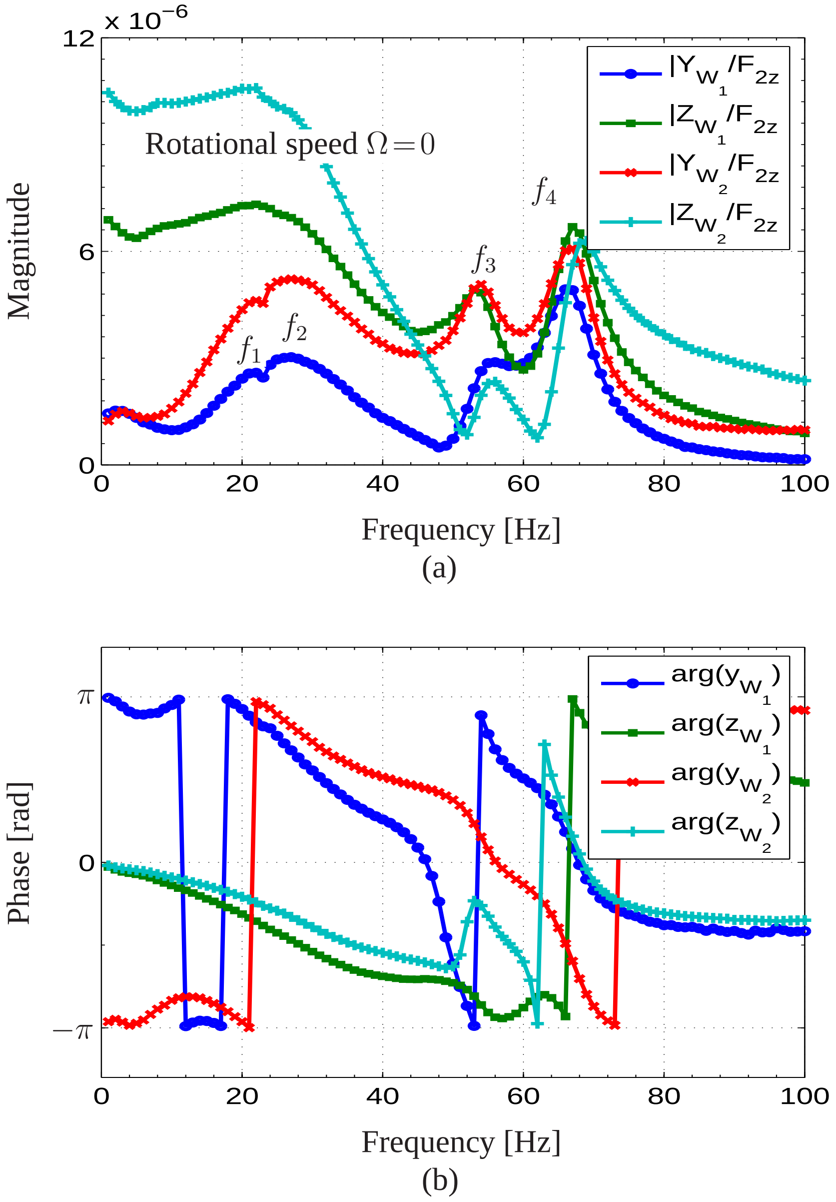

Figure 4.6: Free vibration responses in the frequency domain of the disks through an impact force at the disk 2 in z-direction: (a) magnitudes and (b) phases of the responses

In order to identify the damping coefficient of the rotor, the free vibration response z_{W_2} is analyzed by determining its logarithmic decrement (Λ). Because the response z_{W_2} in the time domain contains all natural frequencies, this response is filtered by using fourth order band-pass filter. By using a cut off of 10 - 23 Hz, the response of the first natural frequency is obtained as shown in Figure 4.7. Based on this figure, the damping coefficient (i.e. assumed as external damping coefficient) of the rotor is identified by the logarithmic decrement [35]

$$D_a = \frac{\Lambda}{\sqrt{4\pi^2 + \Lambda^2}} \approx 0.18 \quad . \tag{4.2}$$

However, this damping coefficient is an approximation value only, because the period of each oscillation motion is not exactly the same.

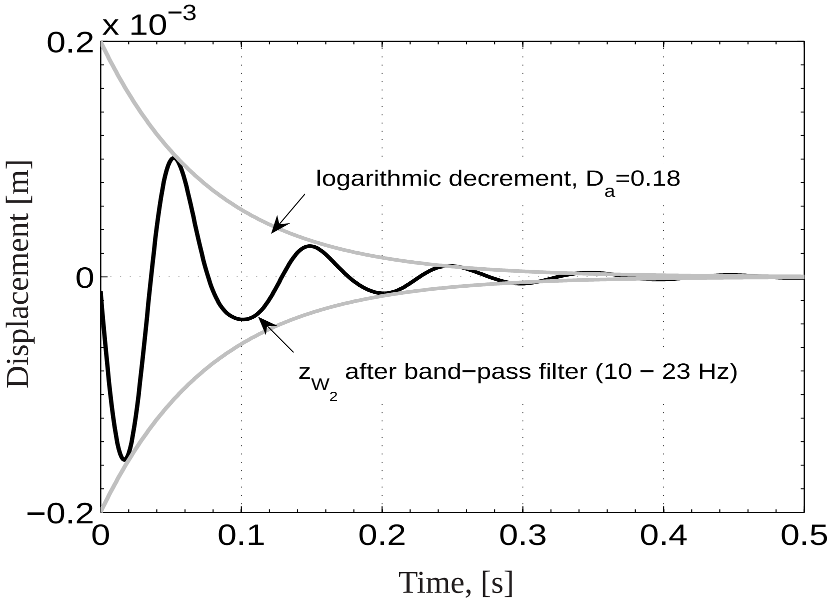

Figure 4.7: Free vibration response z_{W_2} according to Figure 4.6 after a band-pass filter with a cut off of 10 - 23 Hz (i.e. around the first natural frequency of the rotor)

As a comparison, orbit plots of the disks 1 and 2 are depicted at several speeds in Figure 4.8. In the figures, the orbit radius of the disk 2 is wider than the one of the disk 1. At low rotational speeds (e.g. $\Omega/2\pi = 1$ Hz) at which the unbalance forces acting on the disks are still small, the 2Ω component (i.e. effect of the shaft anisotropy) dominates the disk responses, especially for the disk 2. This response can be seen clearly in Figure 4.8b, whereas the smaller response at the 2Ω component of the disk 1 is shown in Figure 4.8a. According to the behavior of an anisotropic rotor as shown in Figure 1.1, the response of an anisotropic rotor should be like two identical circle orbits. This expected orbit corresponds only to the orbit plot of the disk 2 in Figure 4.8b. Based on this comparison, it can be concluded that the misalignment or the bowing exists at the shaft centre line, especially at the position around the disk 1. Therefore, the responses of the disk 1 are not suitable to be used in comparison between the experimental and numerical results in Section 4.3.

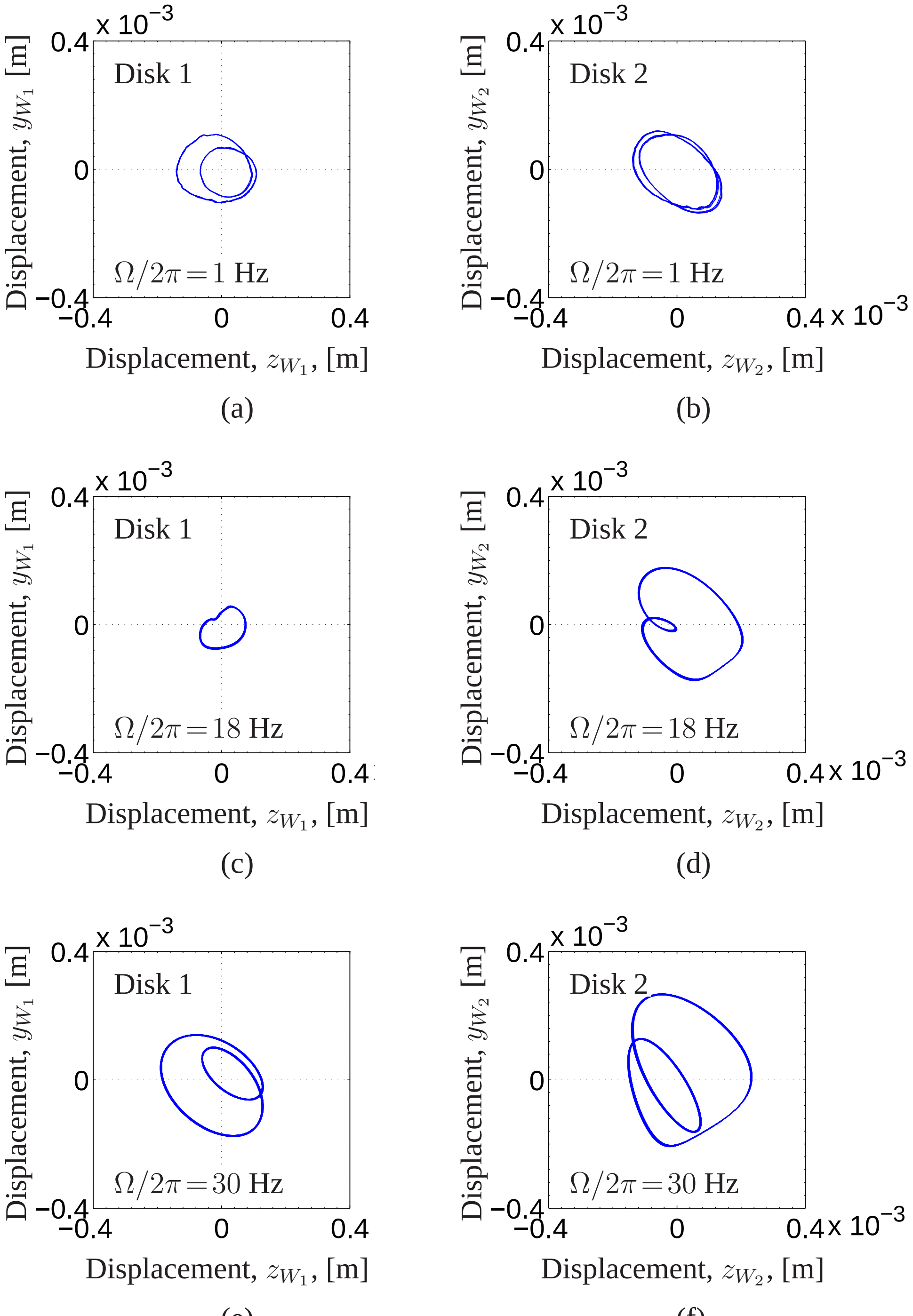

(a) (b)

(c) (d)

(e) (f)

Figure 4.8: Orbits of the disks in the rotor (a) and (b) at rotational speed $\Omega/2\pi = 1$ Hz, (c) and (d) at rotational speed $\Omega/2\pi = 18$ Hz and (e) and (f) at rotational speed $\Omega/2\pi = 30$ Hz (i.e. close to the weight critical speed)

Only the responses of the disk 2 will be used in the further comparison. Furthermore, a significant reduction in the response of the disk 1 occurs at the rotational speed $\Omega/2\pi = 18$ Hz as plotted in Figure 4.8c. At this rotational speed, the 2Ω component of the disk 1 is negligible, whereas it still exists in the disk 2. Nevertheless, the 2Ω component in the disk 1 is recovered at the rotational speed $\Omega/2\pi = 30$ Hz. The occurrence of the 2Ω component with the relatively high amplitude at the rotational speed of 30 Hz is caused by the instability region at frequency about $\Omega/2\pi = 60$ Hz. At this rotational speed, the rotor runs unstable.

4.1.3 Running at constant angular acceleration

In this section, the rotor is operated at constant angular acceleration. The rotor is run up from its rest condition until the rotational speed above $\Omega/2\pi = 80$ Hz is reached. The signal data is recorded in 120 seconds and the rotational speed reaches $\Omega/2\pi = 90$ Hz. In this condition, the acceleration rate is about $a = 4.71$ rad/s^2. The time histories of the responses are depicted in Figure 4.9. The figures show the responses of the disk 1 and 2 in z-direction. It is well known that the sources of vibration cannot be distinguished in the time domain. They show only the displacements of the disks during the accelerated rotor. At the time about $t = 34$ and 38 seconds, the displacements of the disks increase moderately. This increase corresponds to the two critical speeds. The first critical speed occurs at the time $t = 34$ second where the rotor runs at a rotational speed about $\Omega/2\pi = 25$ Hz and at the second critical speed at $t = 38$ second where about 28 Hz. Comparing these results to the first and the second natural frequencies which are obtained through the free vibration test as shown in Figure 4.6, the critical speeds which are obtained through the accelerated rotor test shift to higher frequencies. Further studies on this problem have been discussed in [11].

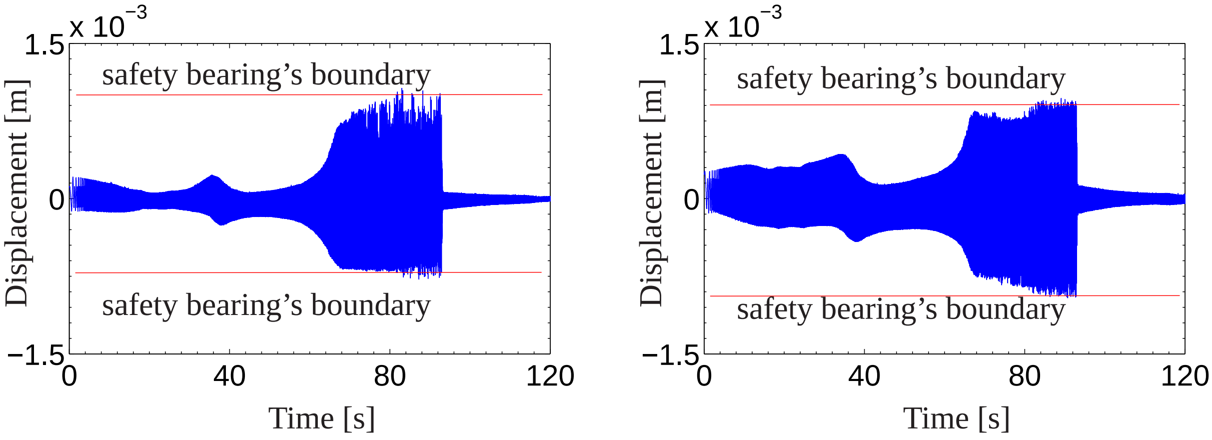

(a) (b)

Figure 4.9: Dynamic responses in the time domain of (a) the disk 1 and (b) the disk 2 in z-direction, in which the rotor is operated by constant angular acceleration

Furthermore, very high amplitudes of the disks occur during the measured time between $t = 68$ and 93 seconds. Here, the disks and the safety bearings are in contact. In order to investigate in more detail, the signal data in the time domain is processed into a spectrogram which is shown in

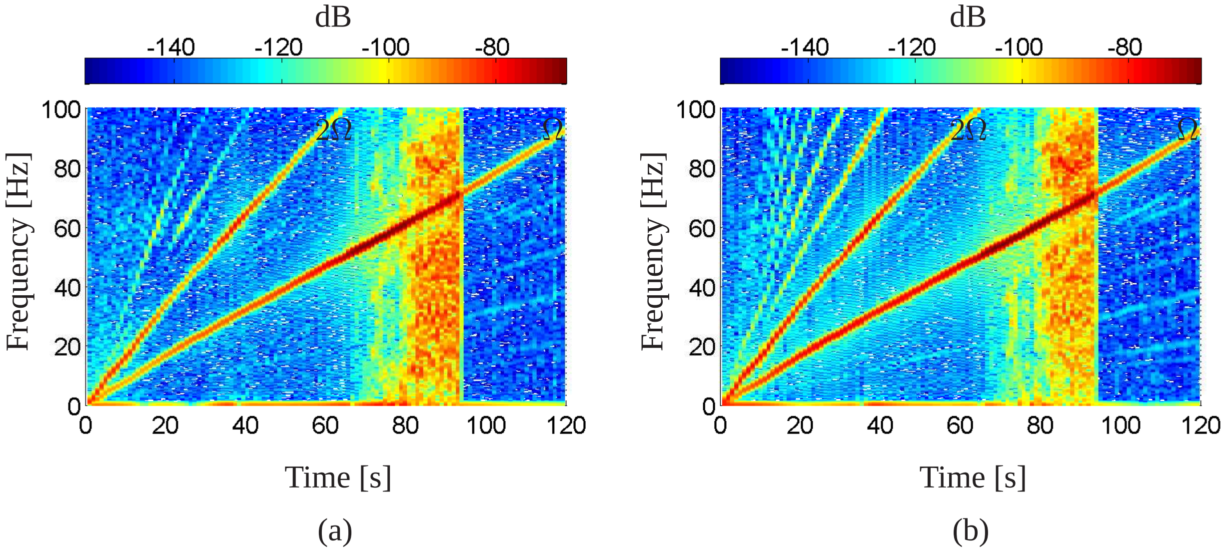

(a) (b)

Figure 4.10: Dynamic responses in the spectrogram of (a) the disk 1 and (b) the disk 2 in z-direction, in which the rotor is operated by constant angular acceleration

Figure 4.10. The figures show the signal data in the frequency domain against time. The response amplitudes are presented in a scaled colour. Similar to the spectral map, the vibration components in the spectrogram can be seen clearly. Again, the Ω and 2Ω component spectrums dominates. At the time about $t = 80$ - 93 seconds, the spectrograms show a wide range of frequency components. It means that an impact force occurs between a disk and its safety bearing. At this time, the rotor runs at the rotational speeds about 60 - 70 Hz. At the time about $t = 70$ - 80 seconds the rotor runs up at rotational speeds about 53 - 60 Hz and the displacements of the disks become very high, too. However, the contacts between the disk and its safety bearing do not occur with the big contact forces. These can be seen in Figure 4.10, where the wide range spectrum is depicted with moderately intensity of the scaled colour only.

4.2 Numerical investigation

In this section, the experimental anisotropic rotor as shown in Figure 4.2 is modelled by assuming several simplifications and calculated numerically. The natural frequencies and the whirl speeds of the rotor are analyzed and plotted in a Campbell diagram. The instability region is also investigated.

4.2.1 Modelling

The components of the prototype rotor as shown in Figure 4.2 have been described in Section 4.1. In this section, the experimental rotor is modelled by using several assumptions in order to simplify the modelling. The rotor is supported by four rigid bearings. Because the ball bearings are self-aligned, the angular positions of the bearings can move freely. The rotor shaft is assumed to be massless and has three shaft sections with the orientations of the cross-section ($\beta_1 = 0°$, $\beta_2 = 30°$ and $\beta_3 = 60°$) as shown in Figure 4.11. The thickness of each shaft section is 5 mm. Therefore, the coefficient of the shaft section anisotropy is $\mu_W = 0.41$. Two disks are attached on the shaft and each disk is placed in a node. The disks are identical, thin, rigid and have an eccentricity of $\varepsilon_1 = \varepsilon_2 = 33.4 \times 10^{-6}$ m and a ratio of mass moments of inertia of $\Theta_{p_1}/\Theta_{a_1} = \Theta_{p_2}/\Theta_{a_2} = 1.90$. The disks are placed at 180 mm from the bearing (b) and 180 mm from the bearing (k) (see Figure 4.2). The internal damping is assumed to be small, with the specific modal damping $D_i = 0.001$. In the numerical simulation, the external damping coefficient is adopted by comparison with the experimental results ($D_a = 0.18$ according to Figure 4.7). For the experimental rotor, the external damping comes from the two discrete dampers which are attached to the shaft at a distance of 55 mm from the disks. In the model, the external damping is assumed to act at exactly the disk position and to be proportional to the absolute velocity of the disk according to Equation (2.64).

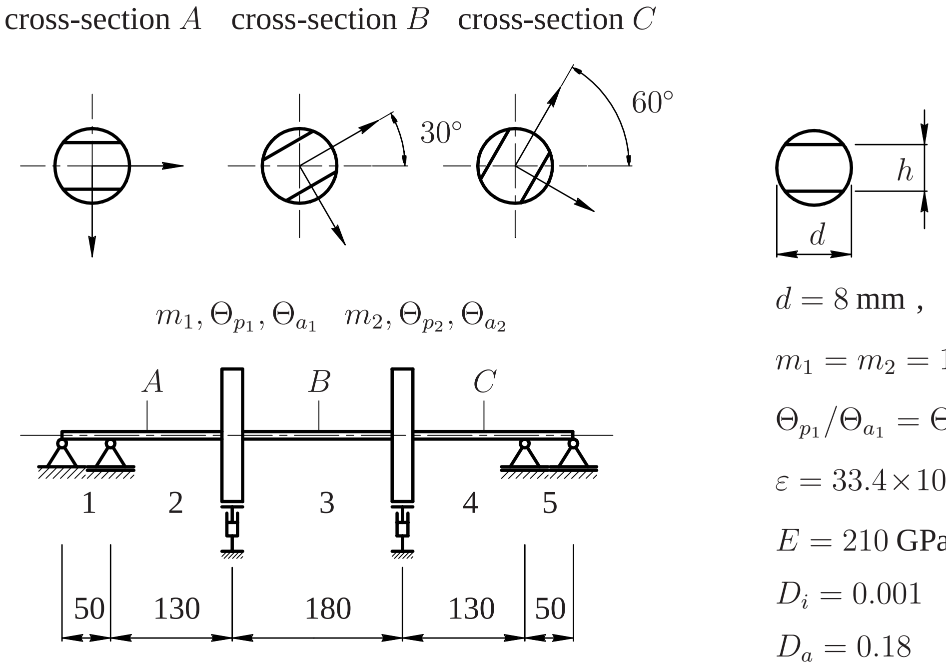

$d = 8$ mm , $h = 5$ mm

$m_1 = m_2 = 1.153$ kg

$\Theta_{p_1}/\Theta_{a_1} = \Theta_{p_2}/\Theta_{a_2} = 1.90$

$\varepsilon = 33.4 \times 10^{-6}$ m

$E = 210$ GPa

$D_i = 0.001$

$D_a = 0.18$

Figure 4.11: Modelling of the experimental rotor. Length unit is in milimeter

Furthermore, the stiffness of the shaft must be considered. Because the experimental rotor with two disks is supported by four rigid bearings, the derived equations in Section 3.2.1 cannot be used directly and must be modified. Based on the equations in Section 2.5.1, the flexibility of the experimental rotor can be derived accordingly. As shown in Figure 4.11, the shaft is discretized by five shaft elements. Therefore, the orientations of the discrete shaft elements are distributed as $\beta_1 = \beta_2 = 0°$, $\beta_3 = 30°$, $\beta_4 = \beta_5 = 60°$. The following steps are made to assemble the stiffness matrix of the experimental rotor. In the first step, the normalized forces and moments in the node of the disk 1 yield the reaction forces in the four supports. Therefore, the bending moment diagrams in η and ζ-directions are derived as a function of the shaft position x , see Figure 2.8. Similarly, the bending moment diagrams which come from the normalized forces and moments in the node of the disk 2 are obtained. In a second step, the flexibility influence coefficients can be calculated by using the Equations (3.1) - (3.3). Further, the flexibility matrix is obtained by assembling the flexibility influence coefficients into a matrix. By inverting this matrix the stiffness matrix of the experimental rotor is derived.

Other dynamic parameters (e.g. the internal and external damping matrices, the differential equations of translatory and rotary inertia) are considered based on the derived equations in Chapter 3. Because the experimental rotor runs at constant angular speed or at constant angular acceleration, it is not necessary to consider the torsions due to reaction forces in the bearings.

4.2.2 Simulation at constant angular speed

In this section, the stability of the rotor model shown in Figure 4.11 is investigated. According to Equation (2.125), the state-space matrices ***A*** and ***B*** are of size 16×16. Therefore, the solution of the equation gives 16 complex eigenvalues: eight complex and eight complex conjugate eigenvalues. By sorting and separating the eigenvalues into positive and negative imaginary values, the forward and backward whirl speeds of the rotor are determined. These forward and backward whirl speeds are transformed into the fixed reference frame and shown in the CAMPBELL diagram in Figure 4.12c for the rotor with $D_a = 0.18$. The decay rate plots obtained from the real parts of the eigenvalues are depicted in Figure 4.12b. As mentioned in Sections 2.10.1 and 3.4.2, the natural frequencies are obtained from the forward whirl speeds of the rotor at the rotational speed $\Omega = 0$. Based on the Figure 4.12a, the natural frequencies are defined as $f_1 = 25.3$ Hz, $f_2 = 33.5$ Hz, $f_3 = 55.7$ Hz and $f_4 = 72.8$ Hz.

The CAMPBELL diagram in Figure 4.12a shows only four of the eight forward f_i' and two of the eight backward whirl speeds $\bar{f}_i'$ of the rotor with the modal external damping coefficient $D_a = 0.18$. In this figure, at rotational speeds about 26.4 - 34.8 Hz and about 56.3 - 75.7 Hz the first whirl speeds of the forward and backward whirl (ω_1' and $\bar{\omega}_1'$) coincide with the Ω line. At rotational speeds about 42.7 - 51.8, the first and the second forward whirls coincide. However, in the decay rate plot in Figure 4.12b only the third instability region which lies in the interval of 57.7 - 74.2 Hz has positive real parts.

Besides, two intersection points ($P_1 = 14.6$ Hz and $P_2 = 30.8$ Hz) occur at the crossing of the 2Ω line and the curves of the whirl speeds in Figure 4.12a. At these points, the amplitudes of the 2Ω

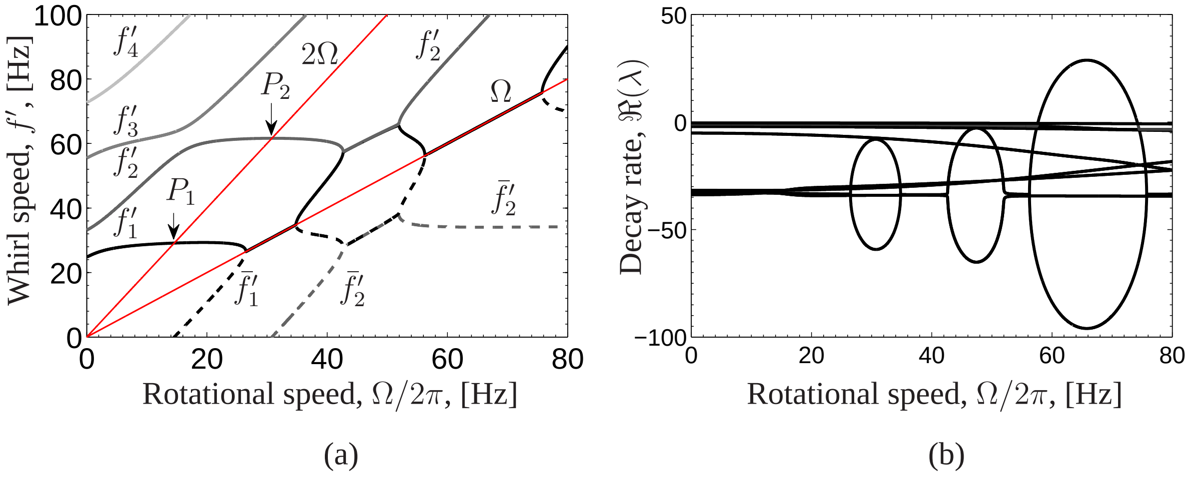

Figure 4.12: (a) Campbell diagram of the simulated rotor with the modal external damping coefficient $D_a = 0.18$ (only four of the eight forward and two of the eight backward whirl speed are shown), (b) decay rate plots (i.e. real parts) of the 16 eigenvalues of the rotor with the modal external damping coefficient $D_a = 0.18$

line are increased. The dynamic response amplitudes at these Ω and 2Ω lines are depicted in the spectral maps as presented in Figures 4.13a.

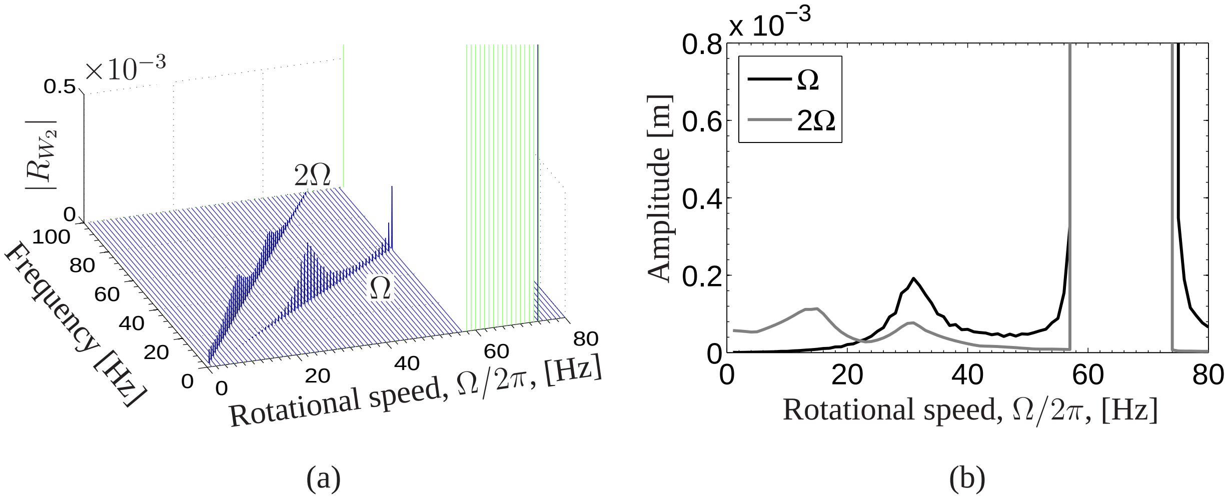

Figure 4.13: (a) Spectral map of disk 2 (R_{W_2}) at constant rotational speed from 1 to 80 Hz for rotor with the coefficient of external damping $D_a = 0.18$ and (b) dynamic response components in the frequency domain

Similar to Figure 4.5, the dynamic responses in the frequency domain of the rotor are presented in Figure 4.13b. In this figure, the first and the second peaks of the 2Ω component (see P_1 and P_2 in Figure 4.12b) occur at frequencies about 15 Hz and 31 Hz. At lower rotational speeds (i.e. from

$\Omega = 0$ to 10 Hz), the 2Ω components occur with moderately higher amplitudes. In this condition, the deflection of the rotor in one revolution is different. As mentioned in Section 1, it is caused by the anisotropy of the shaft.

4.2.3 Simulation at constant angular acceleration

For the rotor at constant angular acceleration, the acceleration rate of 4.71 rad/s^2 is chosen based on the experiment in Figure 4.10. The rotor is run up from the rest condition until it reaches the rotational speed of 90 Hz in 120 second. The results are depicted in Figure 4.14 for the responses at the disks 1 and 2. In the following simulation, the rotor with the external damping coefficient $D_a = 0.18$ is simulated. This external damping coefficient is chosen based on the determining of the logarithmic decrement of the dynamic response in Figure 4.7.

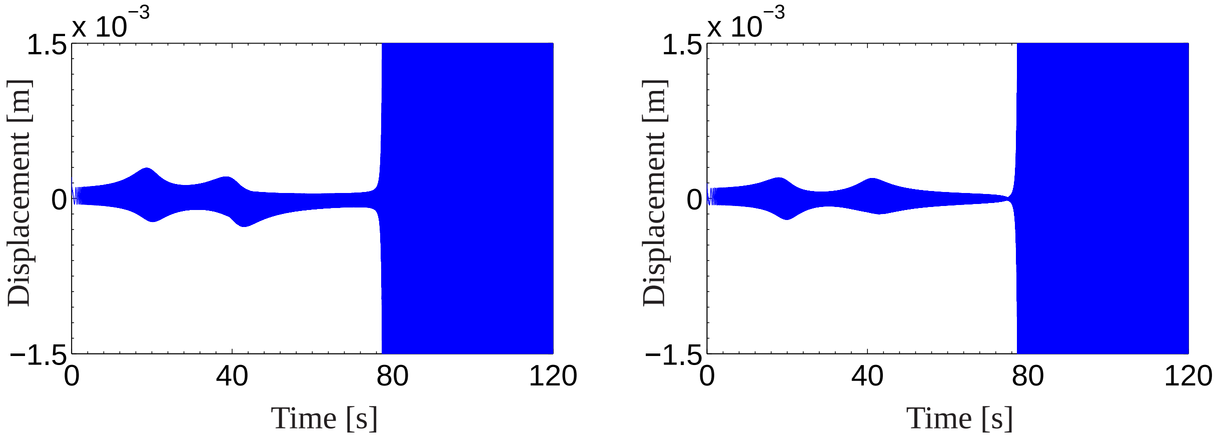

(a) (b)

Figure 4.14: Dynamic responses in the time domain of (a) the disk 1 and (b) the disk 2 in z-direction, in which the rotor is operated by constant angular acceleration

Comparing the numerical result in Figure 4.14 to the experimental results as shown in Figure 4.9, the moderately higher amplitudes in the numerical results occur at times about 39 and 43 seconds where the rotor runs at rotational speeds of 29 and 32 Hz, whereas the moderately high amplitudes in the experimental results occur at time about 34 and 38 seconds or at rotational speeds of 25 and 28 Hz. However, additional moderately higher amplitudes occur in the simulation at times about 18 and 20 seconds at rotational speeds 13.5 and 15 Hz. As mentioned in Section 4.1.3, the sources of vibration cannot be distinguished in the time domain. Therefore, according to the experimental results in Figure 4.5b, the responses of the 2Ω component at frequency of 15 Hz occur with moderately high amplitudes. Furthermore, In Figure 4.14, very high amplitudes occur in the rotor simulation at times after 78 seconds when the rotational speed of the rotor is above 58.5 Hz, whereas in the experiment they occur at time between 80 and 93 seconds at rotational speeds between 60 and 70 Hz. In the rotor simulation at time after 93 seconds at rotational speeds above 70 Hz, the response amplitude is still very high. It may be caused by the lack of the numerical precisions after very high values.

4.3 Comparison of experimental and numerical results

In this section, the natural frequencies which are obtained by experimental and numerical investigations are compared and listed in Table 4.1. The natural frequencies of the experiment are obtained from the free vibrations of the rotor at rest excited by an impact force at disk 2 in z-direction (see Figure 4.6), while in the numerical investigation they are obtained from an eigenvalue analysis of the rotor matrices at rotational speed $\Omega = 0$.

Table 4.1: Comparison of the natural frequencies

Natural frequency	Experimental [Hz]	Numerical [Hz] ($D_a = 0.18$)
1	21	25.3
2	26	33.5
3	55	55.7
4	68	72.8

Based on Table 4.1, the natural frequencies of the experiment are lower than the numerical simulation. If the numerical results are analyzed in more detail, possible causes can be identified. Higher natural frequencies in the numerical simulation are caused by the assumption of a massless shaft, massless bearings and massless dampers. It is well known that the higher the mass coefficient is at constant system stiffness, the lower is the natural frequency of the system.

The dynamic responses in frequency domain of the experimental (Figure 4.5b) and numerical study (Figures 4.13b) are compared in Figure 4.15. In general, the instability region of the experimental results occur only in the third region at frequencies 56 - 71 Hz, whereas in the numerical results at frequencies 57.7 - 74.2 Hz. Here, the third instability interval of the experimental result is narrower than the one of the numerical result.

Furthermore, the comparison of the regions with the relatively higher amplitudes or instability regions based on the Ω component of the responses in the disk 2 is listed in Table 4.2. The responses in the experimental results at rotational speeds around 23 Hz and around 36 Hz occur with the moderately higher amplitudes, whereas the moderately higher amplitudes in the numerical results occur at rotational speed around 31 Hz. In the numerical results, the first and the second regions of instability do not reach into the positive plane of the decay rate plot for the rotor with $D_a = 0.18$ (see Figure 4.13b). As the comparison, according to the simulation in Section 3 (3.3c), the instability regions of the anisotropic rotor (Model 7) exist in three areas.

Table 4.2: Comparison of the relatively higher amplitudes or the instability regions based on the Ω component of the responses at the disk 2

Region	Experimental [Hz]	Numerical [Hz] ($D_a = 0.18$)
1	18 - 27 $^{(*)}$	26.5 - 34.8 $^{(*/**)}$
2	34 - 38 $^{(*)}$	-
3	56 - 71	57.7 - 74.2

$^{(*)}$ the response amplitude in this region is moderately high only (not unstable)

$^{(**)}$ the region is defined by analyzing of the CAMPBELL diagram

Finally, the 2Ω component of the experimental results is compared to the numerical results. In the experimental results, the peaks of the 2Ω component occur at frequencies 15 Hz and 30 Hz, while in the numerical results at frequencies 14.6 Hz and 30.8 Hz. This comparison is listed in Table 4.3. At lower rotational speeds (i.e. rotational speeds from $\Omega = 0$ to 12 Hz), the 2Ω components of the experimental result in Figure 4.15 show the higher amplitudes compared to the numerical result. In the numerical result, the deflections of the rotor at lower rotational speeds are caused by the anisotropy of the shaft, whereas the greater deflections in the experimental results are caused not only by the anisotropy of the shaft but also by the misalignment or bowing in the shaft. Therefore, measured data up to 12 Hz were neglected in the following analysis.

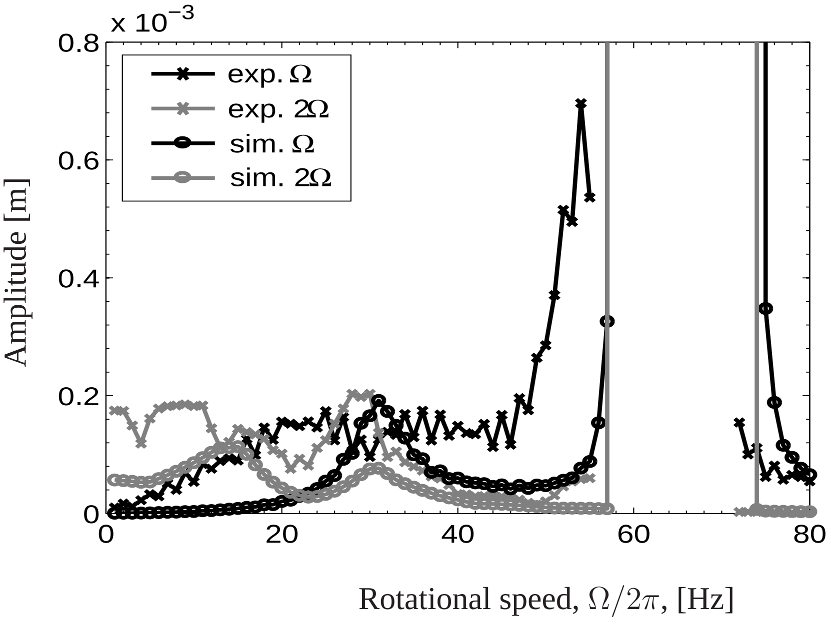

Figure 4.15: Comparison of the experiment and numerical results of the dynamic responses of the disk 2 (R_{W_2}) with the external damping coefficient $D_a = 0.18$

Table 4.3: Comparison of the peaks of the 2Ω component of the responses at the disk 2

Peak	Experimental [Hz] (Figure 4.15)	Numerical [Hz] ($D_a = 0.18$)
1	15	14.6
2	30	30.8

Based on the comparisons above, the shaft mass, the bearing mass and the damper mass should be taken into account in order to obtain lower natural frequencies of the rotor model numerically. Other possibilities for model errors are: the effect of misalignment and the assumptions that the damping is proportional to the absolute velocity of the disk, consideration of quasi-rigid bearings and neglection of the bending moment in the bearings (b) and (k).

The dynamics of the present rotor test rig can be modelled sufficiently well by the developed system equations. The instability region can be predicted sufficiently. However, due to the high external damping ($D_a = 0.18$) induced by the external damper configuration only one instability region could be verified. Therefore, in a future setup it is recommended to alter the configuration. Preliminary numerical simulations indicate that the experimental rotor should experience three instability regions at least for small values of the external damping ($D_a \leq 0.09$), similar to the prediction in Section 3 (Figure 3.3c) for undamped anisotropic rotor.

Chapter 5

Summary

The present work deals with a new discretization model of an anisotropic rotor. The rotor is supported by rigid or anisotropic flexible bearings. Because of different orientations of the cross-section along the shaft, the rotor is modelled by discrete elements. In the developed model, the shaft stiffness matrix is assembled in the rotating reference frame by considering asymmetric bending by means of the strain energy method. The shaft is assumed to be massless, because the shaft mass is very light compared to the rotor mass. By using the minimal number of discrete elements, the size of the shaft stiffness matrix can be minimalized. For an anisotropic rotor with a single disk, the shaft is discretized by two elements and for an anisotropic rotor with two disks by three elements only. The number of degrees of freedom of the system depends on the number of the disks. A disk possesses four degrees of freedom, in which the gyroscopic moments are taken into account. Therefore, the dynamic parameters of the rotor with single disk has the size of the matrices 4×4, whereas the rotor with two disks 8×8.

After considering the differential equations of motion of the anisotropic rotor, several stability investigations are conducted through analysis of eigenvalues for a speed-dependent rotor system and by using FLOQUET theory for a time-variant rotor system. As the basic comparison, a case of a purely anisotropic rotor with single disk which is discretized by using the minimal number of elements (i.e. two discrete shaft elements) is studied. The stability chart of the model shows that the location of the unstable area lies exactly in the range between the first and the second natural frequencies. By increasing the element anisotropy, the range of the instability becomes wider. By the difference in the shaft orientation in the rotor, the occurence of the gyroscopic moments in the system is not significant or very small, but it contibutes to the reduction of the interval of rotor instability. The bigger the difference in the shaft orientation $\Delta\beta$, the narrower is the range of the instability area. For the special case with the difference in the shaft orientation $\Delta\beta = 90°$, the instability area is located only at the first natural frequency of the rotor. It means, the shaft characteristic becomes a ”quasi-round shaft”. The effect of the gyroscopic moments occurs significantly if the disk position is asymmetric on the shaft. An increase in the gyroscopic moments causes the rotor to become stiffer and the instability range wider.

Furthermore, in case of the anisotropic rotor (e.g. with single disk and the shaft is discretized by two elements) supported by anisotropic flexible bearings, the stability chart shows three separated regions of instability especially for the lower element shaft anisotropy. With higher bearings anisotropy, three separated regions of instability reach to a higher element anisotropy of the shaft.

In case of the anisotropic rotor with single disk supported by rigid bearings and accelerated through the instability region, the higher acceleration rate is needed compared to the round rotor. In the other word, by using the same rate of acceleration, the reached maximum amplitudes depend on the element anisotropy μ_W of the rotor. The higher the anisotropy coefficient of the rotor, the higher is the maximum amplitude. For the rotor with the same element anisotropy, but the difference in the shaft orientation $\Delta\beta$ is varied, the bigger the difference in the shaft orientation, the lower is the reached maximum amplitude.

Similar to the case of a single disk anisotropic rotor, several investigations of stability are conducted in order to study the instability regions of the anisotropic rotor with two disks supported by rigid or anisotropic flexible bearings. In case of the purely anisotropic rotor, the instability area has two regions (i.e. termed as instability area 1 and 3), whereas the anisotropic rotor with two disks and different shaft orientations has three regions of instability. The difference in the shaft orientation affects the occurrence of the second region of instability. The bigger the difference in the shaft orientation, the wider is the range of the second instability region. However, the largest interval of the second instability occurs if the difference in the shaft orientation is 90°. The different shaft orientations cause a reduction of the interval of the first and the second regions of instability. Nevertheless, for $\Delta\beta > 90^\circ$, the interval of all regions of instability becomes narrower. Comparing the instability areas of the purely anisotropic rotor supported by rigid bearings to the rotor supported by anisotropic flexible bearings, the first instability area of the rotor supported by anisotropic flexible bearings is separated into three regions of instability. Besides that, several tongues of instabilites occur to the left and to the right of the third instability area. Similarly, comparing the instability areas of the anisotropic rotor with different shaft orientations supported by rigid bearings to the rotor supported by anisotropic flexible bearings, the three separated regions of instability occur in the first and the second instability areas. In the third instability area there is no the separated region of instability. Besides that, several tongues of instabilities also occur in the left and the right of the second and the third instability areas.

In case of a twisted anisotropic rotor with two disks supported by rigid bearings, the rotor shaft can be discretized by the minimal or higher number of shaft elements. The orientation of the elements are distributed linearly along the shaft. In this case, the instability area has also three regions. By using the higher number of the discrete elements on the shaft, the natural frequencies and the instability areas can be obtained with more accurate values. Especially for the investigation of the second instability region, the use of a higher number of shaft elements is recommended.

The weight critical speeds of the anisotropic rotor with one or two disks and different shaft orientations occur usually at rotational speed about half of the instability areas. Based on the investigated cases in Chapters 2 and 3, the dynamic responses in frequency domain shows the higher amplitudes of the responses at these speeds. However, in the FLOQUET stability charts the weight critical speeds are not defined as unstable area.

Furthermore, the investigation of an anisotropic rotor with two disks and different shaft orientations is conducted at constant angular speed and constant angular acceleration experimentally. In order to verify the developed discretization model, an experimental rotor is modelled and simulated numerically. The comparison results show that the model has been well developed, although several irregularities occur in the comparison results. Several possibilities can cause these irregularities, such as the assumptions of a massless shaft, massless bearings, massless dampers, no misalignment at the shaft, damping proportional to the absolute velocity of the disk, quasi-rigid bearings and no bending moment in the leftest and the rightest bearings.

For future work, a further identification of the rotor is recommended. A modification in the experimental rotor should be conducted (e.g. misalignment at the shaft should be reduced and the external damping in the rotor should be designed with a lower coefficient in order to investigate all regions of instability) or by modification in the numerical formulation (e.g. the shaft is modelled by a distributed mass and the bending moments acting in the outer bearings should be taken into account). Furthermore, other methods e.g. transfer matrix method ([22], [46]) or one-dimensional finite element ([10], [12]) with different shaft orientations can be developed. In the transfer matrix method, the mass and the stiffness matrices of a rotor are derived similar to the presented method in this work. The mass of the rotor is modelled by many lumped masses along the shaft. However, the stiffness matrix of the rotor shaft should be developed in which the difference in the shaft orientation is taken into account. Nevertheless, the size of the system matrices is still constant during the assembling of the discrete elements. Furthermore, in the one-dimensional finite element method, the mass and the stiffness matrices of the shaft are derived based on the discretization of a continuous rotor. The shape function according to the element interpolation should be also derived for discrete elements with different orientations.

Bibliography

[1] ACKERMANN, T., MARKERT, R., WEGENER, G., WIESE, D.: Reduktion der doppelt umlauffrequenten Schwingungen von anisotropen Walzen, Schwingungen in rotierenden Maschinen IV (1997), Braunschweig/Wiesbaden: View Verlag, pp. 130-139.

[2] ARIARATNAM, S.T.: The Vibration of Unsymmetrical Rotating Shafts, Journal of Applied Mechanics, Transactions of ASME (1965), pp. 157-162.

[3] BERGMANN, K.: Numerische Integration linearer zeitvarianter Systeme, ZAMM, 71 (1991) 12, pp. 511-515.

[4] BREITWIESER, M.: Identifikation und Reduktion der Anisotropie kontinuierlicher elastischer Rotoren, Diplomarbeit am 1. Institut für Mechanik der TH Darmstadt, 1997.

[5] CHEN, L.-W., PENG, W.-K. : Stability Analyses of a Timoshenko Shaft with Dissimilar Lateral Moments of Inertia, Journal of Sound and Vibration, (1997) 207(1), pp. 33-46.

[6] EWINS, D.J: Modal Testing: Theory and Practice, Letchworth, Hertfordshire, England: Research Studies Press Ltd., Brüel and Kjær, 1986, ISBN: 0-86380-036-X.

[7] GANESAN, R.: Effects of Bearing and Shaft Asymmetries on the Instability of rotors operating at near-critical speeds, Mechanism and Machine Theory 35 (2000), pp. 737-752.

[8] GASCH, R., MARKERT, R., PFÜTZNER, H.: Acceleration of Unbalanced Flexible Rotors Through the Critical Speeds, Journal of Sound and Vibration (1979) 63(3), pp.393-409.

[9] GASCH, R., KNOTHE, K.: Strukturdynamik, Band 1: Diskrete Systeme, Berlin Heidelberg: Springer-Verlag, 1987, ISBN: 3-540-16849-4.

[10] GASCH, R., KNOTHE, K.: Strukturdynamik, Band 2: Kontinua und ihre Diskretisierung, Berlin Heidelberg: Springer-Verlag, 1989, ISBN: 3-540-50771-X.

[11] GASCH, R., NORDMANN, R., PFÜTZNER, H.: Rotordynamik, 2. Auflage, Berlin Heidelberg: Springer-Verlag, 2006, ISBN: 3-540-41240-9.

[12] GENTA, G.: Dynamics of Rotating Systems, New York: Springer-Verlag, 2005, ISBN: 9780387286877.

[13] GENTA, G., DELPRETE, C.: Acceleration through Critical Speeds of an Anisotropic, Non-Linear, Torsionally Stiff Rotor with many Degrees of Freedom, Journal of Sound and Vibration (1995) 180 (3), pp. 369-386.

[14] HIBBELER, R.C.: Technische Mechanik 2 Festigkeitslehre, 5. überarbeitete und erweitere Auflage, Pearson Studium Deutschland GmbH, 2006, ISBN: 3-8273-7134-1.

[15] HULL, E.H.: Shaft Whirling as Influenced by Stiffness Asymmetry, ASME Journal of Engineering for Industry 83 (1961), pp. 219-226.

[16] IKEDA, T., MURAKAMI, S.: Dynamic Response and Stability of a Rotating Asymmetric Shaft Mounted on a Flexible Base, Nonlinear Dynamics 20, 1999, pp. 1-19.

[17] IWATSUBO, T., KANKI, H., KAWAI, R.: Vibration of Asymmetric Rotor Through Critical Speed with Limited Power Supply, Journal Mechanical Engineering Science, Vol. 14 No. 3, 1972, pp. 184-194.

[18] IWATSUBO, T., TOMITA, A., KAWAI, R.: Vibrations of Asymmetric Rotors Supported by Asymmetric Bearings, Ingenieur-Archiv 42, (1973), pp. 416-432.

[19] IWATSUBO, T., TSUJIUCHI, N., INOUE, T.: Vibration of Asymmetric Rotor supported by Oil Film Bearings, Ingenieur-Archiev 56 (1986), pp. 1-15.

[20] KANG, Y., HWANG, W.-W.: Influence of Bearing Damping on Instability of Asymmetric Shafts - Part 1: Stabilizing and Destabilizing Effects, International Journal of Mechanical Science, Vol. 38, No. 12 (1996), pp. 1349-1358.

[21] KANG, Y., LEE, Y.-G.: Influence of Bearing Damping on Instability of Asymmetric Shafts - Part 3: Disk Effects, International Journal of Mechanical Science, Vol. 39, No. 9 (1997), pp. 1055-1065.

[22] KANG, Y., LEE, Y.-G., CHEN, S.-C.: Instability Analysis of Unsymmetrical Rotor-Bearing Systems Using the Transfer Matrix Method, Journal of Sound and Vibration (1997) 199 (3), pp. 381-400.

[23] KELLENBERGER, W.: Biegeschwingungen einer unrunden, rotierenden Welle in horizontaler Lage, Ingenieur-Archiv 26, (1958), pp. 302-318.

[24] KRÄMER, E.: Maschinendynamik, Berlin Heidelberg: Springer-Verlag, 1984, ISBN: 3-540-12541-8.

[25] KRÄMER, E.: Dynamics of Rotors and Foundations, Berlin Heidelberg: Springer-Verlag, 1993, ISBN: 3-540-55725-3.

[26] KREYSZIG, E.: Advanced Engineering Mathematics, 9th Edition, John Wiley and Sons, Inc., 2006, ISBN: 0471728977.

[27] LEE, H.P.: Dynamic Stability of Spinning Beams of Unsymmetrical Cross-Section with Distinct End Condition, Journal of Sound and Vibration (1996) 189 (2), pp. 161-171.

[28] MARKERT, R., PFÜTZNER, H., GASCH, R.: Mindestantriebsmoment zur Resonanzdurchfahrt von unwuchtigen elastischen Rotoren, Forsch.Ing.-Wes. Bd.46 (1980) Nr.2, pp.33-68.

[29] MARKERT, R.: Resonanzdurchfahrt unwuchtiger biegeelastischer Rotoren, VDI Forschritt-Berichte Reihe 11, Nr. 34, Düsseldorf: VDI-Verlag, (1980).

[30] MARKERT, R.: System- und Unwuchtidentification von elastischen Rotoren aus Anfahrmessungen, VDI-Berichte, Nr. 536, (1984), pp.121-140.

[31] MARKERT, R.: Modal Balancing of Flexible Rotors with Data Aquisition from Non-stationary Run-up and Run-down, Proc. 6th International Modal Analysis Conference, Vol. I, (1988), pp.310-316.

[32] MARKERT, R.: Computergestützte Verfahren zur Unwuchtbestimmung von starren und elastischen Rotoren, VDI-Berichte, Nr. 904, (1991), pp.243-261.

[33] MARKERT, R.: Technische Mechanik, Teil A und B, Skript zur Vorlesung, 1. Auflage, TU Darmstadt, 2002.

[34] MARKERT, R.: Rotordynamik, Skript zur Vorlesung, 1. Auflage, Fachbereich Mechanik, TU Darmstadt, 2003.

[35] MARKERT, R.: Strukturdynamik, 1. Auflage, Fachbereich Maschinenbau, TU Darmstadt, 2006.

[36] MASKE H.: Untersuchung einer rotierende Welle in elastischen Lagern bei asymmetrischer Wellensteifigkeit und asymmetrischer Rotordrehmasse, Dissertation an der TU Berlin, 1972.

[37] MEIROVITCH, L.: Elements of Vibration Analysis, New York: McGraw-Hill Book Company, 1975, ISBN: 0-07-041340-1.

[38] MICHATZ, J.: Das Biegeverhalten einer einfach besetzten, unrunden rotierenden Welle unter Berücksichtigung äußerer und innerer Dämpfungeinflüsse, Dissertation an der TU Berlin, 1970.

[39] MUSZYŃSKA, A.: Rotordynamics, Boca Raton: CRC Press, Taylor and Francis Group, 2005, ISBN: 0-8247-2399-6.

[40] N.N.: Using MATLAB, version 5, 1996.

[41] ONCESCU, F., LAKIS, A.A., OSTIGUY, G.: Investigation of the Stability and Steady State Response of Asmmetric Rotors using Finite Element Formulation, Journal of Sound and Vibration (2001) 245 (2), pp. 303-328.

[42] OTA, H., KONO, K.: Unstable Vibrations Induced by Rotationally Unsymmetric Inertia and Stiffness Properties, JSME Vol. 14 No. 67 (1971), pp. 29-38.

[43] OTA, H., MIZUTANI, K., NAKATSUGAWA, Y.: On the Shaft End Torque and the Forced Vibrations of an Asymmetrical Shaft Carrying an Asymmetrical Rotor, JSME Vol. 26 No. 222 (1983), pp. 2178-2185.

[44] PAZ, M.: Structural Dynamics, New York: Van Nostrand Reinhold Company, 1985, ISBN: 0-442-27535-8.

[45] RAO, J.S.: Rotor Dynamics, New Delhi, Bangalore, Bombay, Calcutta: Wiley Eastern Limited, 1983, ISBN: 0-85226-787-8.

[46] RAO, J.S., SREENIVAS, R.: Dynamics of Asymmetric Rotors using Solid Models, Proceedings of the International Gas Turbine Congress 2003, Tokyo, TS-016.

[47] SENKER, P.: Stabilitätsanalyse elastischer Rotorsysteme, Dissertation an der TU Brauschweig, 1993.

[48] TEICHMANN H.: Biegeschwingungsverhalten von unrunden Rotoren in Gleitlagern, Dissertation an der TU Berlin, Verlag Shaker, Aachen, 1995, ISBN-10: 3826509781.

[49] WALTER, F.: Bewegungsdifferentialgleichungen für das Auf- und Abfahren einer Laval-Welle, Diplomarbeit am 1. Institut für Mechanik der TU Berlin, 1978.

[50] WEGENER, G.: Untersuchungen zum Kreiseleinfluss auf den stationären und instationären Betrieb von elastischen Rotoren, Diplomarbeit am Institut für Mechanik der TU Darmstadt, 1993.

[51] WETTERGREN, H.L., OLSSON, K.-O.: Dynamic Instability of a Rotating Asymmetric Shaft with Internal Viscous Damping Supported in Anisotropic Bearings, Journal of Sound and Vibration (1996) 195 (1), pp. 75-84.

[52] WIEDEMANN, M., PERSON, M.: Die Stabilität und die Empfindlichkeit der Stabilität periodisch zeitvarianter Systeme in der Rotordynamik, Forschung im Ingenieurwesen - Engineering Research, Bd. 58 (1992) Nr. 9, pp. 213-222.

[53] WÖLFEL, H.P.: Maschinendynamik, Fachbereich Maschinenbau, TU Darmstadt, 2003.

[54] XU, J., GASCH, R.: Modale Behandlung linearer periodisch zeitvarianter Bewegungsgleichungen, Achieve of Applied Mechanics, 65 (1995), pp. 178-193.

[55] YAMAMOTO, T., OTA, H., KONO, K.: On the Unstable Vibrations of a Shaft with Unsymmetrical Stiffness Carrying an Unsymmetrical rotor, Journal of Applied Mechanics, 35 (1968), pp. 313-321.

Appendix A

Anisotropic rotor supported by rigid bearings

A.1 Flexibility matrix of shaft with different orientation

A special case of an anisotropic rotor with minimum number of elements or only with two elements is considered by using the Equation (2.52), hence the flexibility influence coefficients of shaft can be obtained as following

$$h_{ij} = \sum_{k=1}^{2} \int_{(\ell_k)} \frac{I_{k\zeta}}{E\left(I_{k\eta} I_{k\zeta} - I_{k\eta\zeta}^2\right)} \hat{M}_{ik\eta}(x)\, \hat{M}_{jk\eta}(x)\ dx \quad ;\ \text{for } i = 1,4 \text{ and } j = 1,4 \tag{A.1}$$

$$h_{ij} = \sum_{k=1}^{2} \int_{(\ell_k)} \frac{I_{k\eta}}{E\left(I_{k\eta} I_{k\zeta} - I_{k\eta\zeta}^2\right)} \hat{M}_{ik\zeta}(x)\, \hat{M}_{jk\zeta}(x)\ dx \quad ;\ \text{for } i = 2,3 \text{ and } j = 2,3 \tag{A.2}$$

$$h_{ij} = \sum_{k=1}^{2} \int_{(\ell_k)} \frac{-I_{k\eta\zeta}}{E\left(I_{k\eta} I_{k\zeta} - I_{k\eta\zeta}^2\right)} \hat{M}_{ik\eta}(x)\, \hat{M}_{jk\zeta}(x)\ dx \quad ;\ \text{for } i = 1,4 \text{ and } j = 2,3 \tag{A.3}$$

The flexibility influence coefficients can be arranged in a matrix notation as

$$\boldsymbol{H} = \begin{bmatrix} h_{11} & h_{12} & h_{13} & h_{14} \\ h_{12} & h_{22} & h_{23} & h_{24} \\ h_{13} & h_{23} & h_{33} & h_{34} \\ h_{14} & h_{24} & h_{34} & h_{44} \end{bmatrix} \tag{A.4}$$

where

$$\begin{aligned} h_{11} &= \frac{\ell_1^2\, \ell_2^2}{3E\, \ell^2} \left(\frac{I_{1\zeta}\, \ell_1}{I_{1\eta} I_{1\zeta} - I_{1\eta\zeta}^2} + \frac{I_{2\zeta}\, \ell_2}{I_{2\eta} I_{2\zeta} - I_{2\eta\zeta}^2} \right) \\ &= \frac{\ell_1^2\, \ell_2^2}{6E\, \ell^2} \left\{ \frac{\ell_1 \left[(I_{1\eta^*} + I_{1\zeta^*}) - (I_{1\eta^*} - I_{1\zeta^*}) \cos 2\beta_1 - 2 I_{1\eta^*\zeta^*} \sin 2\beta_1 \right]}{I_{1\eta^*} I_{1\zeta^*} - I_{1\eta^*\zeta^*}^2} \right. \end{aligned}$$

$$\left. + \frac{\ell_2 \left[(I_{2\eta^*} + I_{2\zeta^*}) - (I_{2\eta^*} - I_{2\zeta^*}) \cos 2\beta_2 - 2 I_{2\eta^*\zeta^*} \sin 2\beta_2 \right]}{I_{2\eta^*} I_{2\zeta^*} - I_{2\eta^*\zeta^*}^2} \right\} \tag{A.5}$$

$$\begin{aligned} h_{12} &= \frac{\ell_1^2\,\ell_2^2}{3E\,\ell^2} \left(\frac{I_{1\eta\zeta}\,\ell_1}{I_{1\eta} I_{1\zeta} - I_{1\eta\zeta}^2} + \frac{I_{2\eta\zeta}\,\ell_2}{I_{2\eta} I_{2\zeta} - I_{2\eta\zeta}^2} \right) \\ &= -\frac{\ell_1^2\,\ell_2^2}{6E\,\ell^2} \left\{ \frac{\ell_1 \left[(I_{1\eta^*} - I_{1\zeta^*}) \sin 2\beta_1 - 2 I_{1\eta^*\zeta^*} \cos 2\beta_1 \right]}{I_{1\eta^*} I_{1\zeta^*} - I_{1\eta^*\zeta^*}^2} \right. \\ &\qquad \left. + \frac{\ell_2 \left[(I_{2\eta^*} - I_{2\zeta^*}) \sin 2\beta_2 - 2 I_{2\eta^*\zeta^*} \cos 2\beta_2 \right]}{I_{2\eta^*} I_{2\zeta^*} - I_{2\eta^*\zeta^*}^2} \right\} \end{aligned} \tag{A.6}$$

$$\begin{aligned} h_{13} &= \frac{\ell_1\,\ell_2}{3E\,\ell^2} \left(\frac{I_{1\eta\zeta}\,\ell_1^2}{I_{1\eta} I_{1\zeta} - I_{1\eta\zeta}^2} - \frac{I_{2\eta\zeta}\,\ell_2^2}{I_{2\eta} I_{2\zeta} - I_{2\eta\zeta}^2} \right) \\ &= -\frac{\ell_1\,\ell_2}{6E\,\ell^2} \left\{ \frac{\ell_1^2 \left[(I_{1\eta^*} - I_{1\zeta^*}) \sin 2\beta_1 - 2 I_{1\eta^*\zeta^*} \cos 2\beta_1 \right]}{I_{1\eta^*} I_{1\zeta^*} - I_{1\eta^*\zeta^*}^2} \right. \\ &\qquad \left. - \frac{\ell_2^2 \left[(I_{2\eta^*} - I_{2\zeta^*}) \sin 2\beta_2 - 2 I_{2\eta^*\zeta^*} \cos 2\beta_2 \right]}{I_{2\eta^*} I_{2\zeta^*} - I_{2\eta^*\zeta^*}^2} \right\} \end{aligned} \tag{A.7}$$

$$\begin{aligned} h_{14} &= \frac{\ell_1\,\ell_2}{3E\,\ell^2} \left(\frac{I_{1\zeta}\,\ell_1^2}{I_{1\eta} I_{1\zeta} - I_{1\eta\zeta}^2} - \frac{I_{2\zeta}\,\ell_2^2}{I_{2\eta} I_{2\zeta} - I_{2\eta\zeta}^2} \right) \\ &= \frac{\ell_1\,\ell_2}{6E\,\ell^2} \left\{ \frac{\ell_1^2 \left[(I_{1\eta^*} + I_{1\zeta^*}) - (I_{1\eta^*} - I_{1\zeta^*}) \cos 2\beta_1 - 2 I_{1\eta^*\zeta^*} \sin 2\beta_1 \right]}{I_{1\eta^*} I_{1\zeta^*} - I_{1\eta^*\zeta^*}^2} \right. \\ &\qquad \left. - \frac{\ell_2^2 \left[(I_{2\eta^*} + I_{2\zeta^*}) - (I_{2\eta^*} - I_{2\zeta^*}) \cos 2\beta_2 - 2 I_{2\eta^*\zeta^*} \sin 2\beta_2 \right]}{I_{2\eta^*} I_{2\zeta^*} - I_{2\eta^*\zeta^*}^2} \right\} \end{aligned} \tag{A.8}$$

$$\begin{aligned} h_{22} &= \frac{\ell_1^2\,\ell_2^2}{3E\,\ell^2} \left(\frac{I_{1\eta}\,\ell_1}{I_{1\eta} I_{1\zeta} - I_{1\eta\zeta}^2} + \frac{I_{2\eta}\,\ell_2}{I_{2\eta} I_{2\zeta} - I_{2\eta\zeta}^2} \right) \\ &= \frac{\ell_1^2\,\ell_2^2}{6E\,\ell^2} \left\{ \frac{\ell_1 \left[(I_{1\eta^*} + I_{1\zeta^*}) + (I_{1\eta^*} - I_{1\zeta^*}) \cos 2\beta_1 + 2 I_{1\eta^*\zeta^*} \sin 2\beta_1 \right]}{I_{1\eta^*} I_{1\zeta^*} - I_{1\eta^*\zeta^*}^2} \right. \\ &\qquad \left. + \frac{\ell_2 \left[(I_{2\eta^*} + I_{2\zeta^*}) + (I_{2\eta^*} - I_{2\zeta^*}) \cos 2\beta_2 + 2 I_{2\eta^*\zeta^*} \sin 2\beta_2 \right]}{I_{2\eta^*} I_{2\zeta^*} - I_{2\eta^*\zeta^*}^2} \right\} \end{aligned} \tag{A.9}$$

$$\begin{aligned} h_{23} &= \frac{\ell_1\,\ell_2}{3E\,\ell^2} \left(\frac{I_{1\eta}\,\ell_1^2}{I_{1\eta} I_{1\zeta} - I_{1\eta\zeta}^2} - \frac{I_{2\eta}\,\ell_2^2}{I_{2\eta} I_{2\zeta} - I_{2\eta\zeta}^2} \right) \\ &= \frac{\ell_1\,\ell_2}{6E\,\ell^2} \left\{ \frac{\ell_1^2 \left[(I_{1\eta^*} + I_{1\zeta^*}) + (I_{1\eta^*} - I_{1\zeta^*}) \cos 2\beta_1 + 2 I_{1\eta^*\zeta^*} \sin 2\beta_1 \right]}{I_{1\eta^*} I_{1\zeta^*} - I_{1\eta^*\zeta^*}^2} \right. \\ &\qquad \left. - \frac{\ell_2^2 \left[(I_{2\eta^*} + I_{2\zeta^*}) + (I_{2\eta^*} - I_{2\zeta^*}) \cos 2\beta_2 + 2 I_{2\eta^*\zeta^*} \sin 2\beta_2 \right]}{I_{2\eta^*} I_{2\zeta^*} - I_{2\eta^*\zeta^*}^2} \right\} \end{aligned} \tag{A.10}$$

$$
\begin{aligned}
h_{24} &= \frac{\ell_1\,\ell_2}{3E\,\ell^2}\left(\frac{I_{1\eta\zeta}\,\ell_1^2}{I_{1\eta}I_{1\zeta}-I_{1\eta\zeta}^2}-\frac{I_{2\eta\zeta}\,\ell_2^2}{I_{2\eta}I_{2\zeta}-I_{2\eta\zeta}^2}\right)\\
&= -\frac{\ell_1\,\ell_2}{6E\,\ell^2}\left\{\frac{\ell_1^2\left[(I_{1\eta^*}-I_{1\zeta^*})\sin 2\beta_1-2I_{1\eta^*\zeta^*}\cos 2\beta_1\right]}{I_{1\eta^*}I_{1\zeta^*}-I_{1\eta^*\zeta^*}^2}\right.\\
&\qquad\left.-\frac{\ell_2^2\left[(I_{2\eta^*}-I_{2\zeta^*})\sin 2\beta_2-2I_{2\eta^*\zeta^*}\cos 2\beta_2\right]}{I_{2\eta^*}I_{2\zeta^*}-I_{2\eta^*\zeta^*}^2}\right\}
\end{aligned}
\tag{A.11}
$$

$$
\begin{aligned}
h_{33} &= \frac{1}{3E\,\ell^2}\left(\frac{I_{1\eta}\,\ell_1^3}{I_{1\eta}I_{1\zeta}-I_{1\eta\zeta}^2}+\frac{I_{2\eta}\,\ell_2^3}{I_{2\eta}I_{2\zeta}-I_{2\eta\zeta}^2}\right)\\
&= \frac{1}{6E\,\ell^2}\left\{\frac{\ell_1^3\left[(I_{1\eta^*}+I_{1\zeta^*})+(I_{1\eta^*}-I_{1\zeta^*})\cos 2\beta_1+2I_{1\eta^*\zeta^*}\sin 2\beta_1\right]}{I_{1\eta^*}I_{1\zeta^*}-I_{1\eta^*\zeta^*}^2}\right.\\
&\qquad\left.+\frac{\ell_2^3\left[(I_{2\eta^*}+I_{2\zeta^*})+(I_{2\eta^*}-I_{2\zeta^*})\cos 2\beta_2+2I_{2\eta^*\zeta^*}\sin 2\beta_2\right]}{I_{2\eta^*}I_{2\zeta^*}-I_{2\eta^*\zeta^*}^2}\right\}
\end{aligned}
\tag{A.12}
$$

$$
\begin{aligned}
h_{34} &= \frac{1}{3E\,\ell^2}\left(\frac{I_{1\eta\zeta}\,\ell_1^3}{I_{1\eta}I_{1\zeta}-I_{1\eta\zeta}^2}+\frac{I_{2\eta\zeta}\,\ell_2^3}{I_{2\eta}I_{2\zeta}-I_{2\eta\zeta}^2}\right)\\
&= -\frac{1}{6E\,\ell^2}\left\{\frac{\ell_1^3\left[(I_{1\eta^*}-I_{1\zeta^*})\sin 2\beta_1-2I_{1\eta^*\zeta^*}\cos 2\beta_1\right]}{I_{1\eta^*}I_{1\zeta^*}-I_{1\eta^*\zeta^*}^2}\right.\\
&\qquad\left.+\frac{\ell_2^3\left[(I_{2\eta^*}-I_{2\zeta^*})\sin 2\beta_2-2I_{2\eta^*\zeta^*}\cos 2\beta_2\right]}{I_{2\eta^*}I_{2\zeta^*}-I_{2\eta^*\zeta^*}^2}\right\}
\end{aligned}
\tag{A.13}
$$

$$
\begin{aligned}
h_{44} &= \frac{1}{3E\,\ell^2}\left(\frac{I_{1\zeta}\,\ell_1^3}{I_{1\eta}I_{1\zeta}-I_{1\eta\zeta}^2}+\frac{I_{2\zeta}\,\ell_2^3}{I_{2\eta}I_{2\zeta}-I_{2\eta\zeta}^2}\right)\\
&= \frac{1}{6E\,\ell^2}\left\{\frac{\ell_1^3\left[(I_{1\eta^*}+I_{1\zeta^*})-(I_{1\eta^*}-I_{1\zeta^*})\cos 2\beta_1-2I_{1\eta^*\zeta^*}\sin 2\beta_1\right]}{I_{1\eta^*}I_{1\zeta^*}-I_{1\eta^*\zeta^*}^2}\right.\\
&\qquad\left.+\frac{\ell_2^3\left[(I_{2\eta^*}+I_{2\zeta^*})-(I_{2\eta^*}-I_{2\zeta^*})\cos 2\beta_2-2I_{2\eta^*\zeta^*}\sin 2\beta_2\right]}{I_{2\eta^*}I_{2\zeta^*}-I_{2\eta^*\zeta^*}^2}\right\}
\end{aligned}
\tag{A.14}
$$

Furthermore, the stiffness matrix can be obtained as inverse of the flexibility matrix, hence

$$
\boldsymbol{C}_W = \boldsymbol{H}^{-1} = \begin{bmatrix} c_{11} & c_{12} & c_{13} & c_{14}\\ c_{12} & c_{22} & c_{23} & c_{24}\\ c_{13} & c_{23} & c_{33} & c_{34}\\ c_{14} & c_{24} & c_{34} & c_{44} \end{bmatrix}
\tag{A.15}
$$

A.2 Differential equations of rotor motion

Based on the Equations (2.77) and (2.81), the complete set of equations of rotor motion can be obtained as follows

$$\begin{aligned}
& m\,\ddot{\zeta}_W + (d_a + d_{11})\,\dot{\zeta}_W + (d_{12} - 2m\dot{\varphi})\,\dot{\eta}_W + d_{13}\,\dot{\varphi}_\zeta + d_{14}\,\dot{\varphi}_\eta \\
&\qquad + \left(c_{11} - m\dot{\varphi}^2\right)\zeta_W + (c_{12} - m\ddot{\varphi} - d_a\dot{\varphi})\,\eta_W + c_{13}\,\varphi_\zeta + c_{14}\,\varphi_\eta \\
&\qquad = m\epsilon\ddot{\varphi}\sin\phi + m\epsilon\dot{\varphi}^2\cos\phi + d_a\epsilon\dot{\varphi}\sin\phi + \ mg\cos\varphi
\end{aligned} \tag{A.16}$$

$$\begin{aligned}
& m\,\ddot{\eta}_W + (d_{12} + 2m\dot{\varphi})\,\dot{\zeta}_W + (d_a + d_{22})\,\dot{\eta}_W + d_{23}\,\dot{\varphi}_\zeta + d_{24}\,\dot{\varphi}_\eta \\
&\qquad + (c_{12} + m\ddot{\varphi} + d_a\dot{\varphi})\,\zeta_W + \left(c_{22} - m\dot{\varphi}^2\right)\eta_W + c_{23}\,\varphi_\zeta + c_{24}\,\varphi_\eta \\
&\qquad = -m\epsilon\ddot{\varphi}\cos\phi + m\epsilon\dot{\varphi}^2\sin\phi - d_a\epsilon\dot{\varphi}\cos\phi - \ mg\sin\varphi
\end{aligned} \tag{A.17}$$

$$\begin{aligned}
& \Theta_a\,\ddot{\varphi}_\zeta + d_{13}\,\dot{\zeta}_W + d_{23}\,\dot{\eta}_W + d_{33}\,\dot{\varphi}_\zeta + (d_{34} + \Theta_p\dot{\varphi} - 2\Theta_a\dot{\varphi})\,\dot{\varphi}_\eta \\
&\qquad + c_{13}\,\zeta_W + c_{23}\,\eta_W + \left(c_{33} + \Theta_p\dot{\varphi}^2 - \Theta_a\dot{\varphi}^2\right)\varphi_\zeta + (c_{34} + \Theta_p\ddot{\varphi} - \Theta_a\ddot{\varphi})\,\varphi_\eta = 0
\end{aligned} \tag{A.18}$$

$$\begin{aligned}
& \Theta_a\,\ddot{\varphi}_\eta + d_{14}\,\dot{\zeta}_W + d_{24}\,\dot{\eta}_W + (d_{34} - \Theta_p\dot{\varphi} + 2\Theta_a\dot{\varphi})\,\dot{\varphi}_\zeta + d_{44}\,\dot{\varphi}_\eta \\
&\qquad + c_{14}\,\zeta_W + c_{24}\,\eta_W + (c_{34} - \Theta_p\ddot{\varphi} + \Theta_a\ddot{\varphi})\,\varphi_\zeta + \left(c_{44} + \Theta_p\dot{\varphi}^2 - \Theta_a\dot{\varphi}^2\right)\varphi_\eta = 0
\end{aligned} \tag{A.19}$$

$$\begin{aligned}
& \Theta_p\,\ddot{\varphi} + (\eta_W + \epsilon\sin\phi)\Big(d_{11}\,\dot{\zeta}_W + d_{12}\,\dot{\eta}_W + d_{13}\,\dot{\varphi}_\zeta + d_{14}\,\dot{\varphi}_\eta c_{11}\,\zeta_W + c_{12}\,\eta_W \\
&\qquad + c_{13}\,\varphi_\zeta + c_{14}\,\varphi_\eta\Big) - (\zeta_W + \epsilon\cos\phi)\Big(d_{12}\,\dot{\zeta}_W + d_{22}\,\dot{\eta}_W + d_{23}\,\dot{\varphi}_\zeta + d_{24}\,\dot{\varphi}_\eta \\
&\qquad c_{12}\,\zeta_W + c_{22}\,\eta_W + c_{23}\,\varphi_\zeta + c_{24}\,\varphi_\eta\Big) = T_a
\end{aligned} \tag{A.20}$$

Appendix B

Anisotropic rotor supported by flexible anisotropic bearings

B.1 Equations of forces in the bearings

The equations of forces that act in the bearings as written in the Equations (2.102) and (2.103) are considered in the fixed reference frame. If the equations are transformed into the rotating reference frame, then

$$
\begin{aligned}
F_{L_1} = &\left[\frac{1}{2}\dot{\zeta}_{L_1}\left(d_{1z}+d_{1y}\right)+\frac{1}{2}\dot{\zeta}_{L_1}\left(d_{1z}-d_{1y}\right)\cos 2\varphi-\frac{1}{2}\dot{\eta}_{L_1}\left(d_{1z}-d_{1y}\right)\sin 2\varphi\right.\\
&-\frac{1}{2}\zeta_{L_1}\dot{\varphi}\left(d_{1z}-d_{1y}\right)\sin 2\varphi+\frac{1}{2}\zeta_{L_1}\left(c_{1z}+c_{1y}\right)+\frac{1}{2}\zeta_{L_1}\left(c_{1z}-c_{1y}\right)\cos 2\varphi\\
&\left.-\frac{1}{2}\eta_{L_1}\dot{\varphi}\left(d_{1z}+d_{1y}\right)-\frac{1}{2}\eta_{L_1}\dot{\varphi}\left(d_{1z}-d_{1y}\right)\cos 2\varphi-\frac{1}{2}\eta_{L_1}\left(c_{1z}-c_{1y}\right)\right]\vec{e}_{\zeta}\\
&-\left[\frac{1}{2}\dot{\zeta}_{L_1}\left(d_{1z}-d_{1y}\right)\sin 2\varphi-\frac{1}{2}\dot{\eta}_{L_1}\left(d_{1z}+d_{1y}\right)+\frac{1}{2}\dot{\eta}_{L_1}\left(d_{1z}-d_{1y}\right)\cos 2\varphi\right.\\
&-\frac{1}{2}\zeta_{L_1}\dot{\varphi}\left(d_{1z}+d_{1y}\right)+\frac{1}{2}\zeta_{L_1}\dot{\varphi}\left(d_{1z}-d_{1y}\right)\cos 2\varphi+\frac{1}{2}\zeta_{L_1}\left(c_{1z}-c_{1y}\right)\sin 2\varphi\\
&\left.-\frac{1}{2}\eta_{L_1}\dot{\varphi}\left(d_{1z}-d_{1y}\right)\sin 2\varphi-\frac{1}{2}\eta_{L_1}\left(c_{1z}+c_{1y}\right)+\frac{1}{2}\eta_{L_1}\left(c_{1z}-c_{1y}\right)\cos 2\varphi\right]\vec{e}_{\eta}
\end{aligned}
\tag{B.1}
$$

$$
\begin{aligned}
F_{L_2} = &\left[\frac{1}{2}\dot{\zeta}_{L_2}\left(d_{1z}+d_{1y}\right)+\frac{1}{2}\dot{\zeta}_{L_2}\left(d_{1z}-d_{1y}\right)\cos 2\varphi-\frac{1}{2}\dot{\eta}_{L_2}\left(d_{1z}-d_{1y}\right)\sin 2\varphi\right.\\
&-\frac{1}{2}\zeta_{L_2}\dot{\varphi}\left(d_{1z}-d_{1y}\right)\sin 2\varphi+\frac{1}{2}\zeta_{L_2}\left(c_{1z}+c_{1y}\right)+\frac{1}{2}\zeta_{L_2}\left(c_{1z}-c_{1y}\right)\cos 2\varphi\\
&\left.-\frac{1}{2}\eta_{L_2}\dot{\varphi}\left(d_{1z}+d_{1y}\right)-\frac{1}{2}\eta_{L_2}\dot{\varphi}\left(d_{1z}-d_{1y}\right)\cos 2\varphi-\frac{1}{2}\eta_{L_2}\left(c_{1z}-c_{1y}\right)\right]\vec{e}_{\zeta}
\end{aligned}
$$

$$\begin{aligned}
&-\Bigg[\frac{1}{2}\dot{\zeta}_{L_2}\left(d_{1z}-d_{1y}\right)\sin 2\varphi-\frac{1}{2}\dot{\eta}_{L_2}\left(d_{1z}+d_{1y}\right)+\frac{1}{2}\dot{\eta}_{L_2}\left(d_{1z}-d_{1y}\right)\cos 2\varphi\\
&-\frac{1}{2}\zeta_{L_2}\dot{\varphi}\left(d_{1z}+d_{1y}\right)+\frac{1}{2}\zeta_{L_2}\dot{\varphi}\left(d_{1z}-d_{1y}\right)\cos 2\varphi+\frac{1}{2}\zeta_{L_2}\left(c_{1z}-c_{1y}\right)\sin 2\varphi\\
&-\frac{1}{2}\eta_{L_2}\dot{\varphi}\left(d_{1z}-d_{1y}\right)\sin 2\varphi-\frac{1}{2}\eta_{L_2}\left(c_{1z}+c_{1y}\right)+\frac{1}{2}\eta_{L_2}\left(c_{1z}-c_{1y}\right)\cos 2\varphi\Bigg]\vec{e}_\eta
\end{aligned} \tag{B.2}$$

B.2 Differential equations of rotor motion

Based on the Equations (2.111) and (2.115), the complete set of equations of rotor motion can be obtained,

in ζ-direction is

$$\begin{aligned}
&m\,\ddot{\zeta}_W+\left(d_a+d_{11}\right)\dot{\zeta}_W+\left(d_{12}-2m\dot{\varphi}\right)\dot{\eta}_W+d_{13}\,\dot{\varphi}_\zeta+d_{14}\,\dot{\varphi}_\eta-\left(\frac{\ell_2}{\ell}d_{11}+\frac{1}{\ell}d_{14}\right)\dot{\zeta}_{L_1}\\
&\quad-\left(\frac{\ell_2}{\ell}d_{12}-\frac{1}{\ell}d_{13}\right)\dot{\eta}_{L_1}-\left(\frac{\ell_1}{\ell}d_{11}-\frac{1}{\ell}d_{14}\right)\dot{\zeta}_{L_2}-\left(\frac{\ell_1}{\ell}d_{12}+\frac{1}{\ell}d_{13}\right)\dot{\eta}_{L_2}\\
&\quad+\left(c_{11}-m\dot{\varphi}^2\right)\zeta_W+\left(c_{12}-m\ddot{\varphi}-d_a\dot{\varphi}\right)\eta_W+c_{13}\,\varphi_\zeta+c_{14}\,\varphi_\eta\\
&\quad-\left(\frac{\ell_2}{\ell}c_{11}+\frac{1}{\ell}c_{14}\right)\zeta_{L_1}-\left(\frac{\ell_2}{\ell}c_{12}-\frac{1}{\ell}c_{13}\right)\eta_{L_1}-\left(\frac{\ell_1}{\ell}c_{11}-\frac{1}{\ell}c_{14}\right)\zeta_{L_2}\\
&\quad-\left(\frac{\ell_1}{\ell}c_{12}+\frac{1}{\ell}c_{13}\right)\eta_{L_2}=m\epsilon\ddot{\varphi}\sin\phi+m\epsilon\dot{\varphi}^2\cos\phi+d_a\epsilon\dot{\varphi}\sin\phi+\ mg\cos\varphi
\end{aligned} \tag{B.3}$$

and in η-direction is

$$\begin{aligned}
&m\,\ddot{\eta}_W+\left(d_{12}+2m\dot{\varphi}\right)\dot{\zeta}_W+\left(d_a+d_{22}\right)\dot{\eta}_W+d_{23}\,\dot{\varphi}_\zeta+d_{24}\,\dot{\varphi}_\eta-\left(\frac{\ell_2}{\ell}d_{12}+\frac{1}{\ell}d_{24}\right)\dot{\zeta}_{L_1}\\
&\quad-\left(\frac{\ell_2}{\ell}d_{22}-\frac{1}{\ell}d_{23}\right)\dot{\eta}_{L_1}-\left(\frac{\ell_1}{\ell}d_{12}-\frac{1}{\ell}d_{24}\right)\dot{\zeta}_{L_2}-\left(\frac{\ell_1}{\ell}d_{22}+\frac{1}{\ell}d_{23}\right)\dot{\eta}_{L_2}\\
&\quad+\left(c_{12}+m\ddot{\varphi}+d_a\dot{\varphi}\right)\zeta_W+\left(c_{22}-m\dot{\varphi}^2\right)\eta_W+c_{23}\,\varphi_\zeta+c_{24}\,\varphi_\eta\\
&\quad-\left(\frac{\ell_2}{\ell}c_{12}+\frac{1}{\ell}c_{24}\right)\zeta_{L_1}-\left(\frac{\ell_2}{\ell}c_{22}-\frac{1}{\ell}c_{23}\right)\eta_{L_1}-\left(\frac{\ell_1}{\ell}c_{12}-\frac{1}{\ell}c_{24}\right)\zeta_{L_2}\\
&\quad-\left(\frac{\ell_1}{\ell}c_{22}+\frac{1}{\ell}c_{23}\right)\eta_{L_2}=-m\epsilon\ddot{\varphi}\cos\phi+m\epsilon\dot{\varphi}^2\sin\phi-d_a\epsilon\dot{\varphi}\cos\phi-\ mg\sin\varphi
\end{aligned} \tag{B.4}$$

Furthermore, two equations in rotary direction φ_ζ and φ_η are

$$\begin{aligned}
&\Theta_a\,\ddot{\varphi}_\zeta+d_{13}\,\dot{\zeta}_W+d_{23}\,\dot{\eta}_W+d_{33}\,\dot{\varphi}_\zeta+\left(d_{34}+\Theta_p\dot{\varphi}-2\Theta_a\dot{\varphi}\right)\dot{\varphi}_\eta\\
&\quad-\left(\frac{\ell_2}{\ell}d_{13}+\frac{1}{\ell}d_{34}\right)\dot{\zeta}_{L_1}-\left(\frac{\ell_2}{\ell}d_{23}-\frac{1}{\ell}d_{33}\right)\dot{\eta}_{L_1}-\left(\frac{\ell_1}{\ell}d_{13}-\frac{1}{\ell}d_{34}\right)\dot{\zeta}_{L_2}
\end{aligned}$$

$$
\begin{aligned}
&-\left(\frac{\ell_1}{\ell}d_{23}+\frac{1}{\ell}d_{33}\right)\dot{\eta}_{L_2}+c_{13}\,\zeta_W+c_{23}\,\eta_W+\left(c_{33}+\Theta_p\dot{\varphi}^2-\Theta_a\dot{\varphi}^2\right)\varphi_\zeta\\
&+\left(c_{34}+\Theta_p\ddot{\varphi}-\Theta_a\ddot{\varphi}\right)\varphi_\eta-\left(\frac{\ell_2}{\ell}c_{13}+\frac{1}{\ell}c_{34}\right)\zeta_{L_1}-\left(\frac{\ell_2}{\ell}c_{23}-\frac{1}{\ell}c_{33}\right)\eta_{L_1}\\
&-\left(\frac{\ell_1}{\ell}d_{13}-\frac{1}{\ell}d_{34}\right)\zeta_{L_2}-\left(\frac{\ell_1}{\ell}c_{23}+\frac{1}{\ell}c_{33}\right)\eta_{L_2}=0
\end{aligned}
\tag{B.5}
$$

$$
\begin{aligned}
&\Theta_a\,\ddot{\varphi}_\eta+d_{14}\,\dot{\zeta}_W+d_{24}\,\dot{\eta}_W+\left(d_{34}-\Theta_p\dot{\varphi}+2\Theta_a\dot{\varphi}\right)\dot{\varphi}_\zeta+d_{44}\,\dot{\varphi}_\eta\\
&\quad-\left(\frac{\ell_2}{\ell}d_{14}+\frac{1}{\ell}d_{44}\right)\dot{\zeta}_{L_1}-\left(\frac{\ell_2}{\ell}d_{24}-\frac{1}{\ell}d_{34}\right)\dot{\eta}_{L_1}-\left(\frac{\ell_1}{\ell}d_{14}-\frac{1}{\ell}d_{44}\right)\dot{\zeta}_{L_2}\\
&\quad-\left(\frac{\ell_1}{\ell}d_{24}+\frac{1}{\ell}d_{34}\right)\dot{\eta}_{L_2}+c_{14}\,\zeta_W+c_{24}\,\eta_W+\left(c_{34}-\Theta_p\ddot{\varphi}+\Theta_a\ddot{\varphi}\right)\varphi_\zeta\\
&\quad+\left(c_{44}+\Theta_p\dot{\varphi}^2-\Theta_a\dot{\varphi}^2\right)\varphi_\eta-\left(\frac{\ell_2}{\ell}c_{14}+\frac{1}{\ell}c_{44}\right)\zeta_{L_1}-\left(\frac{\ell_2}{\ell}c_{24}-\frac{1}{\ell}c_{34}\right)\eta_{L_1}\\
&\quad-\left(\frac{\ell_1}{\ell}c_{14}-\frac{1}{\ell}c_{44}\right)\zeta_{L_2}-\left(\frac{\ell_1}{\ell}c_{24}+\frac{1}{\ell}c_{34}\right)\eta_{L_2}=0
\end{aligned}
\tag{B.6}
$$

Furthermore, by applying the four differential equations from Equations (2.94)-(2.97) with the two equations in Appendix (B.1) above for ζ and η-direction, hence the equations of the bearing in the left side of the rotor in ζ-direction are obtained as following

$$
\begin{aligned}
&-\left(\frac{\ell_2}{\ell}d_{11}+\frac{1}{\ell}d_{14}\right)\dot{\zeta}_W-\left(\frac{\ell_2}{\ell}d_{12}+\frac{1}{\ell}d_{24}\right)\dot{\eta}_W-\left(\frac{\ell_2}{\ell}d_{13}+\frac{1}{\ell}d_{34}\right)\dot{\varphi}_\zeta\\
&\quad-\left(\frac{\ell_2}{\ell}d_{14}+\frac{1}{\ell}d_{44}\right)\dot{\varphi}_\eta+\left[\frac{\ell_2^2}{\ell^2}d_{11}+\frac{2\ell_2}{\ell^2}d_{14}+\frac{1}{\ell^2}d_{44}+\frac{1}{2}\left(d_{1z}+d_{1y}\right)\right.\\
&\quad\left.+\frac{1}{2}\left(d_{1z}-d_{1y}\right)\cos 2\varphi\right]\dot{\zeta}_{L_1}+\left[\frac{\ell_2^2}{\ell^2}d_{12}-\frac{\ell_2}{\ell^2}d_{13}+\frac{\ell_2}{\ell^2}d_{24}-\frac{1}{\ell^2}d_{34}\right.\\
&\quad\left.-\frac{1}{2}\left(d_{1z}-d_{1y}\right)\sin 2\varphi\right]\dot{\eta}_{L_1}+\left[\frac{\ell_1\,\ell_2}{\ell^2}d_{11}+\left(\frac{\ell_1-\ell_2}{\ell^2}\right)d_{14}-\frac{1}{\ell^2}d_{44}\right]\dot{\zeta}_{L_2}\\
&\quad+\left(\frac{\ell_1\,\ell_2}{\ell^2}d_{12}+\frac{\ell_2}{\ell^2}d_{13}+\frac{\ell_1}{\ell^2}d_{24}+\frac{1}{\ell^2}d_{34}\right)\dot{\eta}_{L_2}\\
&\quad-\left(\frac{\ell_2}{\ell}c_{11}+\frac{1}{\ell}c_{14}\right)\zeta_W-\left(\frac{\ell_2}{\ell}c_{12}+\frac{1}{\ell}c_{24}\right)\eta_W-\left(\frac{\ell_2}{\ell}c_{13}+\frac{1}{\ell}c_{34}\right)\varphi_\zeta\\
&\quad-\left(\frac{\ell_2}{\ell}c_{14}+\frac{1}{\ell}c_{44}\right)\varphi_\eta+\left[\frac{\ell_2^2}{\ell^2}c_{11}+\frac{2\ell_2}{\ell^2}c_{14}+\frac{1}{\ell^2}c_{44}+\frac{1}{2}\left(c_{1z}+c_{1y}\right)\right.\\
&\quad\left.+\frac{1}{2}\left(c_{1z}-c_{1y}\right)\cos 2\varphi-\frac{1}{2}\dot{\varphi}\left(d_{1z}-d_{1y}\right)\sin 2\varphi\right]\zeta_{L_1}\\
&\quad+\left[\frac{\ell_2^2}{\ell^2}c_{12}-\frac{\ell_2}{\ell^2}c_{13}+\frac{\ell_2}{\ell^2}c_{24}-\frac{1}{\ell^2}c_{34}-\frac{1}{2}\dot{\varphi}\left(d_{1z}+d_{1y}\right)-\frac{1}{2}\dot{\varphi}\left(d_{1z}-d_{1y}\right)\cos 2\varphi\right.
\end{aligned}
$$

$$
\begin{aligned}
&-\frac{1}{2}\left(c_{1z}-c_{1y}\right)\sin 2\varphi\Bigg]\eta_{L_1}+\left[\frac{\ell_1\,\ell_2}{\ell^2}c_{11}+\left(\frac{\ell_1-\ell_2}{\ell^2}\right)c_{14}-\frac{1}{\ell^2}c_{44}\right]\zeta_{L_2}\\
&+\left(\frac{\ell_1\,\ell_2}{\ell^2}c_{12}+\frac{\ell_2}{\ell^2}c_{13}+\frac{\ell_1}{\ell^2}c_{24}+\frac{1}{\ell^2}c_{34}\right)\eta_{L_2}=0
\end{aligned}
\tag{B.7}
$$

The equation in the bearing in the left side of the rotor in η-direction is

$$
\begin{aligned}
&-\left(\frac{\ell_2}{\ell}d_{12}-\frac{1}{\ell}d_{13}\right)\dot{\zeta}_W-\left(\frac{\ell_2}{\ell}d_{22}-\frac{1}{\ell}d_{23}\right)\dot{\eta}_W-\left(\frac{\ell_2}{\ell}d_{23}-\frac{1}{\ell}d_{33}\right)\dot{\varphi}_\zeta\\
&\quad-\left(\frac{\ell_2}{\ell}d_{24}-\frac{1}{\ell}d_{34}\right)\dot{\varphi}_\eta+\left[\frac{\ell_2^2}{\ell^2}d_{12}+\frac{\ell_2}{\ell^2}d_{24}-\frac{\ell_2}{\ell^2}d_{13}-\frac{1}{\ell^2}d_{34}-\frac{1}{2}\left(d_{1z}-d_{1y}\right)\sin 2\varphi\right]\dot{\zeta}_{L_1}\\
&\quad+\left[\frac{\ell_2^2}{\ell^2}d_{22}-\frac{2\ell_2}{\ell^2}d_{23}+\frac{1}{\ell^2}d_{33}+\frac{1}{2}\left(d_{1z}+d_{1y}\right)-\frac{1}{2}\left(d_{1z}-d_{1y}\right)\cos 2\varphi\right]\dot{\eta}_{L_1}\\
&\quad+\left(\frac{\ell_1\,\ell_2}{\ell^2}d_{12}-\frac{\ell_2}{\ell^2}d_{24}-\frac{\ell_1}{\ell^2}d_{13}+\frac{1}{\ell^2}d_{34}\right)\dot{\zeta}_{L_2}+\left(\frac{\ell_1\,\ell_2}{\ell^2}d_{22}+\frac{\ell_2}{\ell^2}d_{23}-\frac{\ell_1}{\ell^2}d_{23}-\frac{1}{\ell^2}d_{33}\right)\dot{\eta}_{L_2}\\
&\quad-\left(\frac{\ell_2}{\ell}c_{12}-\frac{1}{\ell}c_{13}\right)\zeta_W-\left(\frac{\ell_2}{\ell}c_{22}-\frac{1}{\ell}c_{23}\right)\eta_W-\left(\frac{\ell_2}{\ell}c_{23}-\frac{1}{\ell}c_{33}\right)\varphi_\zeta\\
&\quad-\left(\frac{\ell_2}{\ell}c_{24}-\frac{1}{\ell}c_{34}\right)\varphi_\eta+\Bigg[\frac{\ell_2^2}{\ell^2}c_{12}+\frac{\ell_2}{\ell^2}c_{24}-\frac{\ell_2}{\ell^2}c_{13}-\frac{1}{\ell^2}c_{34}+\frac{1}{2}\dot{\varphi}\left(d_{1z}+d_{1y}\right)\\
&\quad-\frac{1}{2}\dot{\varphi}\left(d_{1z}-d_{1y}\right)\cos 2\varphi-\frac{1}{2}\left(c_{1z}-c_{1y}\right)\sin 2\varphi\Bigg]\zeta_{L_1}\\
&\quad+\Bigg[\frac{\ell_2^2}{\ell^2}c_{22}-\frac{\ell_2}{\ell^2}c_{23}-\frac{\ell_2}{\ell^2}c_{23}+\frac{1}{\ell^2}c_{33}+\frac{1}{2}\dot{\varphi}\left(d_{1z}-d_{1y}\right)\sin 2\varphi+\frac{1}{2}\left(c_{1z}+c_{1y}\right)\\
&\quad-\frac{1}{2}\left(c_{1z}-c_{1y}\right)\cos 2\varphi\Bigg]\eta_{L_1}+\left(\frac{\ell_1\,\ell_2}{\ell^2}c_{12}-\frac{\ell_2}{\ell^2}c_{24}-\frac{\ell_1}{\ell^2}c_{13}+\frac{1}{\ell^2}c_{34}\right)\zeta_{L_2}\\
&\quad+\left(\frac{\ell_1\,\ell_2}{\ell^2}c_{22}+\frac{\ell_2}{\ell^2}c_{23}-\frac{\ell_1}{\ell^2}c_{23}-\frac{1}{\ell^2}c_{33}\right)\eta_{L_2}=0
\end{aligned}
\tag{B.8}
$$

The equation in the bearing in the right side of the rotor in ζ-direction is

$$
\begin{aligned}
&-\left(\frac{\ell_1}{\ell}d_{11}-\frac{1}{\ell}d_{14}\right)\dot{\zeta}_W-\left(\frac{\ell_1}{\ell}d_{12}-\frac{1}{\ell}d_{24}\right)\dot{\eta}_W-\left(\frac{\ell_1}{\ell}d_{13}-\frac{1}{\ell}d_{34}\right)\dot{\varphi}_\zeta\\
&\quad-\left(\frac{\ell_1}{\ell}d_{14}-\frac{1}{\ell}d_{44}\right)\dot{\varphi}_\eta+\left(\frac{\ell_1\,\ell_2}{\ell^2}d_{11}+\frac{\ell_1}{\ell^2}d_{14}-\frac{\ell_2}{\ell^2}d_{14}-\frac{1}{\ell^2}d_{44}\right)\dot{\zeta}_{L_1}\\
&\quad+\left(\frac{\ell_1\,\ell_2}{\ell^2}d_{12}-\frac{\ell_1}{\ell^2}d_{13}-\frac{\ell_2}{\ell^2}d_{24}+\frac{1}{\ell^2}d_{34}\right)\dot{\eta}_{L_1}\\
&\quad+\left[\frac{\ell_1^2}{\ell^2}d_{11}-\frac{2\ell_1}{\ell^2}d_{14}+\frac{1}{\ell^2}d_{44}+\frac{1}{2}\left(d_{2z}+d_{2y}\right)+\frac{1}{2}\left(d_{2z}-d_{2y}\right)\cos 2\varphi\right]\dot{\zeta}_{L_2}\\
&\quad+\left[\frac{\ell_1^2}{\ell^2}d_{12}+\frac{\ell_1}{\ell^2}d_{13}-\frac{\ell_1}{\ell^2}d_{24}-\frac{1}{\ell^2}d_{34}-\frac{1}{2}\left(d_{2z}-d_{2y}\right)\sin 2\varphi\right]\dot{\eta}_{L_2}
\end{aligned}
$$

$$
\begin{aligned}
&-\left(\frac{\ell_1}{\ell}c_{11}-\frac{1}{\ell}c_{14}\right)\zeta_W-\left(\frac{\ell_1}{\ell}c_{12}-\frac{1}{\ell}c_{24}\right)\eta_W-\left(\frac{\ell_1}{\ell}c_{13}-\frac{1}{\ell}c_{34}\right)\varphi_\zeta\\
&-\left(\frac{\ell_2}{\ell}c_{14}+\frac{1}{\ell}c_{44}\right)\varphi_\eta+\left[\frac{\ell_1\,\ell_2}{\ell^2}c_{11}+\left(\frac{\ell_1-\ell_2}{\ell^2}\right)c_{14}-\frac{2}{\ell^2}c_{44}\right]\zeta_{L_1}\\
&+\left(\frac{\ell_1\,\ell_2}{\ell^2}c_{12}-\frac{\ell_1}{\ell^2}c_{13}-\frac{\ell_2}{\ell^2}c_{24}+\frac{1}{\ell^2}c_{34}\right)\eta_{L_1}\\
&+\left[\frac{\ell_1^2}{\ell^2}c_{11}-\frac{2\ell_1}{\ell^2}c_{14}+\frac{1}{\ell^2}c_{44}+\frac{1}{2}\left(c_{2z}+c_{2y}\right)+\frac{1}{2}\left(c_{2z}-c_{2y}\right)\cos 2\varphi\right.\\
&\left.-\frac{1}{2}\dot{\varphi}\left(d_{2z}-d_{2y}\right)\sin 2\varphi\right]\zeta_{L_2}+\left[\frac{\ell_1^2}{\ell^2}c_{12}+\frac{\ell_1}{\ell^2}c_{13}-\frac{\ell_1}{\ell^2}c_{24}-\frac{1}{\ell^2}c_{34}\right.\\
&\left.-\frac{1}{2}\dot{\varphi}\left(d_{2z}+d_{2y}\right)-\frac{1}{2}\dot{\varphi}\left(d_{2z}-d_{2y}\right)\cos 2\varphi-\frac{1}{2}\left(c_{2z}-c_{2y}\right)\sin 2\varphi\right]\eta_{L_2}=0
\end{aligned}
\tag{B.9}
$$

and the equation in the bearing in the right side of the rotor in η-direction is

$$
\begin{aligned}
&-\left(\frac{\ell_1}{\ell}d_{12}+\frac{1}{\ell}d_{13}\right)\dot{\zeta}_W-\left(\frac{\ell_1}{\ell}d_{22}+\frac{1}{\ell}d_{23}\right)\dot{\eta}_W-\left(\frac{\ell_1}{\ell}d_{23}+\frac{1}{\ell}d_{33}\right)\dot{\varphi}_\zeta\\
&-\left(\frac{\ell_1}{\ell}d_{24}+\frac{1}{\ell}d_{34}\right)\dot{\varphi}_\eta+\left(\frac{\ell_1\,\ell_2}{\ell^2}d_{12}+\frac{\ell_1}{\ell^2}d_{24}+\frac{\ell_2}{\ell^2}d_{13}+\frac{1}{\ell^2}d_{34}\right)\dot{\zeta}_{L_1}\\
&+\left[\frac{\ell_1\,\ell_2}{\ell^2}d_{22}-\left(\frac{\ell_1-\ell_2}{\ell^2}\right)d_{23}-\frac{1}{\ell^2}d_{33}\right]\dot{\eta}_{L_1}\\
&+\left[\frac{\ell_1^2}{\ell^2}d_{12}-\frac{\ell_1}{\ell^2}d_{24}+\frac{\ell_1}{\ell^2}d_{13}-\frac{1}{\ell^2}d_{34}-\frac{1}{2}\left(d_{2z}-d_{2y}\right)\sin 2\varphi\right]\dot{\zeta}_{L_2}\\
&+\left[\frac{\ell_1^2}{\ell^2}d_{22}+\frac{2\ell_1}{\ell^2}d_{23}+\frac{1}{\ell^2}d_{33}+\frac{1}{2}\left(d_{2z}+d_{2y}\right)-\frac{1}{2}\left(d_{2z}-d_{2y}\right)\cos 2\varphi\right]\dot{\eta}_{L_2}\\
&-\left(\frac{\ell_1}{\ell}c_{12}+\frac{1}{\ell}c_{13}\right)\zeta_W-\left(\frac{\ell_1}{\ell}c_{22}+\frac{1}{\ell}c_{23}\right)\eta_W-\left(\frac{\ell_1}{\ell}c_{23}+\frac{1}{\ell}c_{33}\right)\varphi_\zeta\\
&-\left(\frac{\ell_1}{\ell}c_{24}+\frac{1}{\ell}c_{34}\right)\varphi_\eta+\left[\frac{\ell_1\,\ell_2}{\ell^2}c_{12}+\frac{\ell_1}{\ell^2}c_{24}+\frac{\ell_2}{\ell^2}c_{13}+\frac{1}{\ell^2}c_{34}\right]\zeta_{L_1}\\
&+\left[\frac{\ell_1\,\ell_2}{\ell^2}c_{22}-\frac{\ell_1}{\ell^2}c_{23}+\frac{\ell_2}{\ell^2}c_{23}-\frac{1}{\ell^2}c_{33}\right]\eta_{L_1}+\left[\frac{\ell_1^2}{\ell^2}c_{12}-\frac{\ell_1}{\ell^2}c_{24}+\frac{\ell_1}{\ell^2}c_{13}-\frac{1}{\ell^2}c_{34}\right.\\
&\left.+\frac{1}{2}\dot{\varphi}\left(d_{2z}+d_{2y}\right)-\frac{1}{2}\dot{\varphi}\left(d_{2z}-d_{2y}\right)\cos 2\varphi-\frac{1}{2}\left(c_{2z}-c_{2y}\right)\sin 2\varphi\right]\zeta_{L_2}\\
&+\left[\frac{\ell_1^2}{\ell^2}c_{22}+\frac{\ell_1}{\ell^2}c_{23}+\frac{\ell_1}{\ell^2}c_{23}+\frac{1}{\ell^2}c_{33}+\frac{1}{2}\dot{\varphi}\left(d_{2z}-d_{2y}\right)\sin 2\varphi+\frac{1}{2}\left(c_{2z}+c_{2y}\right)\right.\\
&\left.-\frac{1}{2}\left(c_{2z}-c_{2y}\right)\cos 2\varphi\right]\eta_{L_2}=0
\end{aligned}
\tag{B.10}
$$

Furthermore, the equation of the rotor with the polar mass moment of inertia is

$$
\begin{aligned}
\Theta_p\,\ddot{\varphi} + \left(\eta_W - \frac{\ell_2}{\ell}\eta_{L_1} - \frac{\ell_1}{\ell}\eta_{L_2} + \epsilon\sin\phi\right) \Big[& d_{11}\,\dot{\zeta}_W + d_{12}\,\dot{\eta}_W + d_{13}\,\dot{\varphi}_\zeta + d_{14}\,\dot{\varphi}_\eta \\
& - \left(\frac{\ell_2}{\ell}d_{11} + \frac{1}{\ell}d_{14}\right)\dot{\zeta}_{L_1} - \left(\frac{\ell_2}{\ell}d_{12} - \frac{1}{\ell}d_{13}\right)\dot{\eta}_{L_1} - \left(\frac{\ell_1}{\ell}d_{11} - \frac{1}{\ell}d_{14}\right)\dot{\zeta}_{L_2} \\
& - \left(\frac{\ell_1}{\ell}d_{12} + \frac{1}{\ell}d_{13}\right)\dot{\eta}_{L_2} + c_{11}\,\zeta_W + c_{12}\,\eta_W + c_{13}\,\varphi_\zeta + c_{14}\,\varphi_\eta \\
& - \left(\frac{\ell_2}{\ell}c_{11} + \frac{1}{\ell}c_{14}\right)\zeta_{L_1} - \left(\frac{\ell_2}{\ell}c_{12} - \frac{1}{\ell}c_{13}\right)\eta_{L_1} - \left(\frac{\ell_1}{\ell}c_{11} - \frac{1}{\ell}c_{14}\right)\zeta_{L_2} \\
& - \left(\frac{\ell_1}{\ell}c_{12} + \frac{1}{\ell}c_{13}\right)\eta_{L_2}\Big] \\
& - \left(\zeta_W - \frac{\ell_2}{\ell}\zeta_{L_1} - \frac{\ell_1}{\ell}\zeta_{L_2} + \epsilon\cos\phi\right)\Big[d_{12}\,\dot{\zeta}_W + d_{22}\,\dot{\eta}_W + d_{23}\,\dot{\varphi}_\zeta + d_{24}\,\dot{\varphi}_\eta \\
& - \left(\frac{\ell_2}{\ell}d_{12} + \frac{1}{\ell}d_{24}\right)\dot{\zeta}_{L_1} - \left(\frac{\ell_2}{\ell}d_{22} - \frac{1}{\ell}d_{23}\right)\dot{\eta}_{L_1} - \left(\frac{\ell_1}{\ell}d_{12} - \frac{1}{\ell}d_{24}\right)\dot{\zeta}_{L_2} \\
& - \left(\frac{\ell_1}{\ell}d_{22} + \frac{1}{\ell}d_{23}\right)\dot{\eta}_{L_2} + c_{12}\,\zeta_W + c_{22}\,\eta_W + c_{23}\,\varphi_\zeta + c_{24}\,\varphi_\eta \\
& - \left(\frac{\ell_2}{\ell}c_{12} + \frac{1}{\ell}c_{24}\right)\zeta_{L_1} - \left(\frac{\ell_2}{\ell}c_{22} - \frac{1}{\ell}c_{23}\right)\eta_{L_1} - \left(\frac{\ell_1}{\ell}c_{12} - \frac{1}{\ell}c_{24}\right)\zeta_{L_2}\Big] \\
& - \left(\frac{\ell_1}{\ell}c_{22} + \frac{1}{\ell}c_{23}\right)\eta_{L_2} = T_a
\end{aligned}
\tag{B.11}
$$

Appendix C

Tables of stability investigation

Table C.1: Identified paramaters of the rotor cases with the coefficient of element anisotropy at $\mu_W = 0.2$

Parameter	Unit	Model-5	Model-6	Model-7	Model-8	Model-9	Model-10
Natural frequency, $\omega_{1\ at\ \Omega=0}$	[rad/s]	212.41	213.28	215.72	222.90	217.76	214.63
Natural frequency, $\omega_{2\ at\ \Omega=0}$	[rad/s]	260.15	258.50	254.18	243.56	250.99	256.16
Natural frequency, $\omega_{3\ at\ \Omega=0}$	[rad/s]	790.11	798.11	820.30	847.61	808.83	795.27
Natural frequency, $\omega_{4\ at\ \Omega=0}$	[rad/s]	967.69	954.35	921.46	884.74	934.71	956.91
Lower boundary of 1^{st} unstable area	[rad/s]	220.31	221.37	224.34	233.20	226.44	222.78
Upper boundary of 1^{st} unstable area	[rad/s]	269.82	267.87	262.79	250.43	259.72	265.55
Width of 1^{st} unstable area	[rad/s]	49.51	46.50	38.45	17.23	33.28	42.77
Shifting of 1^{st} lower boundary due to ω_1	[%]	3.72	3.79	4.00	4.62	3.99	3.80
Shifting of 1^{st} upper boundary due to ω_2	[%]	3.72	3.62	3.39	2.82	3.48	3.67
Lower boundary of 2^{nd} unstable area	[rad/s]	-	580.02	570.67	570.16	579.54	-
Upper boundary of 2^{nd} unstable area	[rad/s]	-	608.00	619.06	618.19	607.28	-
Width of 2^{nd} unstable area	[rad/s]	-	27.98	48.39	48.03	27.74	-
Lower boundary of 3^{rd} unstable area	[rad/s]	874.92	881.78	900.15	947.96	903.82	885.43
Upper boundary of 3^{rd} unstable area	[rad/s]	1071.55	1063.94	1042.95	984.08	1032.37	1055.55
Width of 3^{rd} unstable area	[rad/s]	196.63	182.16	142.80	36.12	128.55	170.12
Shifting of 3^{rd} lower boundary due to ω_3	[%]	10.73	10.48	9.73	11.84	11.74	11.34
Shifting of 3^{rd} upper boundary due to ω_4	[%]	10.73	11.48	13.18	11.23	10.45	10.31

Table C.2: Identified paramaters of the rotor cases with the coefficient of element anisotropy at $\mu_W = 0.3$

Parameter	Unit	Model-5	Model-6	Model-7	Model-8	Model-9	Model-10
Natural frequency, $\omega_{1\ at\ \Omega=0}$	[rad/s]	180.97	181.99	184.88	193.65	187.35	183.60
Natural frequency, $\omega_{2\ at\ \Omega=0}$	[rad/s]	246.63	243.90	236.99	221.20	232.16	240.19
Natural frequency, $\omega_{3\ at\ \Omega=0}$	[rad/s]	673.17	683.68	712.54	743.09	695.67	679.14
Natural frequency, $\omega_{4\ at\ \Omega=0}$	[rad/s]	917.37	893.53	842.21	795.25	864.33	898.87
Lower boundary of 1^{st} unstable area	[rad/s]	187.70	188.95	192.49	203.47	195.07	190.64
Upper boundary of 1^{st} unstable area	[rad/s]	255.79	252.62	244.62	226.49	240.05	249.02
Width of 1^{st} unstable area	[rad/s]	68.09	63.67	52.13	23.02	44.98	58.38
Shifting of 1^{st} lower boundary due to ω_1	[%]	3.72	3.82	4.12	5.07	4.12	3.83
Shifting of 1^{st} upper boundary due to ω_2	[%]	3.71	3.58	3.22	2.39	3.40	3.68
Lower boundary of 2^{nd} unstable area	[rad/s]	-	510.72	498.52	497.61	509.79	-
Upper boundary of 2^{nd} unstable area	[rad/s]	-	549.07	564.75	562.70	547.40	-
Width of 2^{nd} unstable area	[rad/s]	-	38.35	66.23	65.09	37.61	-
Lower boundary of 3^{rd} unstable area	[rad/s]	745.42	754.75	779.33	840.86	781.84	758.24
Upper boundary of 3^{rd} unstable area	[rad/s]	1015.83	1005.00	975.00	890.11	957.98	991.54
Width of 3^{rd} unstable area	[rad/s]	270.41	250.25	195.67	49.25	176.14	233.30
Shifting of 3^{rd} lower boundary due to ω_3	[%]	10.73	10.40	9.37	13.16	12.39	11.65
Shifting of 3^{rd} upper boundary due to ω_4	[%]	10.73	12.48	15.77	11.93	10.83	10.31

Table C.3: Identified paramaters of the rotor cases with the coefficient of element anisotropy at $\mu_W = 0.5$

Parameter	Unit	Model-5	Model-6	Model-7	Model-8	Model-9	Model-10
Natural frequency, $\omega_{1\ at\ \Omega=0}$	[rad/s]	126.30	127.32	130.25	139.61	132.84	128.96
Natural frequency, $\omega_{2\ at\ \Omega=0}$	[rad/s]	218.76	212.84	199.42	174.24	191.41	205.84
Natural frequency, $\omega_{3\ at\ \Omega=0}$	[rad/s]	469.80	484.64	522.73	542.93	493.74	475.64
Natural frequency, $\omega_{4\ at\ \Omega=0}$	[rad/s]	813.73	736.63	658.76	618.87	709.44	768.31
Lower boundary of 1^{st} unstable area	[rad/s]	131.00	132.25	135.89	147.89	138.65	134.01
Upper boundary of 1^{st} unstable area	[rad/s]	226.89	220.27	205.23	177.08	197.98	213.84
Width of 1^{st} unstable area	[rad/s]	95.89	88.02	69.34	29.19	59.33	79.83
Shifting of 1^{st} lower boundary due to ω_1	[%]	3.72	3.87	4.33	5.93	4.37	3.92
Shifting of 1^{st} upper boundary due to ω_2	[%]	3.72	3.49	2.91	1.63	3.43	3.89
Lower boundary of 2^{nd} unstable area	[rad/s]	-	379.40	364.28	362.71	377.45	-
Upper boundary of 2^{nd} unstable area	[rad/s]	-	432.82	455.79	449.35	427.57	-
Width of 2^{nd} unstable area	[rad/s]	-	53.42	91.51	86.64	50.12	-
Lower boundary of 3^{rd} unstable area	[rad/s]	520.23	533.65	566.60	639.30	562.11	533.93
Upper boundary of 3^{rd} unstable area	[rad/s]	901.06	884.62	838.60	706.51	806.84	859.26
Width of 3^{rd} unstable area	[rad/s]	380.83	350.97	272.00	67.21	244.73	325.33
Shifting of 3^{rd} lower boundary due to ω_3	[%]	10.73	10.11	8.39	17.75	13.85	12.26
Shifting of 3^{rd} upper boundary due to ω_4	[%]	10.73	20.09	27.30	14.16	13.73	11.84

Table C.4: Identified paramaters of the twisted anisotropic rotor case with the coefficient of element anisotropy at $\mu_W = 0.2$

Parameter	Unit	3-Elements	6-Elements	24-Elements	Change of 6 el. due to 3 el. [%]	Change of 24 el. due to 6 el. [%]
Natural frequency, $\omega_{1\ at\ \Omega=0}$	[rad/s]	215.72	214.15	213.66	-0.73	-0.23
Natural frequency, $\omega_{2\ at\ \Omega=0}$	[rad/s]	254.18	256.89	257.79	1.07	0.35
Natural frequency, $\omega_{3\ at\ \Omega=0}$	[rad/s]	820.30	805.17	800.85	-1.84	-0.54
Natural frequency, $\omega_{4\ at\ \Omega=0}$	[rad/s]	921.46	946.42	953.04	2.71	0.70
Lower boundary of 1^{st} unstable area	[rad/s]	224.34	222.35	221.75	-0.89	-0.27
Upper boundary of 1^{st} unstable area	[rad/s]	262.79	266.07	267.13	1.25	0.40
Width of 1^{st} unstable area	[rad/s]	38.45	43.72	45.38	13.71	3.80
Shifting of 1^{st} lower boundary due to ω_1	[%]	4.00	3.83	3.79		
Shifting of 1^{st} upper boundary due to ω_2	[%]	3.39	3.57	3.62		
Lower boundary of 2^{nd} unstable area	[rad/s]	570.67	573.46	575.69	0.49	0.39
Upper boundary of 2^{nd} unstable area	[rad/s]	619.06	615.94	613.29	-0.50	-0.43
Width of 2^{nd} unstable area	[rad/s]	48.39	42.48	37.60	-12.21	-11.49
Lower boundary of 3^{rd} unstable area	[rad/s]	900.15	888.35	885.12	-1.31	-0.36
Upper boundary of 3^{rd} unstable area	[rad/s]	1042.95	1058.10	1061.41	1.45	0.31
Width of 3^{rd} unstable area	[rad/s]	142.80	169.75	176.29	18.87	3.85
Shifting of 3^{rd} lower boundary due to ω_3	[%]	9.73	10.33	10.52		
Shifting of 3^{rd} upper boundary due to ω_4	[%]	13.18	11.80	11.37		

Table C.5: Identified paramaters of the twisted anisotropic rotor case with the coefficient of element anisotropy at $\mu_W = 0.3$

Parameter	Unit	3-Elements	6-Elements	24-Elements	Change of 6 el. due to 3 el. [%]	Change of 24 el. due to 6 el. [%]
Natural frequency, $\omega_{1\ at\ \Omega=0}$	[rad/s]	184.88	183.01	182.43	-1.01	-0.32
Natural frequency, $\omega_{2\ at\ \Omega=0}$	[rad/s]	236.99	241.28	242.73	1.81	0.60
Natural frequency, $\omega_{3\ at\ \Omega=0}$	[rad/s]	712.54	693.56	687.85	-2.66	-0.82
Natural frequency, $\omega_{4\ at\ \Omega=0}$	[rad/s]	842.21	881.79	892.85	4.70	1.25
Lower boundary of 1^{st} unstable area	[rad/s]	192.49	190.11	189.40	-1.24	-0.37
Upper boundary of 1^{st} unstable area	[rad/s]	244.62	249.70	251.38	2.08	0.67
Width of 1^{st} unstable area	[rad/s]	52.13	59.59	61.98	14.31	4.01
Shifting of 1^{st} lower boundary due to ω_1	[%]	4.12	3.88	3.82		
Shifting of 1^{st} upper boundary due to ω_2	[%]	3.22	3.49	3.56		
Lower boundary of 2^{nd} unstable area	[rad/s]	498.52	502.14	505.02	0.73	0.57
Upper boundary of 2^{nd} unstable area	[rad/s]	564.75	560.53	556.76	-0.75	-0.67
Width of 2^{nd} unstable area	[rad/s]	66.23	58.39	51.74	-11.84	-11.39
Lower boundary of 3^{rd} unstable area	[rad/s]	779.33	764.28	759.85	-1.93	-0.58
Upper boundary of 3^{rd} unstable area	[rad/s]	975.00	997.04	1001.59	2.26	0.46
Width of 3^{rd} unstable area	[rad/s]	195.67	232.76	241.74	18.96	3.86
Shifting of 3^{rd} lower boundary due to ω_3	[%]	9.37	10.20	10.47		
Shifting of 3^{rd} upper boundary due to ω_4	[%]	15.77	13.07	12.18		

Lebenslauf

Name : Jhon Malta
geboren am : 28. Januar 1976 in Bukittinggi, Indonesien

07/1982 - 06/1988 : Grundschule (SDN 2), Payakumbuh, Indonesien
07/1988 - 06/1991 : Mittelschule (SMPN 1), Payakumbuh, Indonesien
07/1991 - 06/1994 : Oberschule (SMAN 3), Payakumbuh, Indonesien
08/1994 - 02/1999 : Bachelor Studium, Abteilung Maschinenbau, Fakultät für Ingenieurswesen, Universität Andalas, Indonesien
06/1998 - 07/1998 : Praktikum im PT. Caltex Pacific Indonesien
04/1999 - 07/1999 : Wissenschaftlicher Assistent im Kollaborationsprojekt (Abteilung Maschinenbau, Fakultät für Ingenieurswesen, Universität Andalas und PT. Padang Zement), Indonesien
08/1999 - 09/2001 : Master Studium, Abteilung Maschinenbau, Institut Technologie Bandung, Indonesien
12/2001 - 07/2004 : Dozent an der Abteilung Maschinenbau, Fakultät für Ingenieurswesen, Universität Andalas, Indonesien
10/2005 - 09/2006 : Wissenschaftlicher Mitarbeiter (Doktorand) am Fachgebiet Mechanik II, Fachbereich Mechanik, der Technischen Universität Darmstadt
10/2006 - 05/2009 : Wissenschaftlicher Mitarbeiter (Doktorand) am Fachgebiet Strukturdynamik, Fachbereich Maschinenbau, der Technischen Universität Darmstadt